Politecnico di Torino

Corso di Laurea Magistrale in Ingegneria Aerospaziale

TESI DI LAUREA MAGISTRALE

Verification and Validation of a CFD simulation model for resonance igniter heat-up phase

Relatore:
Prof.
Dario Giuseppe
Pastrone

Candidato:
Andrea Romano
Matr.: 246678

ANNO ACCADEMICO 2018-2019

Abstract

The main aim of this master thesis is to verify and validate a CFD code that simulate a resonance igniter for rocket engines applications during the transient heat-up phase and using air as working fluid, in order to establish if it is capable to reproduce the experimental results and the main flow features. This analysis is motivated by the urgent need of developing a reliable and safe igniter for rockets upper stages driven by green propellants, not hypergolic because they are hydrazine free, since this material has been classified as toxic. Thanks to the high reliablity this ignition technology is particularly suitable for satellite propulsion systems with long mission durations and a high number of ignitions.
The work has 3 main parts. First of all, an overview of the main characteristics and fundamentals of resonance ignition is pointed out.
In the second part a theoretical method to analyze resonance heating is shown, in order to go deeper in the reasons of heating and in its theoretical basis. The limits of this kind of analisys will be pointed out,showing that ,for realistic applications, CFD is a more reliable method. Theoretical approaches can give only some preliminary information about the heating preformances of the resonator.
In the last part of the thesis a numerical analysis is done by using the commercial CFD software ANSYS FLUENT, in order to find a suitable setup that can simulate this phenomenon in a realistic way. The CFD code is first verified, checking if it is capable to reproduce the most important flow features. The verification main parts are: mesh and timestep size sensitivity study,that were carried out with the GCI method, iterative convergence and consistency checks. The results are finally validated over a prior experimental campaign conducted by "Lehrstuhl für Turbomaschinen und Flugantriebe" (LTF) in Technical University of Munich (TUM). The validation is carried out by comparing the frequency spectrum of cavity base pressure with the microphone resoponse of the experiments, since no internal pressure or temperature measurements were available due to the high temperatures inside the cavity.
The results of the simulations suggest that the code is able to reproduce the main flow characteristics ,such as the stable periodic alternation of inflow and outflow phases and the underexpanded jet cells structure,as shown by schlieren images comparison. Furthermore the peak frequency of the simulation pressure history FFT analysis agree well with the experimental results, especially excluding from the evaluation window the first transitory cycle the error lowers from 13 % to 6 %. The code is not realistic for temperature predictions, since no wall heat trnasfer was considered.The code is not realistic for temperature predictions, since no wall heat tansfer was considered. Looking into the effect of temperature dependent Cp and viscosity was found out that a more realistic temperature response can be obtained, even if the FFT analysis doesn't show great changes.
However the last conclusion are only preliminary, since are limited by the coarse resolution of the frequency domain, related to a too small evaluation window, limited by computational resources. For future validations is suggested an higher running time to make a more reliable comparison.

Contents

1 Introduction **1**

2 Resonance ignition foundamentals **3**
2.1 Resonance ignition working principles 3
2.1.1 Main oscillation modes 4
2.2 Main parameters affecting gasdynamic ignition 6
2.3 Resonance igniter designs 12
2.3.1 Most common resonance ignition workflow 12
2.3.2 Other successful designs 13

3 Theoretical analysis approach **17**
3.1 General features of the flow 17
3.2 Heating mechanism 20
3.2.1 Shock wave heat dissipation 20
3.2.2 Friction heat dissipation 21
3.3 Heating limiting factors 22
3.3.1 Wave steepening limit 22
3.3.2 Mass exchange between cold and hot gas 23
3.3.3 Forced convection heat transfer 24
3.4 Power balance 25
3.5 1D theoretical model 27

4 Numerical investigation **31**
4.1 Computational Fluid Dynamics 31
4.1.1 Governing equations 31
4.1.2 Turbolence model 33
4.2 CFD software: Ansys Fluent 33
4.2.1 Density based solver 34
4.2.2 Pressure based solver 35

5 Simulation with Fluent **37**
5.1 Prior experimental investigation 37
5.2 CFD simulation 40
5.2.1 Geometry 40
5.2.2 Boundary conditions 40

5.2.3 Timescales 41
5.3 Mesh 43
5.3.1 Modeling the boundary layer 43
5.4 Setup summary 45

6 Verification of the CFD code **47**
6.0.1 Mesh sensitivity study 47
6.0.2 Temporal discretization sensitivity 55
6.0.3 Examination of consistency 57
6.0.4 Examination of iterative convergence 60

7 Validation of the results **63**
7.1 Pressure frequency spectrum comparison 63
7.2 Influence of variable Cp 67
7.3 Influence of variable μ 70
7.4 Schlieren image comparison 74

8 Conclusions **77**
8.1 Possible future developements 78

List of Figures

2.1 Classical nozzle-resonator configuration with resonator cavity and underexpanded nozzle flow [1] . . . 3
2.2 Free jet structure [2] . . . 4
2.3 Effect of nozzle cavity gap on cavity base temperature [2] . . . 7
2.4 Normalized cell boundary position and nozzle-cavity gap for peak cavity-base temperature as function of ratio of nozzle pressure to ambient pressure. [2] . . . 8
2.5 Cavity base wave amplitude as a function of nozzle pressure for various NPR [2] . . . 8
2.6 Effect of ratio of nozzle pressure to ambient pressure on peak cavity-base temperature for various nozzle pressures. [2] . . . 9
2.7 Effect of cavity depth on cavity base temperature [2] . . . 10
2.8 Thruster scheme [3] . . . 12
2.9 Rocketdyne thruster design [4] . . . 13
2.10 Z1 resonance igniter scheme [1] . . . 15
2.11 Kessaev resonance igniter scheme [4] . . . 15

3.1 Wave diagram example [5] . . . 19
3.2 Static instability of shock in a periodic jet [6] . . . 20
3.3 Entropy temperature diagram for incident and reflected shocks [7] . . . 21
3.4 Longitudinal temperature distribution and waves reflected and transmitted at temperature discontinuity [8] . . . 22
3.5 Boundary layer profile in a system of coordinates fixed with the contact surface [7] . . . 24
3.6 Temperature at thermal equilibrum in the tube [7] . . . 26
3.7 Simplified phisical model: Inflow (a) and outflow (b) [9] . . . 27
3.8 Heating curves with respect of number of cycles (n) and time [9] . . . 28
3.9 Theoretical heating gas properties [9] . . . 28

4.1 Workbench layout . . . 34
4.2 Pressure based solver algorithms [10] . . . 35

5.1 Experimental setup for sound and resonator bottom temperature measurement [11] . . . 37
5.2 Equilibrium temperature for various nozzle distances at a NPR of 4 [11] . . . 38
5.3 Resonator geometries used during the test campaign. [11] . . . 38

5.4 Resonator geometries dimensions [11] . . . 39
5.5 Non-calibrated microphone response spectrum for conical resonator at NPR 4 and s/d of 0.8 and 2.4 [11] . . . 39
5.6 Case 1 geometry . . . 40
5.7 Case 1: boundary conditions . . . 41
5.8 Foundamental frequencies for cylindrical and conical cavity compared to experimental frequency . . . 42
5.9 Effect od increasing or decreasing y+ for the stream over a flat plate [10] . . . 43
5.10 Y+ of the cavity walls at t=0.7 ms . . . 44
5.11 Underexpanded jet structure . . . 45
5.12 Mesh details of the cavity entrance and the nozzle exit . . . 45

6.1 Pressure axial distribution at $t = 1.5\tau_{conv}$ for the 3 different meshes . . . 50
6.2 Pressure history . . . 50
6.3 Pressure axial distribution at for the 3 different meshes for the same shock position . . . 51
6.4 Cavity base temperature with respect to mesh refinement at $t = 1.5\tau_{conv}$ . . . 52
6.5 Axial distribution of pressure for the 2e-8 s timestep and with the finest mesh 53
6.6 Axial distribution of pressure for the 2e-8 s timestep and with the finest mesh 54
6.7 Autoignition temperature of air-methane mixture with respect to methane concentration [12] . . . 55
6.8 Axial distribution of pressure for the finest timestep and with the finest mesh . 56
6.9 Axial distribution of density for the finest timestep and with the finest mesh . 56
6.10 Axial distribution of pressure for the finest timestep and with the finest mesh . 57
6.11 Outlet and inlet mass flow rates . . . 57
6.12 Outlet mass flow rate for different outlet distances . . . 58
6.13 Outlet mass flow rate and cavity entrance mass flow rate for the standard case 59
6.14 Residuals of the equation with respect to the iterations for the finest mesh . . 60
6.15 Cavity entrance mass flow with respect to the iterations for the finest mesh . . 61
6.16 Cavity entrance mass flow with respect to the iterations for the finest mesh . . 61

7.1 Frequency spectrum of cavity base pressure of the simulation (5 ms runtime) 64
7.2 Non-calibrated microphone response spectrum for conical resonator at NPR 4 and s/d of 0.8 and 2.4 [11] . . . 64
7.3 Pressure history of the cavity closed end . . . 65
7.4 Last 4 cycles FFT . . . 66
7.5 Last 5 cycles FFT . . . 66
7.6 Last 7 cycles FFT . . . 66
7.7 Last 9 cycles FFT . . . 66
7.8 Cavity closed end temperature: variable Cp effect . . . 67
7.9 Cavity closed end pressure: variable Cp effect . . . 68
7.10 Frequency spectrum of cavity base pressure of the simulation for temperature dependent Cp . . . 69
7.11 Sutherland law . . . 70

7.12 Frequency spectrum of cavity base pressure of the simulation for temperature dependent viscosity 71
7.13 viscosity effect on mass exchanged between extranous and indigenous flow . 72
7.14 Cavity closed end temperature: variable viscosity effect 73
7.15 Cavity mass flow rate: variable viscosity effect 73
7.16 Numerical schlieren-like image during outflow: t=0.33 ms 75
7.17 Numerical schlieren-like image during inflow: t=0.11 ms 75
7.18 Comparison of numerical and experimental schlieren image during outflow . 76

List of Tables

6.1 Mesh influence at $1.5\tau_{conv}$ 52

7.1 65

Chapter 1

Introduction

European Union REACH framework recently classificated Hydrazine and it's derivatives as "material of very high concern", because it's highly toxic, can cause cancer and may damage the environment [13].Therefore looking forward for the near future a less toxic propellant is required for In-Orbit propulsion systems.
The biggest advantage of hydrazine based rocket engines is their ease of ignition, this propellant do not need a a dedicated ignition system, since in the bipropellant configuration auto-ignite due to the hypergolic behaviour of the propellants, and in the monopropellant engines hydrazine is decomposed by catalysis [4]. The green propellants based engines contrariwise need a dedicated ignition system, so finding a reliable and safe ignition system is a major issue, expecially for upper stages, since for boosters and lower stages conventional igniters from LOX/LH2 can be adapted to ignite different propellant combinations [4].
Electric spark igniters worked well in general, but there are still several problems, such as wiring isolaton, system complexity and high frequency electrical interference [2]. New generation stages however require more reliability and durability and have to be reusable indefinitely, expecially for very long satellite propulsion missions (more than 10 years) and millions of engine cycles. For these applications resonace igniters could be a good choice, since they require no elctrical power, moving parts, degrading catalysts, electrodes or optical acess, providing quasi hypergolic behaviour using more stable propellants [4].Furthermore this kind of ignition gives some more advantages,for example high pressure ignition is achieved within milliseconds, even in the cold vacuum environment of space; combustion instabilities are eliminated, and acoustic vibration is reduced locating and sizing properly the resonance tubes within the combustion chamber.
Thanks to the previously listed characteristics resonance ignition had been investigated worldwide with promising results. Even the Institute for Flight Propulsion (LTF) of the Technical University of Munich (TUM) investigates Resonance Ignition methods for green propellants engines.
From this introduction is clear the importance of resonance ignition for rocket propulsion applications.In this thesis the analysis of this phenomenon will be done by using especially CFD methods. The main aim of the thesis is to verify and validate over experimental results a FLUENT CFD code, finding a setup that can simulate in a reliable way the main features of the flow in the tube.
In the first chapter an overview on the phenomenon and on previous researches is carried out,

giving some informations about typical design of the igniter.
The second chapter gives some more detailed informations about the flow features and the physics involved in the heating mechanisms. It is pointed out that all theoretical models can only give order of magnitude prediction, and it is necessary to use more advanced methods,such as CFD.
The third chapter gives some general information about the solvers used , and the fourth chapter gives an overview about the problem analyzed. It is shown the previous experiment that will be simulated, than an overviw on the geometry, boundary conditions, mesh and setup is given.
In the fifth chapter the verification process of the code is carried out. The mesh and timestep convergence study is done, some checks on the consistency and iterative convergence are carried out.
In the last chapter the validation against the experimental results is done. The results are validated over a prior experimental campaign conducted by "Lehrstuhl für Turbomaschinen und Flugantriebe" (LTF) in Technical University of Munich (TUM). The validation is carried out by comparing the frequency spectrum of cavity base pressure with the microphone resoponse of the experiments, since no internal pressure or temperature measurements were available. Moreover the effect of the fluid properties over the results is analyzed, especially looking at the effect of a temperature dependent C_p (constant pressure gas specific heat) and viscosity μ. Moreover by comparing the schlieren images of the undrexpanded jet with the numerical schlieren was qualitatively verified that the main jet structure characteristics were reproduced.

Chapter 2

Resonance ignition foundamentals

2.1 Resonance ignition working principles

Resonance ignition is based on a device known as "Hartmann-Whistle", used to produce powerful sound. This mechanism was first discovered by Hartmann in 1919 while making pressure measurements on an underexpanded supersonic free jet by using a pitot tube [14]. He noticed that strong pressure oscillations were triggered inside the pitot tube at certain nozzle-tube distances, that produced a loud sound.

Only later, in 1954, Sprenger [15] discovered that this violent oscillation of the gas can produce in particular conditions (for example low conductivity cavity) a notable heating effects, for example he obtained temperatures in excess of 1265 K by using room-temperature air. This device is called "Hartmann-Sprenger tube" or "resonance tube", and it works by trapping a small quantitiy of high pressure gas inside the tube and heating it by a succession of shock waves passing through the trapped gas. As Sprenger himself suggested, the heating is caused by the shockwaves travelling inside the tube, which cause dissipative heating, so the strenght and the frequency of the schock will determine the heating of the gas trapped in the cavity. Other researchers found that another factor causing heating is the wall friction, but a complete description of the phenomena has not been found yet [4]. For example Reynolds attributes the dissipation to the turbulence of the flow inside the tube.[7] In reality, the two

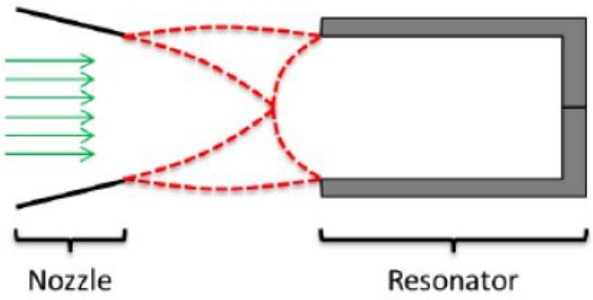

Figure 2.1: Classical nozzle-resonator configuration with resonator cavity and underexpanded nozzle flow [1]

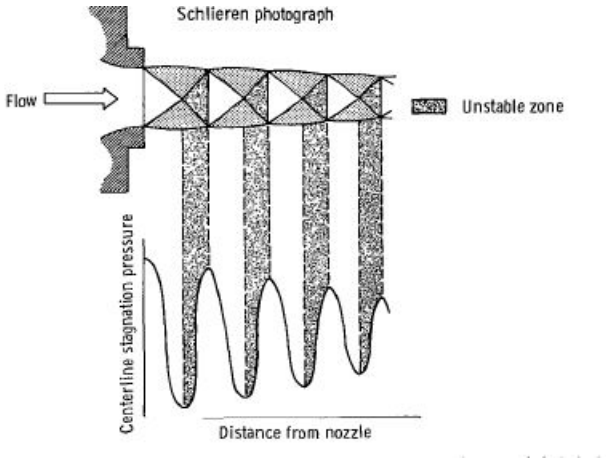

Figure 2.2: Free jet structure [2]

dissipative mechanisms, irreversibility of the shock waves and friction in the inner wall of the tube, both play a role in the temperature rise inside the tube.
The heating mechanism cited before is limited by some factors.Several authors suggest that the heat dissipated is transferred to the walls of the tube by forced convection, and that this heat is then carried off in the atmosphere by radiation and free convection around the tube.[7]
Another factor limiting the resonance heating is the mechanism proposed by Wilson and Resler [7]. Passage from the expansion phase to the compression phase does not occur instantaneously, and a train of compression waves is formed at the mouth of the tube.This wave train need to travel until a certain space before it coalesce in a shock. Wilson and Resler have found out that this coalescence distance increases with the temperature of the gas. Thus, insofar as the energy dissipation is due principally to the shock waves, the limiting temperature will be achieved when the wave train no longer has time to form a shock inside the tube.[7]
The mechaninsm of resonance heating is strictly related to the underexpanded jet flow structure(shown in figure x). If the supersonic jet hit a blunt body (in this case the cavitiy entrance) a detached shock will appear around it. The shock will be in a fixed position from the blunt body. If the nozzle and the flow field are adjusted relative to the cavity there will be zones in which the shock will oscillate, in this case there is a resonance condition. This zones, shown in figure 2.2 are unstable regions where pressure tends to oscillate. If the bowshock is inside this region compression or shockwaves will be detached from the shock and travel up and down inside the cavity [2].
So because jet flow between the nozzle exit and the tube inlet plays a key role in the performance of a resonance tube, the nozzle-cavity distance is idenfied as one of the most important parameters affecting resonance heating.

2.1.1 Main oscillation modes

Concerning the oscillations one of the most remarkable work has been done by Sarohia and Back [16], which experimentally studied the effects of tube location in relation to free-jet shock location, and identified the main oscillation modes in resonance tubes. They identified three different modes of operation, depending upon the tube, gap size, and jet Mach number,

all of them have different thermal effects.

- **Jet Instability Mode**: this mode only occurs for subsonic jets. In this mode a weak compression wave inside the tube was generated by the toroidal vortices that were created by the jet and grew in size as they moved downstream. In this mode the frequency of pressure fluctuations in the tube was equal to the vortex shedding frequency [17]. Since neither large heating effects nor relevant pressure amplitudes are generated it is not of further interest. [18]

- **Jet Regurgitant Mode (JRM)**: This mode was observed when the gap between the nozzle and the tube was greater than the free-jet shock location relative to the nozzle [17]. It is characterized by a periodic ingestion and almost a complete expulsion of gases in the cavity for each cycle. This cycle is characterized by the fundamental frequency of the resonator, in and outflow phases have different durations. Strong heating effects can only be observed in long tubes, due to the fact that in this mode there are a series of compression waves entering in the cavity, that can coalesce forming strong shocks only if the tube is long enough.In this case a portion of the fluid near the closed end of the tube remains in the resonator and is repeatedly compressed and expanded, causing gradual heating through irreversible effects. If the tube is short there are only weak compression waves which compress and expand the gas almost isentropically. [18]

- **Jet Screech Mode (JSM)**: this mode was observed when the gap was equal to or less than the free-jet shock location relative to the nozzle [17]. is characterized by relatively weak pressure oscillations at frequencies much higher than the fundamental frequency of the resonator. In this mode the normal shock in front of the cavity inlet is oscillating at high frequency. Under certain conditions and for short resonators strong heating at local node points can be observed, suggesting that standing waves are present within the cavity.[18]
  In JSM Sarohia and Back observed considerable gas heating only for short resonators, longer resonators remained at almost ambient temperatures. That was confirmed even by investigation at LTF, but a satisfying explanation of this behaviour is still uknown.[18]

2.2 Main parameters affecting gasdynamic ignition

In this section the most important parameters influencing resonance heating are pointed out. 7 main effects are here considered:

- **Effect of nozzle-cavity gap**
- **Effect of nozzle pressure ratio**
- **Effect of wall friction**
- **Effect of cavity length**
- **Effect of cavity geometry**
- **Effect of the nature of the gas**
- **Effect of tube material**

In the next part of this section all the aforementioned effects are described in a more detailed way.

- **Effect of nozzle-cavity gap** As pointed out in the previous section, resonance heating happens when the bowshock in front of the cavity mouth is located in one of the unstable areas of the jet flow field.
  Philips and Pavli [2] investigated this effect sudying the position of the instable zone of the free underexpanded jet by changing the nozzle pressure ratio and took shlieren images of it,since the shock structure of the jet doesn't change in a noticeable way if the cavity is present. "From these photographs, the distance from the nozzle to the first cell boundary was measured. This distance (s), divided by the nozzle diameter (d), was plotted as a function of the nozzle pressure/ambient pressure ratio."[2]
  In the same paper they investigated the effects of the nozzle-cavity gap on the cavity base temperature. The result can be seen in figure 2.3, as we can see from the curve the maximum cavity base temperature occurs at greater gaps then the free jet cell boundaries, due to the fact that the bowshock forms at a certain distance from the cavity mouth. To have resonance heating the bowshock must be coupled with the unstable zone of the jet. This effect is also shown looking at figure 2.4, where are plotted the distance s/d that gives the peak temperature and the distance s/d of the free jet cell boundary as a function of NPR. The distance between the two curves represents the bowshock distance from the cavity mouth.Reporting the Philips and Pavli conclusions:" The most significant result found was that the nozzle gap effect was controlled solely by the nozzle diameter and the ratio of nozzle pressure to ambient pressure. If the pressure ratio and the nozzle diameter are fixed, so is the nozzle gap corresponding to a peak in the cavity-base temperature" [2].

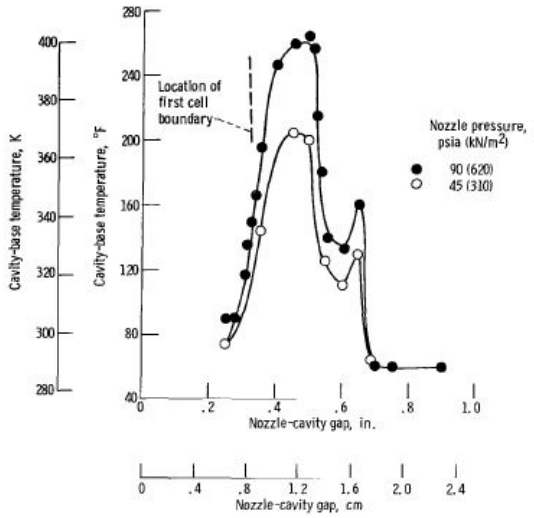

Figure 2.3: Effect of nozzle cavity gap on cavity base temperature [2]

- **Effect of nozzle pressure ratio (NPR)** Nozzle pressure ratio is defined by the following equation, where p_e s the downstream static pressure and p_n is the feed pressure upstream of the nozzle or the total pressure in the nozzle exit plane, assuming isentropic expansion [1].

$$NPR = \frac{p_n}{p_e}$$

The effect of this parameter on the cavity base temperature was examined experimentally by Philips and Pavli [2]. The first experiment was to maintain a fixed NPR and vary the pressure, obtaining a linear realtionship between cavity base pressure amplitude and temperature. The results,displayed in figure 2.5 show also iso-NPR curves, and the best performances seems to be at NPR=4.5. Next was examined the pressure temperature relationship at fixed pressure ratios, that resulted to be definitely nonlinear.

A crossplot that summarize the results is shown in figure 2.6. It shows cavity-base temperature as a function of nozzle pressure ratio at fixed values of nozzle pressure. Looking at the curves an optimum NPR value can be identified between 4.8 and 4.5. The optimum NPR value seems to be similar (around 4.5) even changing the nozzle diameter. Both peak pressure amplitude and cavity base temperature are realized at NPR=4.5, but the reasons of this are still unknown.

- **Effect of wall fricion** The effect of roughness of the inner wall of the tube plays an important role on heating, expecially for small-tubes. That is explained by the fact that the mechanical energy dissipated by friction on the tube walls increases with the tube inner wall roughness. The E.Brocher C.Maresca ivestigations on resonance heating

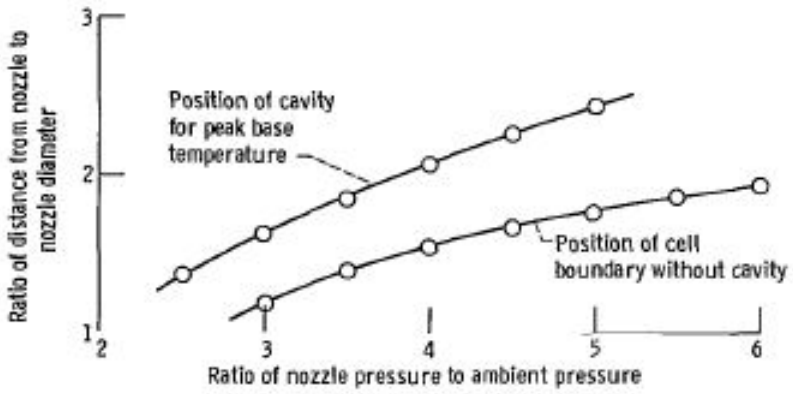

Figure 2.4: Normalized cell boundary position and nozzle-cavity gap for peak cavity-base temperature as function of ratio of nozzle pressure to ambient pressure. [2]

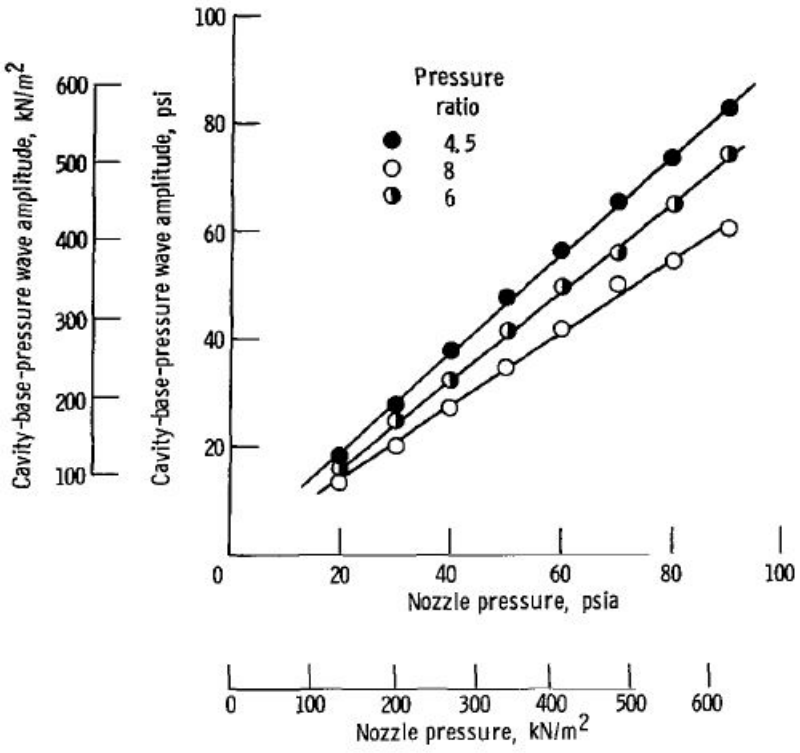

Figure 2.5: Cavity base wave amplitude as a function of nozzle pressure for various NPR [2]

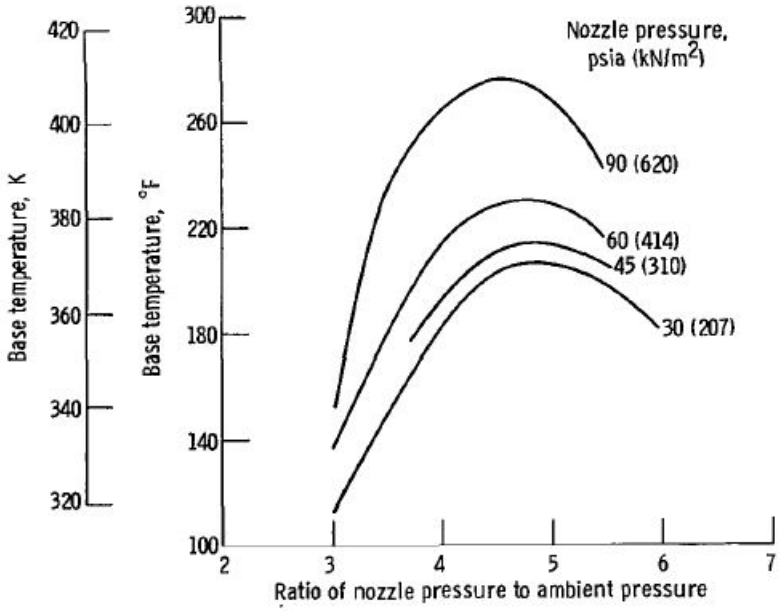

Figure 2.6: Effect of ratio of nozzle pressure to ambient pressure on peak cavity-base temperature for various nozzle pressures. [2]

pointed out that temperature rise is slightly higher for a rough-walled tube than for a smooth-walled one [7].

- **Effect of cavity length** Varying the resonance cavity depth the compression or shock waves will be traveling for a different length. More the cavity is long more likely the compression waves will coalesce and form strong shocks. At the same time if the tube length increase the oscillation period of the compression waves will increase too, since the speed at which the waves propagate doesn't change.
  Some experiment investigating about this were done by Pavli and Philips [2], for some different cavity depths they changed the nozzle pressure, at fixed pressure ratio (4,5) and nozzle-cavity gap (1.143 cm), evaluating the effect on the steady state cavity base temperature. The results are reported in figure 2.7, where each curve is a given cavity depth, and it is clear that a short tube gives better results. Their experiments also showed that the transition from a sinusoidal-type wave to a shock-type wave occurred at approximately 3.56 cm cavity depth. The second wave shape is characteristic of high-amplitude pressure oscillations in tubes
  In reference [2] it is also pointed out that increasing the length of the tube increases the surface area of the tube, leading to more convective and radiation thermal losses.

- **Effect of cavity geometry** Several studies investigated on the effects of the cavity shape on the thermal characteristics of the resonator, for example McAlevy and Pavlak [19] sudyied the effect of tapering the resonance tube, highlighting that for the same heat per cycle the frequency increased.
  Even Philips and Pavli [2] investigated on this, they evaluated and compared the cylin-

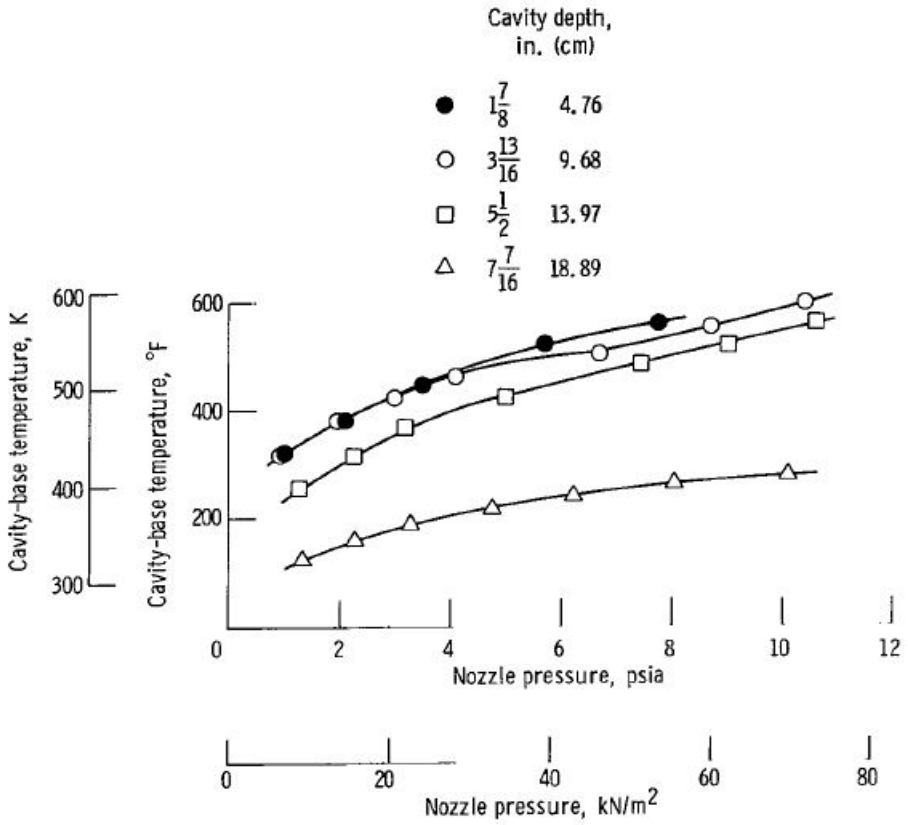

Figure 2.7: Effect of cavity depth on cavity base temperature [2]

drical and tapered cavity, resulting in the superiority of tapering, since the cavity base temperature more than doubled. Their result clearly indicated that was possible to reach temperatures far above 811 K at nozzle pressures above 1 psi by using a tapered shape. They even tested another configuration, adding a cylindrical extension to the tapered cavity. This solution resulted to be worst than the simply tapered one, because increasing the cavity lenght caused a frequency decrease.

- **Effect of the nature of the gas** For certain applications using air as resoanting gas is not sufficent, other gases must be considered. Philips and Pavli [2] tested the identical configuration (same nozzle-cavity gap and nozzle pressure ratio) with both gaseous hydrogen and nitrogen. Tey found that hydrogen produces much higher temperatures. Similar reults were produced using gaseous oxygen instead of nitrogen. Brocher and Maresca [7] made similar experiments using helium, argon, air, and oxygen. The mono- atomic gases produced a much higher temperature rise than did the diatomic gases.
  Philips and Pavli [2] explained this behaviour pointing out that, for the same conditions, the frequency of oscillation of the tube with hydrogen is at least three to four times greater than with nitrogen, that's due to the influence of molecular weight on sonic speed. So if the energy per cycle is the same, the energy per unit of time will be

bigger for the less heavy gas thanks to the greater oscillation frequency.

- **Effect of the tube material** Free convection and radiation around the outer wall of the tube are two mechanisms for removing the heat which can be reduced to a large extent [7]. In order to minimize heat loss from the gas to the resonance tube, materials of low conductivity are used.
  Pavli and Philips [2] in addiction to thermal conductivity pointed out the importance of structural strength and impermeability of the material.For example they tested foamed zirconia, material with a low conductivity and high strength, that was unsuccessful due to the absorption of the compression waves by the porous wall structure. Another test was made evaluating abestos composites. Bigger is the amount of bilder higher will be the strength, the density and the thermal conductivity.The material with the lowest percentage of binder was most successful in terms of giving high cavity-base temperatures, but it failed by cracking after a short time during the tests. Pavli and Philips, after these considerations, had chosen asbestos composite A as most suitable material.

2.3 Resonance igniter designs

2.3.1 Most common resonance ignition workflow

In this section is the described the most common resonance igniter workflow, as described by Bogdanov in reference [3].
As is possible to notice in figure 2.8 the igniter is composed by six main parts. The first is an injection nozzle where the working fluid (inert gas or oxidier) is injected. The working fluid is directed into the resonance cavity 4, that is usually tapered (for reasons explained in section 2.2) and can be sometimes composed by an ending cylindrical part with a wall at its end. The volume between the nozzle and the cavity it's the ignition chamber 3, separated from the main combustion chamber 6 by a wall having apertures 5 made integral to the resonator.
"Fuel components injection is carried out by the means of disposed co-axially fuel and oxidizer nozzles"[3]. Moreover,in order to achieve a better mixing uniformity,is used a gaseous oxidier instead of the inert gas. In this way the resonator is filled with pre-mixed fuel components and the mixture is ignited thanks to the heat produced by resonance heating it ignites other portion of mixture (which was already there but did not ignite on its own) and the flame propagates from the resoanator volume to the whole ignition chamber. After that the flames leave the ignition chamber through the apertures spreading into the main combustion chamber.
This design has a main disadvantage:up until ignition occurs the igniter is in contact with cold fuel components, that produces several thermal losses and extends the time necessary to achieve ignition.
In order to improve igniter performances rising thermal insulation of resonator this design had been modified. This new design consists in eliminating the physical contact of the resonator and combustion chamber structure by means of an additional protective cavity (in some cases vacuumed) around the resonator, in this way the cavity material is not in contact with cold fuel components. Another possible way is to use a low heat conductivity material for the resonance tube, that would lower thermal losses and reduce ignition time.[3]

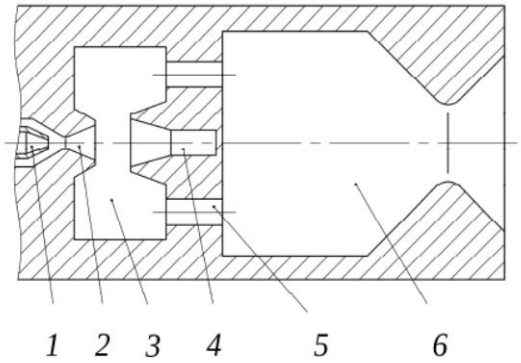

1 – fuel injector, 2 – igniter injector, 3 – ignition chamber, 4 – resonator, 5 – apertures, 6 – main combustion chamber

Figure 2.8: Thruster scheme [3]

2.3.2 Other successful designs

In this section some of the most famous resonance igniter successful projets are presented. Even if this experiments had been a success no one of these had been implemented in an actual engine, probabily because of the relatively strong sensitivity of the resonator oscillation mode to variations of the nozzle pressure ratio [1].

- **Rocketdyne 1973**
  This design is hydrogen/oxygen based and was intended to be used for the Auxiliary Propulsion System of the Space Shuttle. Even though this igniter design was demonstrated to be reliable in cryogenic conditions the program was later discontinued.[4]
  The igniter, depicted in picture 2.9 feature a simple converging nozzle generating an hydrogen underexpanded jet that impinges on a stepped cavity resonator. When enough hot hydrogen is produced by resonance heating oxygen is introduced by pressure-actuated valve, starting the combustion and generating a torch that can ignite the main combustion chamber ."This staggered introducion of the propellants became common for all later developements"[4]
  The restrictor orifice was designed to maintain sonic conditions during resonance heating, in order to decouple mixing chamber from downstream main combustion chamber, necessary to maintain a constant NPR. However this increases the required supply pressure, requiring high pressure rechargable tanks for pump fed engines, while the pressure actuated valve in the high temperature region of the resonator reduces the reliability of the otherwise completely passive device. [4]

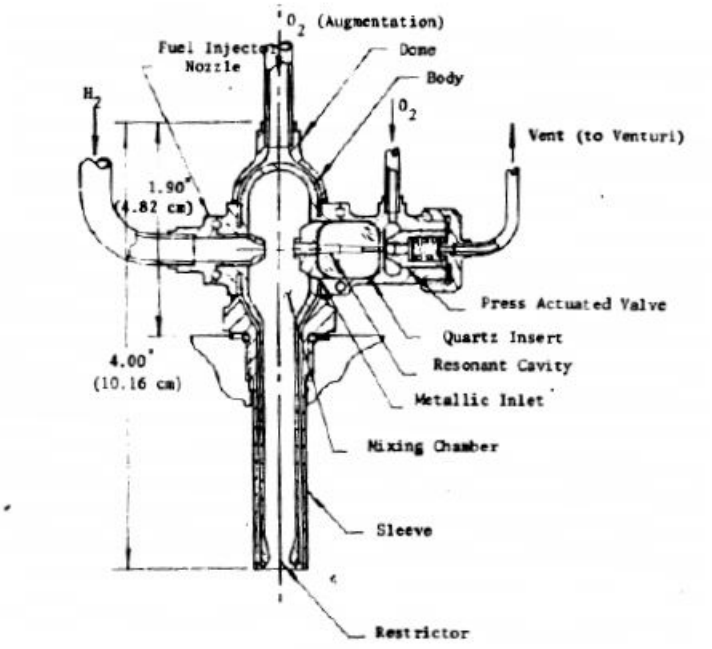

Figure 2.9: Rocketdyne thruster design [4]

- **Z1: TUM resonance igniter**
  This resonance igniter was designed by LTF in TUM and uses methane oxygen combinations, since LTF focuses his research on green propellants. This design is the product of researches focusing on reducing the sensitivity of oscillation mode to NPR variations, that demonstrated that special nozzle designs can sustain resonant oscillations over a wide range of NPR ranges.[1]
  The design is really similar to the one introduced in section 2.3.1 , it consists in a coaxial nozzle, the outer for oxygen and the inner for methane, whose cross sections are designed for ambient pressure during the resonance heating process. As shown in figure 2.10 a tapered resonator is aligned with the injection nozzle [1]. The tapered shape was chosen since preceding researches [2] found that this geometry gives better performances in terms of heating characteristics.
  The igniter operates in this way: oxygen is first introduced through the nozzle into the resonator at supersonic speed, leading to the resonant heating of oxygen, mainly of the oxygen trapped in the end of the resonator. When oxygen is hot enough methane flows into the resonator, mixes with the hot oxygen and then ignition occurs[1].
  In addition to proper nozzle designs,to reducing the sensitivity of resonance generating mechanism on NPR variations a chocked torch outlet was introduced, in this way a constant NPR is imposed directly. With a sonic chamber throat the ignition system becomes less influenced by the main combustion chamber during ignition start up.
  For this kind of igniter a oxidier/fuel ratio of 30 is chosen , since is sufficiently far from the flammability limit (O/F=36), but lean enough to raise hot gas temperatures that allow sufficiently long operating time of the system.[1] The ignition system is oxygen-rich, that reduces the main chamber ignition delay when the torch gases mix with the fuel rich propellant mixture from the main chamber injector.
  "The material, a cobalt-chrome-molybdenum alloy, offers very high temperature resistance combined with high corrosion durability, and thus enables its use for oxygen-rich applications." [1]

- **Kessaev et Al. 2000** Attempting to create an igniter for a restartable rocket engine the group around Kessaev developed and tested a resonance igniter for GOX/Kerosene.
  DIfferently from earlier designs the resonance gas is Oxygen, that ,due to its low heating rates, requires more a complex resonator design then the one required for a low molecoular mass gas like hydrogen .Kerosene is introduced perpendicular to the oxygen jet instead of insert it directly.That solves the problem of reqiring a fragile valve in the resonator hot region and allows much lower fuel feed pressures.[4]
  Tests demonstrated that reliable ignition was obtained for oxygen inlet pressures as low as 0.8 MPa and after a time of 0.1s. Since ignition was obtained for very low pressures it is possible to say that torch outlet was not designed as a sonic throat, so the igniter is influenced by disturbances originating from the main combustion chamber.This may cause problems when integrated into a real thruster, since, during the startup sequence, backpressure change may detune the system and cause a delayed or failed ignition.[4]

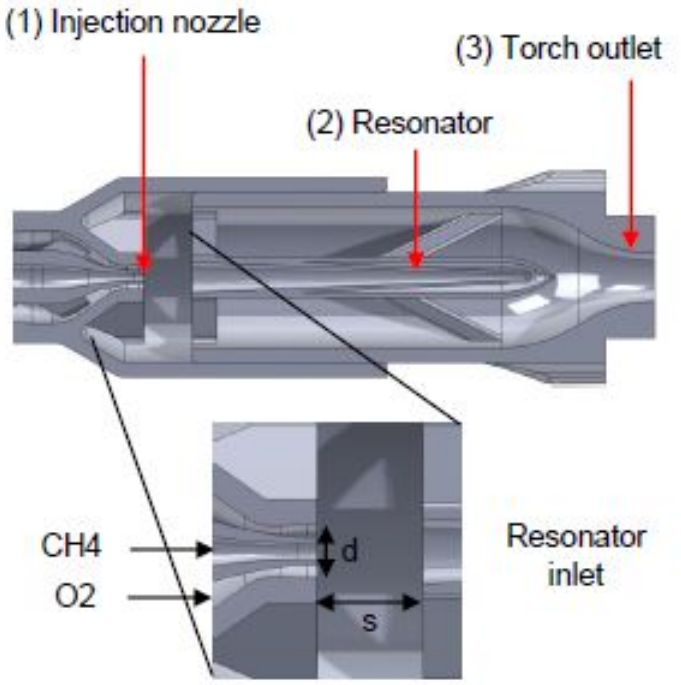

Figure 2.10: Z1 resonance igniter scheme [1]

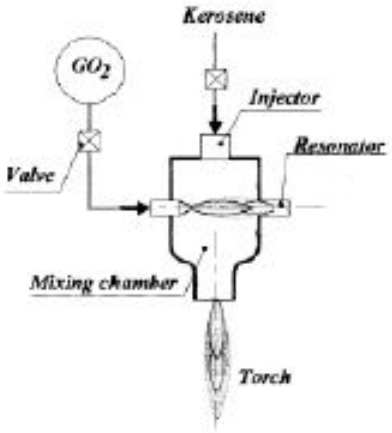

Figure 2.11: Kessaev resonance igniter scheme [4]

Chapter 3

Theoretical analysis approach

Due to the high complexity of the phenomena involved in resonance heating, only a few analytical and theoretical analyses have been published to date.
In this section will be analized the theory of resonance heating. In this way is possible to go deeper in the heating phenomena that occurs inside the resonance cavity, and knowing the shock wave behavior is necessary to underststand the basis of most of the 1D theoretical models that describe the heating preformances of the resoanance tubes.

3.1 General features of the flow

The typical flow of an Hartmann-Sprenger tube take origin by an underexpanded jet that interacts with a closed end cavity. To describe the phenomenon in more detail several experimental and theoretical analisys were carried out in these years, giving a more detailed description of the internal flow of the cavity and even of the external one, expecially thanks to the shlieren technique [6] [5].
One of the oldest and famous experimental and theoretical analyses is the one made by Thompson [6], that thanks to flow photographs and pressure records was able to deduce some of the main flow features of the resonator.
In the Thompson publication [6], but even in other publications such as the Prizirembel one [5], 4 distinct phases were detected in one resonance cycle:

- **Inflow phase**: At the beginning of the cycle most of the jet mass flow enters inside the cavity, a shock wave stands in front of the mouth and another shock travels inside the cavity and then is reflected at the cavity end.

- **Transition from inflow to outflow**: In this phase a shock wave start to exit from the cavity entrance and advance in the nozzle jet field. At the same time an expansion wave moves inside the the resonance tube. In this phase the outflow phase starts, but is still not stationary.

- **Outflow phase**: The flow coming from the tube penetrate in the jet region,the flow is almost sonic at the mouth, than it accelerate with a Prandtl-Mayer expansion and collides with the jet, in this phase the outflow is almost stationary. The outflow and the

jet collide in a plane interface, since there is a matching between the jet and the outflow impulse. As long as this matching is maintained, the collision structure will not change and the outflow will take place .

- **Transition from ouflow to inflow**: This is the last phase of the cycle. Compared to the first transition this one is much slower. The outflow decreases and the collision structure recedes, leading to a new inflow phase and a repeated cycle.

The flow is periodic,the cycles repeat themselves with a frequency can be calculated approximately with the acoustic theory [5]:

$$f_{0,cyl} = \frac{v}{4(L + 0.3D)} \tag{3.1}$$

As Thompson states, fluid can be modeled distinguishing between a fluid that enters during the inflow and then is expelled during the outflow and a fluid that is trapped inside the cavity. The first one is called 'extraneous fluid', the second 'indigenous fluid', and they are separeted by an entropy discontinuity. The extraneous flow is subject to an entropy rise only during one cycle, after that it is replaced by new fluid coming from the jet. The indigenous flow on the contrary is heated in every cycle by the traveling shock waves and its temperature and entropy rise.
To understand better what happens inside a resonance tube looking at the wave diagram can be quite helpful,since it represents adequately the basic flow phenomenon. G. Przirembel [5] constructed a wave diagram for a simple axisymmetric resonator by using his experimental data about the shock and espansion waves traveling velocities.

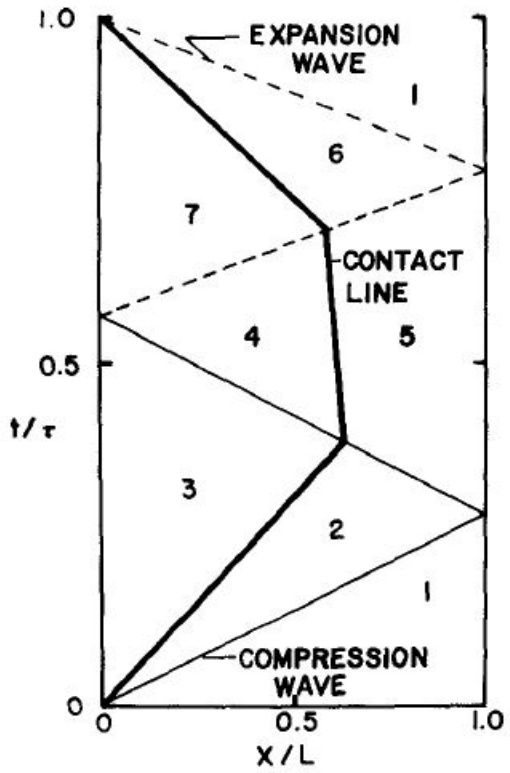

Figure 3.1: Wave diagram example [5]

The wave diagram represents on the y axis the time normalized with the period and on the x axis the x distance from the cavity entrance normalized with the cavity length. The compression wave position is represented with the dark line, it travels slower than the expansion wave(pointed line), since this one travels in a more hot fluid, already heated by the shock waves, and the speed of sound is proportional to the temperature of the fluid. The bold line represent the contact surface between the extraneous and the indigenous fluid, as it is possible to see the extraneous fluid never penetrate into the whole cavity.
Looking at the diagram is possible to point out some events: a point x of the cavity is first subject to an incident shock wave, than to the same shock wave reflected by the endwall and now traveling leftward.After the reflected wave reach the exit an expansion wave travels inside the cavity and it is reflected by the endwall.

Another important aspect of the resonance igniter flow is the underexpanded jet interaction with the cavity.This kind of jet is periodic and composed by cells. As Hartmann pointed out,the resonace tube distance from the nozzle must be long in a way that the cavity entrance is placed in the converging part of one of the periodic jet cells. [6].
Thompson gave a simple explaination of the bow shock instabilities in front of the cavity [6].

Looking at figure 3.2 it is possible to see two curves: the ondulatory one represents the

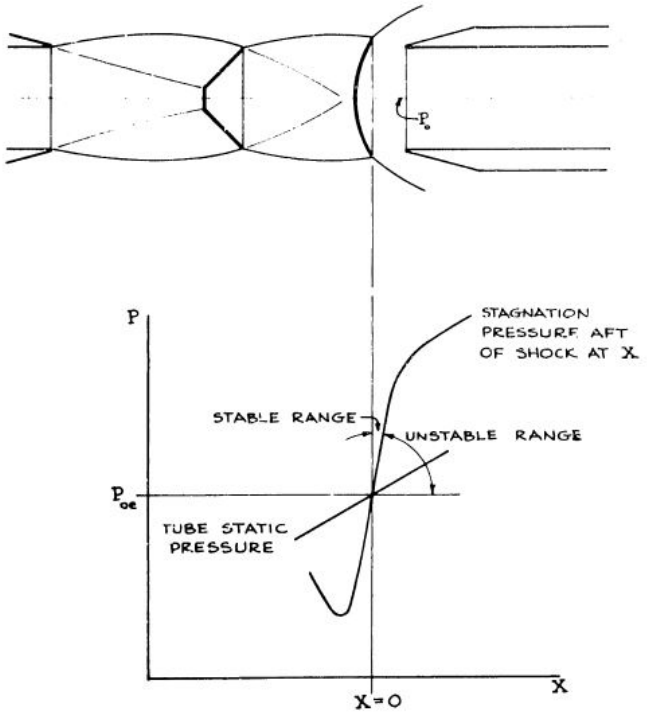

Figure 3.2: Static instability of shock in a periodic jet [6]

stagnation pressure after a shock having place at X. The straight one represents the pressure-length relation for a quasi static compression of the fluid. A displacement of the shock from the equilibrum position leads to a pressure difference that tends to increase the shock displacement, so to compress the fluid. That happens until the slope of the stagnation pressure curve is greater of the tube static pressure tube. The limit of static stability occurs when the slopes of the two curves are equal.

3.2 Heating mechanism

As mentioned in the previous chapter there are two main factors that lead to the fluid heating: heat dissipation because of shock waves and friction heat dissipation.

3.2.1 Shock wave heat dissipation

For the description of this mechanism the theoretical analysis of Brocher and Maresca will be reported.[7]
During one cycle the gas is run through an incident and a reflected shock waves, that rise the gas entropy. The authors of that paper calculated the mechanical energy dissipated in one

cycle Q_{irr}.

$$Q_{irr} = mC_p\Delta T_5 \tag{3.2}$$

Where $\Delta T_5 = T_5 - T_5'$. The pedix refers to the entropy temperature diagram. The incident shock wave bring the gas from 1 to 2 and the reflected from 2 to 5. If no heat is removed the isentropic expansion leads the fluid to 1'. To close the cycle is necessary to remove heat form 5 to 5'.

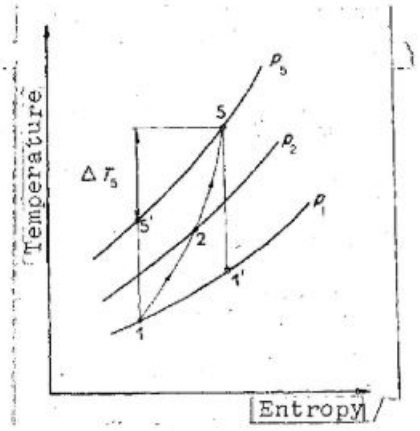

Figure 3.3: Entropy temperature diagram for incident and reflected shocks [7]

3.2.2 Friction heat dissipation

Heat dissipation caused by friction is one of the most important factors that lead to temperature increase in the tube. A theoretical analysis of this phenomenon was given by Brocher [7].
Considering the wave diagram (figure 3.1) at the abscissa x Cf_2 is the friction coefficient, u_2 is the mean velocity in the section considered. The energy dissipated by friction in the wall element dx during the time t2-t1 is:

$$dQ_{fr} = 0.5C_f\rho_2 u_2^3 \frac{S}{D}(t_2 - t_1)dx \tag{3.3}$$

Assuming that the dissipated heat during compression is the same during expansion t3-t4 we obtain:

$$dQ_{fr} = C_f\rho_2 u_2^3 \frac{S}{D}(t_2 - t_1)dx \tag{3.4}$$

Integrating over the tube length and assuming that the period is $4L/a_2$

$$\frac{P_{fr}}{P_2} = \frac{\gamma}{4LD}C_{f2}M_2^2 a_2 \int_0^L (t_2 - t_1)\, dx \tag{3.5}$$

The friction coefficient it is assumed to be equal to that for a completely developed stationary flow.

$$C_f = 0.316Re^{-0.25} \tag{3.6}$$

3.3 Heating limiting factors

3.3.1 Wave steepening limit

One of the factors that set a limit on the maximum attainable temperature for an Hartmann-Sprenger tube was pointed out by Shapiro [8].
Usually a train of compression waves is formed at the cavity mouth and it need to travel a certain distance to become a shock wave.The fact inhibiting energy dissipation within the tube is that a time-mean temperature gradient can prevent a wave from steepening.
Shapiro made the hypotesis of a time invariant temperature longitudinal distribution inside the tube, that is considered as a step like curve with finite temperature jumps ΔT. When an incident wave impinges on the temperature discontinuity there is a resultant transmitted and reflected wave.The resonance tube is, of course, filled with a complex pattern of waves of both families.
At the interface the axial velocities and the pressures matches. From the dynamical equations

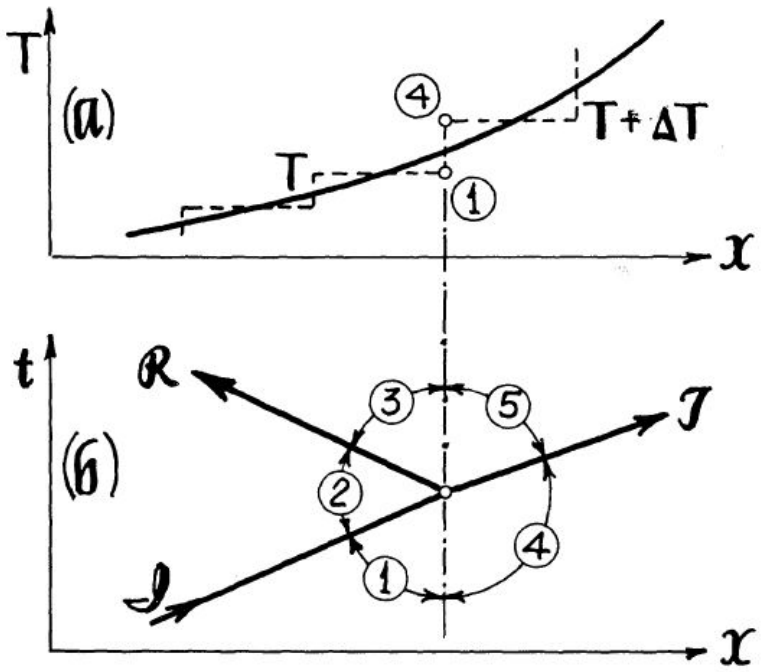

Figure 3.4: Longitudinal temperature distribution and waves reflected and transmitted at temperature discontinuity [8]

for the 3 waves and considering that the temperature jump is the same order of magnitude of the pressure amplitude, assuming that the incident wave is of small amplitude:

$$(u_3 - u_2)/(u_2 - u_1) = -(\rho_4 c_4 - \rho_1 c_1)/2\rho_1 c_1$$

For a prefect gas the acoustic impedance is:

$$d(\rho c)/\rho c = dp/p - (0.5 dT/T)$$

Combining the equations: $(p_5 - p_4)/(p_2 - p_1) = 1 - (T_4 - T_1)/4T_1$ Considering a second wavvelet traveling rightward, δV_w is the excess of velocity of the first wave over the second.

$$\delta V_w = (u_3 + c_3) - (u_4 + c_4) \tag{3.7}$$

$(u_3 + c_3)$differs from $(u_4 + c_4)$ only in the second order. Using the previous results and considering the limit:

$$\delta V_w/\delta x = 0.5(k+1)du/dx + (c/2T)dT/dx \tag{3.8}$$

If $\delta V_w/\delta x$ there is no more wave steepening and viscous dissipation.
Shapiro gives an order of magnitude estimation of the maximum temperature. Considering that for a progressive wave: $du/dx = (1/c)du/dt$, that the tube resonate at a quarter wavelength acoustic frequency and that the particles velocities are in the order of magnitude of the jet velocity, thus of the speed of sound:

$$(du/dx)_{max} = (1/c)(du/dt)_{max} = 8f = 2c/L$$

The maximum temperature rise is then:

$$\Delta T/T = 2(k+1) \tag{3.9}$$

Of course is only an order of magnitude calculation, but gives an explaination of a limiting factor for the temperature rise.
The mechanism can be summarized in this way: as the average temperature in the tube increases, waves require a longer distance to steepen, and a longitudinal temperature gradient itself inhibits wave steepening.

3.3.2 Mass exchange between cold and hot gas

Another limiting factor is the mass exchange between cold flow from the jet and hot flow inside the tube. The following analysis was performed by Brocher [7]. During the inflow phase a certain mass m^* of hot gas passes through the contact surface between extraneous and indigenous flow within the thikness of the boundary layer. The same thing happens to the cold gas in the outflow phase.This behaviour is shown in the next figure, where a coordinate system fixed to the contact surface is used.

The flow inside the tube is highly instationary, so the theoretical study of the boundary layer is complex. In the Brocher analysis the boundary layer is assumed to be like the BL established for a turbolent stationary flow over a plane plate.The velocity profile and the thickness of the boundary layer in this case are:

$$u/u_2 = (y/\delta)^{-1/2}$$

$$\delta(x) = 0.37x(u_2x/\nu_2)^{-1/5}$$

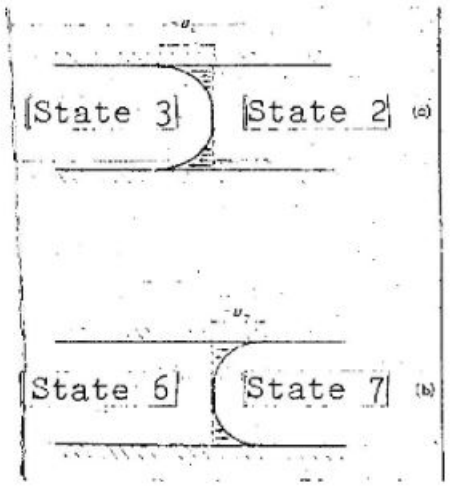

Figure 3.5: Boundary layer profile in a system of coordinates fixed with the contact surface [7]

The final relation for the mass percentage of the hot gas which passes across the contact surface is given by the nex relation:

$$\frac{m^*}{m} = 0.103 \left(\frac{\rho_2}{\rho_1}\right) \left(\frac{L_p}{L}\right)^{4/5} \left(\frac{L}{D}\right)^{4/5} (Re)^{-1/5} \left(1 - 0.137 \left(\frac{L_p}{L}\right)^{4/5} \left(\frac{L}{D}\right)^{4/5} (Re)^{-1/5}\right) \tag{3.10}$$

Where L_p is the penetration distance of the jet, and is a function of the jet mach number, $\frac{\rho_2}{\rho_1}$ can be found by the Hugoniot relations, and $Re = u_2 D/\nu_2$ is the Reynolds number of the tube.
Considering that the enthalpy carried by the hot gass mass passing the contact front is equal to $m^* C_p T_{tot2}$ where T_{tot2} is the average total temperature of the hot gas.The enthalpy carried by the cold gas that sustitute the hot gas during the expansion phase is $m^* C_p T_{tot}$ where T_{tot} is the total temperature of the cold gas. The heat lost by the hot gas in one cycle is:

$$Q_m = m^* C_p (T_{tot2} - T_{tot}) \tag{3.11}$$

Considering that a cycle is almost equal to $4L/a_2$ the energy per unit time $P_m = Q_m a_2/(4L)$. Defining $\theta = T_{tot2}/T_{tot}$:

$$\frac{P_m}{P_2} = 0.25 \frac{\gamma}{\gamma - 1} \frac{m^*}{m} \frac{\rho_1}{\rho_2} \frac{1 + 0.5(\gamma - 1) M_2^2}{M_2} \tag{3.12}$$

3.3.3 Forced convection heat transfer

When the oscillatory motion is established the tube is filled by cold flow and hot flow alernatively. As Brocher [7] pointed out, at a certain position of the tube the wall recieves heat from the hot gas and transfers it to the cold gas.This mechanism of heat removal is not related to the external insulation of the tube, since the heat do not pass from one side to another of the

wall, but the wall acts like a heat sink, as in regenerative heat exchangers.
For the calculation of this heat transfer it would be necessary to know the exact developement of the boundary layer, but as already said it is complex to calculate, thus Brocher made the hypotesis that the heat transfer is the same of a completely developed permanent flow. That's beacuse the boundary layer already exists before the shock wave passes, because of the oscillatory motion of the gas.
Tp(x) is the temperature at abscissa x, Tr is the recovery temperature of the hot flow, h_2 is the heat transfer coefficient in the wall.
During one period the heat given up by the hot gas to the wall is:

$$Q_{cf} = 2\pi D h_2 \int_0^{L_r} (T_r - T_p(x))(t_2 - t_1)\, dx \tag{3.13}$$

Where the heat transfer coefficient is given by the following empirical formula:

$$h_2 = 0.023 \frac{k_2 (Re_2)^{0.8} (Pr)^{0.4}}{D} \tag{3.14}$$

Noting that $(t_2 - t_1) = (1/u_2 - 1/u_{ci})x$, where u_2 is the velocity after the incident shock and u_{ci} is the incident shock wave velocity, and that the period is $T = 4L/a_2$ the thermical power carried off by forced convection is:

$$\frac{P_{cf}}{P_2} = \frac{2h_2 (LL_p)^2}{p_2 u_2 (DL)^2} \left(\frac{1}{M_2} - \frac{a_2}{u_{ci}}\right) \int_0^{L_r} (T_r - T_p(x))(t_2 - t_1)\eta d\eta \tag{3.15}$$

Where $\eta = x/L_p$. The temperature distribution along the axis was found by Brocher and Maresca:

$$\frac{T_p(x) - T_{tot}}{T_p(L_p) - T_{tot}} = \frac{K\eta^3}{1 - \eta + K\eta^3} \tag{3.16}$$

Considering that the temperature at Lp is the same of the hot gas, and that K is a coefficient depending on Prandtl number, geometry and incident and reflected shock velocity [7].
Even ratiation losses have a role in limiting the maximum temperature, but can be trascured in most of the cases.

3.4 Power balance

Having found the main factors that cause and limit heat increase, Brocher and Maresca found a way to define the maximum attainable temperature by the power balance [7].

$$P_m + P_{cf} = P_{irr} + P_{fr}$$

That can be written as:

$$(\phi_m + \phi_{cf}) \frac{\theta + 1}{\theta} = \phi_{irr} + \phi_{fr}$$

Where:$\phi_{fr}(\gamma, M_2, L/D, Re)$,$\phi_{cf}(\gamma, M_2, L/D, Re)$,$\phi_{irr}(\gamma, M_2)$. From this equation the maximum temperature rise is found:

$$\theta = \left(1 - \frac{\phi_{irr} + \phi_{fr}}{\phi_m + \phi_{cf}}\right)^{-1} \tag{3.17}$$

ϕ_{cr}, ϕ_{irr} are increasing functions with M2, the other two are decreasing. At a certain mach, M_{lim} the temperature rise to infinite.But there is another factor to take in account.
When the limiting cycle is reached the velocity inside the tube u_2 is determined only by the jet velocity, but on the other hand the speed of sound a_2 is determined by the total temperaure of the tube T_{tot2}. It follows that M2 is a decreasing function of θ.
This results are summarized in the next figure.

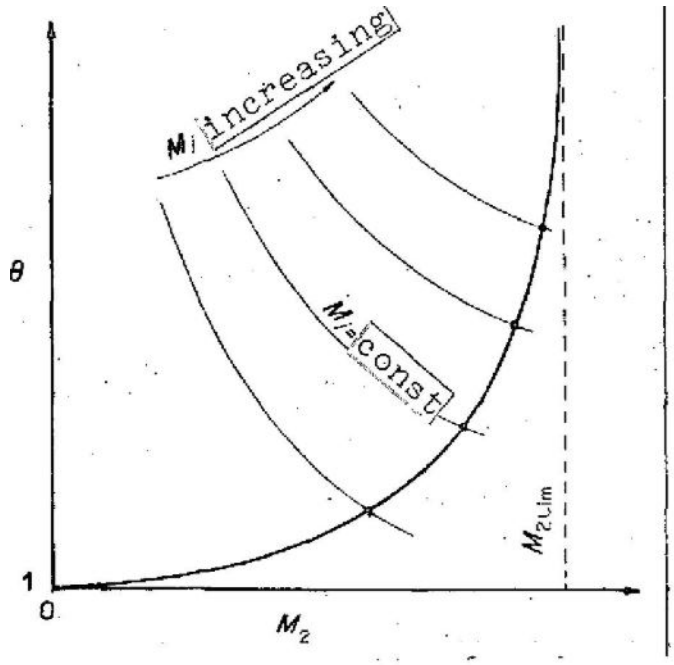

Figure 3.6: Temperature at thermal equilibrum in the tube [7]

The operating point at thermal equilibrum for a certain jet mach number M_j is the interception of the curve $\theta(M_2)$ with $\theta(M_2, M_j)$. The value of M2 at equilibrum is always lower than the limit value, and is increasing with the M_j. So θ is increasing with M_j,and can be infinite only for a jet mach number that tends to infinite.

3.5 1D theoretical model

In this section an example of a 1D model will be shown. The model that will be presented in this section is relatively recent, and was develped by professor Guozhu Liang [9].
Because of the high complexity of the resonance heating phenomenon the model adopts the

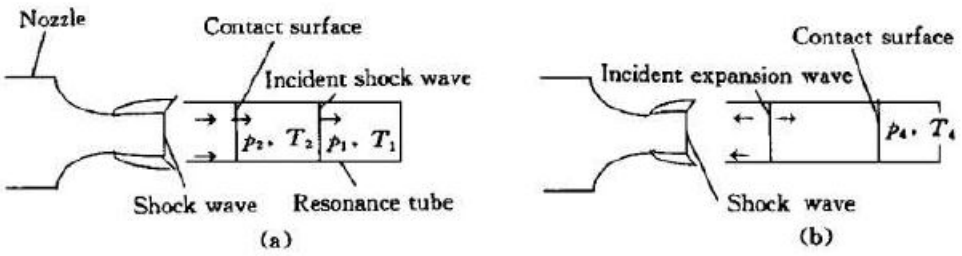

Figure 3.7: Simplified phisical model: Inflow (a) and outflow (b) [9]

following assumptions:

- The tube is considered adiabatic
- The transitory phase is negelcted and the ube works in a stable state
- The fluid inside the tube is indigenous or extraneous, and the indigenous and extraneous fluid are separated by an entropy discontinuity. This contact surface is brought to the tube entrance after each cycle, that means that the inflow acts like a gaseous piston.
- The mixing of the gases at the contact surface is not considered
- The stagnation pressure p_0 and temperature T_0 of the inflow are constant inside the tube
- Three dimensional effects at the tube mouth are neglected

Based on this assumptions and on one-dimensional inviscid flow theory a simple wave diagram that represents the movements of the shock waves and expansion waves was calculated. The diagram is analogous to the one shown in figure 3.1.

A simplified analytical method wasndeveloped on this hypotesis, leading to a prediction of the resonance heating characteristics for different gases. An equation for the ideal maximum resonance temperature was obtained:

$$\frac{T_{max}}{T_0} = \left(\frac{p_0}{p_1}\right)_{cr}$$

Where cr refers to the critical inflow and the pedix 1 refers to figure 3.3.
From the results of the analytical temperature history computation, is clear that the larger is the adiabatic index, the higher is the maximum temperature and larger the gas constant the

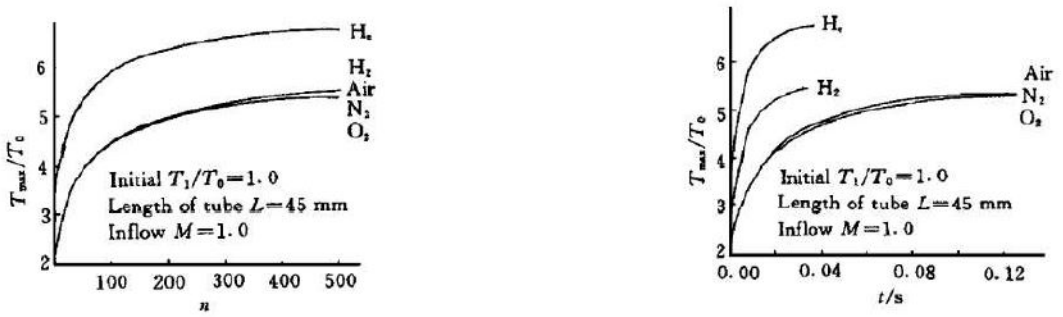

Figure 3.8: Heating curves with respect of number of cycles (n) and time [9]

Gas	k	M	$(p_0/p_1)_{cr}$	f/Hz
Oxygen (O_2)	1.396	32.000	5.958 8	~1 811
Air	1.400	28.965	5.976 3	~1 906
Nitrogen (N_2)	1.400	28.016	5.976 3	~1 938
Hydrogen (H_2)	1.405	2.016	5.998 2	~7 239
Helium (H_e)	1.666	4.003	7.181 7	~5 594

Figure 3.9: Theoretical heating gas properties [9]

shorter the resonance time is. Hydrogen, oxygen, nitrogen and air have the same maximum resonance temperature, that is about 6 times the stagnation temperature, helium instead has a highest temperature about $7.2T_0$. Hydrogen and helium have resonance times about one fifth smaller than those of air,nitrogen and oxygen.[9].
The model can even give a prediction of the length of the high temperature zone, by assuming that is determined aproximately by the maximum deepness of the inflow moving downstream.

$$L_{cs} = L\left(\frac{2}{k+1}\right)^2 \tag{3.18}$$

This model, as all similar models, is quite useful to give some preliminary informations about the heating characteristics of the gases, and can give a good description of the macro laws of the resonance tube heating.In the description of the behaviour of the gases is quite realistic, and it qualitatively reproduce was was stated in the previous chapter.
On the other hand it is quite limited if the aim of the analysis is to go deeper into the phenomenon and even reproduce experimental results. That's because many restrictive hypotesis were done at the beginning. Moreover the model is valid only for a simple cylindric tube, but not for more complex geometries. Since most of the resonance tubes has tapered shape to enhance the heating performance [2], the previosly cited limit make this model not suitable for these applications, where more complex approaches, such as CFD can be more realistic and successful. The same thing is valid for other theoretical models, for example the maximum temperature predicted by Shapiro [8] can only give order of magnitude informations

and the analysis of Brocher [7], as pointed out by the autor itself, can't give a good accuracy in prediction of the hot gas temperature.

Chapter 4

Numerical investigation

4.1 Computational Fluid Dynamics

To analyze the resonance heating phenomenon computational fluid dynamics (CFD) methods will be used.The resonance heating phenomenon has no analytical solution due to its complexity; it involves a compressible transient and turbolent flow and most of the details of this phenomenon are not still well understood, so without CFD it would be impossible to find an accurate solution .
The term CFD refers to several numerical methods used to solve complex 2D or 3D and unsteady flow problems. With CFD a mathematical model of the physical problem and a numerical method are used in a software to do an analysis of the fluid flow. It solves the equation of fluid motion (Navier Stokes equations) numerically and it is useful to produce qualitative and even quantitative predictions of the fuid flow phenomena.

4.1.1 Governing equations

The geometry of this case of study will be an axisymmetric geometry, as seen in most of resonance tube designs and numerical investigations [4]. In this section will be presented all the governing equations that controls the resonance heating phenomenon for a 2D axisymmetric geometry.

Mass equation

For a 2D axisymmetric geometry the continuitiy equation is as follows:

$$\frac{\partial \rho}{\partial t} + \frac{\partial(\rho v_x)}{\partial x} + \frac{\partial(\rho v_r)}{\partial r} + \frac{\rho v_r}{r} = S_m \tag{4.1}$$

Where x is the aial coordinate, r is the radial coordinate, v_x and v_r are respectively the axial and the radial velocity. S_m is a source, it is the mass added to the continuous phase from the dispersed second phase and any user defined source [10]. In the case of resonance heating studeid S_m will be zero.

Momentum equation

For a 2D axisymmetric geometry the momentum equations are as follow [20]:

- **r-momentum**

$$\rho\frac{Du_r}{Dt} = F_r - \frac{\partial p}{\partial r} + \frac{\partial}{\partial r}(2\mu\frac{\partial u_r}{\partial r} + \lambda\nabla\cdot u) + \frac{\partial}{\partial x}(\mu(\frac{\partial u_r}{\partial x} + \frac{\partial u_x}{\partial r})) + \frac{2\mu}{r}(\frac{\partial u_r}{\partial r} - \frac{u_r}{r}) \quad (4.2)$$

- **x-momentum**

$$\rho\frac{Du_x}{Dt} = F_x - \frac{\partial p}{\partial x} + \frac{\partial}{\partial x}\left[2\mu\frac{\partial u_x}{\partial x} + \lambda\nabla\cdot u\right] + \frac{1}{r}\frac{\partial}{\partial r}\left[\mu\left(\frac{\partial u_r}{\partial x} + \frac{\partial u_x}{\partial r}\right)\right] \quad (4.3)$$

Where p is the static pressure,ρ is the density of the fluid, v_x and v_r are respectively the axial and the radial velocity. The F terms are the gravitational body forces and other external body forces. F also contains other model dependent source terms such as porous media and user defined sources. [10]

Energy equation

The following energy equation is valid for a 2D axisymmetric geometry [20]

$$\frac{1}{r}\frac{\partial}{\partial r}\left(k_r\frac{\partial T}{\partial r}\right) + \frac{1}{x}\frac{\partial}{\partial x}\left(k_x\frac{\partial T}{\partial x}\right) + \phi = \rho\frac{Dh}{Dt} - \frac{Dp}{Dt} \quad (4.4)$$

where h is the specific hentalpy, T is the absolute temperature, k_r and k_x are the thermal conductivity of the fluid in radial and axial direction respectively,they appear since the conduction heat transfer is governed by Fourier's law.
ϕ is the dissipation function, it represent the work of friction forces due to velocity gradients which is irreveribly converted in internal energy. For the axisymmetric case is defined by the following equation:

$$\phi = 2\mu\left[\left(\frac{\partial u_r}{\partial r}\right)^2 + \left(\frac{u_r}{r}\right)^2 + \left(\frac{\partial u_x}{\partial x}\right)^2 + \frac{1}{2}\left(\frac{\partial u_r}{\partial x}\right) + \left(\frac{\partial u_x}{\partial x}\right)^2 - \frac{1}{3}(\nabla\cdot u)^2\right] \quad (4.5)$$

Equation of state

For compressible flows the relation between density,pressure and temperature is given by the equation of state. For this study an ideal gas will be condidered:

$$p = \rho RT \quad (4.6)$$

where R is the gas constant.

4.1.2 Turbolence model

Choosing the right turbolence model for the simulation is one of the key issues for a working CFD code. For the simulation in the next chapter the $k-\omega\,SST$ model will be the chosen one.
The $k-\omega\,SST$ model include 2 additional transport equations to represent turbulent properties of flow,the turbolent kinetic energy k and the specific dissipation rate ω, that can be thought as the ratio of the kinetic energy dissipation rate ϵ to k.
The additional equations are the following ones:

$$\frac{\partial(\rho k}{\partial t}+\frac{\partial(\rho k u_i)}{\partial x_i}=\frac{\partial}{\partial x_i}\left(\Gamma_k\frac{\partial k}{\partial x_j}\right)+G_k-Y_k+S_k \tag{4.7}$$

$$\frac{\partial(\rho \omega}{\partial t}+\frac{\partial(\rho \omega u_i)}{\partial x_i}=\frac{\partial}{\partial x_i}\left(\Gamma_\omega\frac{\partial \omega}{\partial x_j}\right)+G_\omega-Y_\omega+D_\omega+S_\omega \tag{4.8}$$

In these equations G_k and G_ω represent respectively the production of turbolent kinetic energy k and the geenration specific dissipation rate ω. Γ_k and Γ_ω represent the effective diffusivity of k and ω.Y_k and Y_ω represent the dissipation of k and ω due to turbulence. D_ω represents the cross-diffusion term. The S parameters are user defined.
This model combines the advantages of $k^\smile\omega$ and $k^\smile\epsilon$ models in predicting aerodynamic flows,that are the robust and accurate near wall formulation for the $k^\smile\omega$ and the free stream indipendence in the far field for the $k^\smile\epsilon$ .In this way it avoids the main problem of the $k-\omega$ model,that is very sensitive to the inlet free-stream turbulence properties, but at the same time keeps the advantage of being directly usable all the way down to the wall through the viscous sub-layer. That's thanks to a blending function that multiplies the $k-\epsilon$ and $k-\omega$ models, designed in order to be one in the near wall region, activating $k-\omega$ model, and zero in the far field region, where $k-\epsilon$ model is active.[10] The model has been validated against many other applications with good results such as turbomachinery blades, wind turbines, free shear layers, zero pressure gradient and adverse pressure gradient boundary layers.

4.2 CFD software: Ansys Fluent

For the CFD analysis of this thesis the software "Ansys Fluent 18.0" was used. It is a professional CFD software that allows to model flow, heat transfer, turbolence and reactions.This software has high performances and it is used for academical and industrial purposes since it can deal with 2D and 3D flows with with steady, transient, laminar, turbolent, compressible , incompressible behavoiour. It is even possible to simulate both gases, liquids or multiphase flows.[10]
Ansys has a working space called workbench, where is possible to set up the mumerical model and solve the problem. In fluent workbench the program shows all the steps the user has to follow to achieve a CFD solution, as shown in figure 4.1 .At each step Fluent provides to the user a specific sub-program to set the geometry(Design Modeler), mesh (Meshing), solution set up (FLUENT), and postprocessing (CFD-post) . All the components are linked to one another by the workbench interface and are easily accessible by the user.

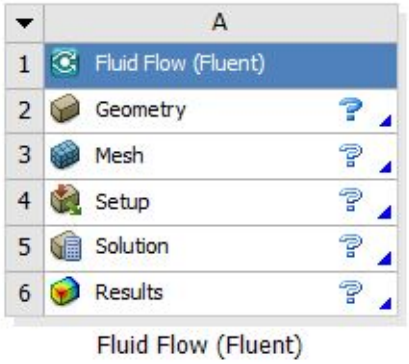

Figure 4.1: Workbench layout

4.2.1 Density based solver

Ansys fluent allows the user to choose between two different numerical methods: Pressure based solver or Density based solver. Historically the first was created for low-speed incompressible flows, the second for high-speed compressible flows.[10]
In bot methods Ansys Fluent will solve governing equations for the conservation of mass and momentum and for energy and other scalars such as turbolence and chemical species by using a control-volume-based technique In the density-based approach, the continuity equation is used to obtain the density field while the pressure field is determined from the equation of state. On the other hand, in the pressure-based approach, the pressure field is extracted by solving a pressure or pressure correction equation which is obtained by manipulating continuity and momentum equations.[10]. In this section will be presented only the density based solver, since the problem of resonance ignition is an high speed compressible transient problem, and the density based solver is more suitable.
In the density based solver approaches the governing equations in a differently from the pressure based method,for each iteration it follow this workflow [10]:

- **1**. Update the fluid properties based on the current solution.
- **2.** Solve the continuity, momentum and energy equations simultaneously.
- **3.** Where appropriate solve equations for scalars such as turbolence and radiation using the previously updated values of the other variables.
- **4.** When interphase coupling is to be included, update the source terms in the appropriate continuous phase equations with a discrete phase trajectory calculation.
- **5.** Check for the convergence of the equation set.

In the density-based solution methods the discrete, non-linear governing equations are linearized to produce a system of equations for the dependent variables in every computational cell. They can be linearized with implicit or explicit formulation with respect to the dependent variable of interest. In summary the implicit formulation solves for all the variables

(p, u, v, w, T) in all cells at the same time. The explicit approach solves for all variables (p, u, v, w, T) one cell at a time. [10]
The implicit formulation allows to obtain a converged steady state solution much faster than the explicit formulation, since it has much better stability characteristics. However the explicit approach requires less memory than the implicit one. For the case of study an implicit formulation will be used in order to achieve a faster convergence.

4.2.2 Pressure based solver

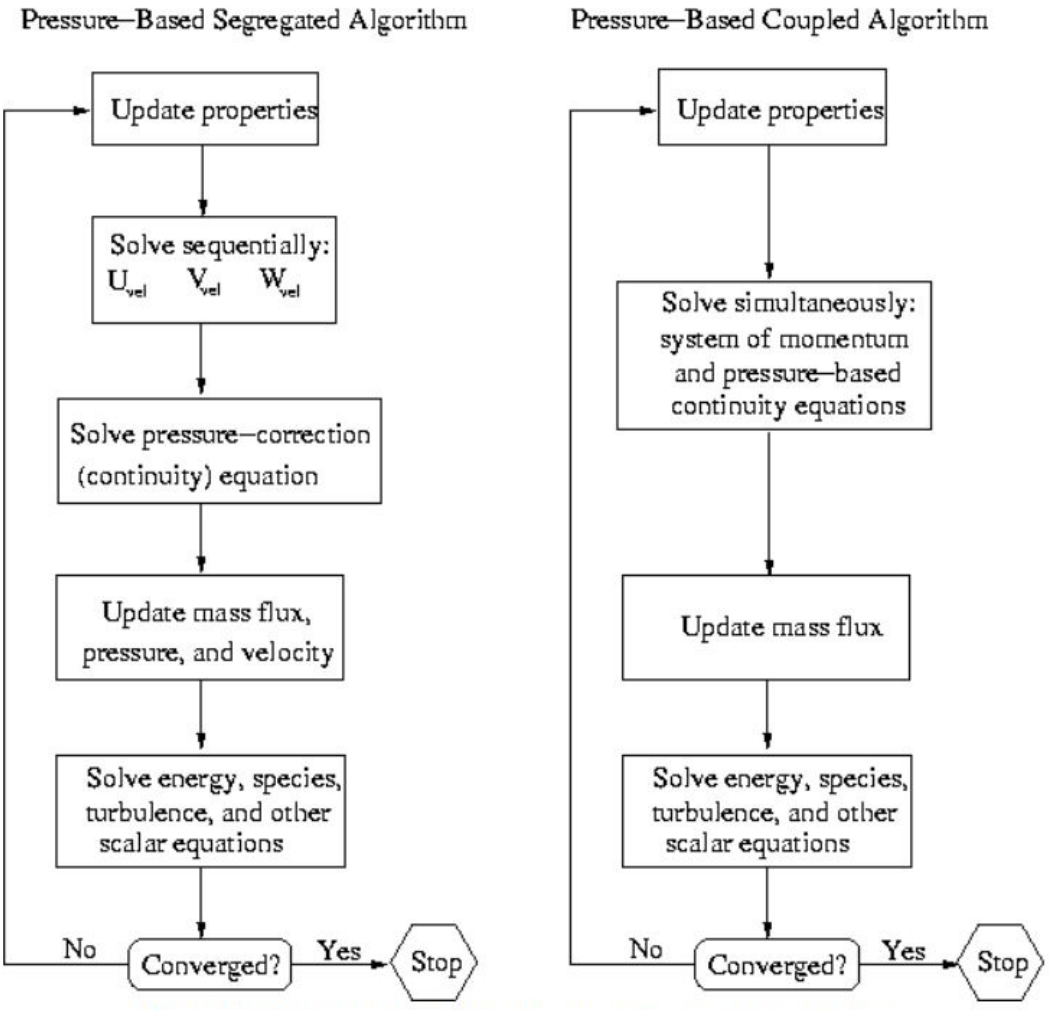

Figure 18.1.1: Overview of the Pressure-Based Solution Methods

Figure 4.2: Pressure based solver algorithms [10]

For the pressure based solver is possible to identify two different algorithms, the segregated and the coupled algorithm.
In the segregated algorithm, the individual governing equations for the solution variables are solved separately one after another. The segregated algorithm is memory-efficient, since the

discretized equations need only be stored in the memory one at a time. However, the solution convergence is relatively slow, since the equations are solved in a decoupled manner.[10].

Unlike the segregated algorithm, the pressure-based coupled algorithm solves a coupled system of equations comprising the momentum equations and the pressure-based continuity equation. Thus, in the coupled algorithm,the momentum and pressure equations are solved in a coupled manner. The remaining equations are solved separately as in the segregated algorithm.

As reported in the fluent manual [10]:"Since the momentum and continuity equations are solved in a closely coupled manner, the rate of solution convergence significantly improves when compared to the segregated algorithm. However, the memory requirement increases by 1.5 - 2 times that of the segregated algorithm since the discrete system of all momentum and pressure-based continuity equations needs to be stored in the memory when solving for the velocity and pressure fields (rather than just a single equation, as is the case with the segregated algorithm)". Moreover the robustness of the simulation is improved, since for transient flows the coupled algorithm is useful to reduce the sensitivity on a poor mesh or large timesteps. Thanks to its stability characteristics, this solver will be chosen for the next simulations, having a better stability behavior than the density based solver. However the pressure based solver has the disadvantage of having a more coarse resolution of the high gradient zones, as shock waves, than the pressure based.

Chapter 5

Simulation with Fluent

5.1 Prior experimental investigation

The numerical simulations that are carried out in the next sections are based on an experimental campaign conduted in 2014 by LFA [11].
The experimental setup they used consists of a convergent nozzle axially movable by a linear actuator.The static pressure in the nozzle and the ambient pressure were measured with Wika A-10 pressure transducers, while the nozzle pressure ratio (NPR) is adjusted by the upstream fluid supply. The resonators were housed in a vacuum chamber with optical access. The temperature in the closed end of the resonator was measured with 0.25 mm Type K thermocouples and the acoustic data were measured with a microphone of type MK301E in the range of 5 Hz to 100 kHz.

As working fluids, pressurized air, oxygen, methane and hydrogen are used. An exper-

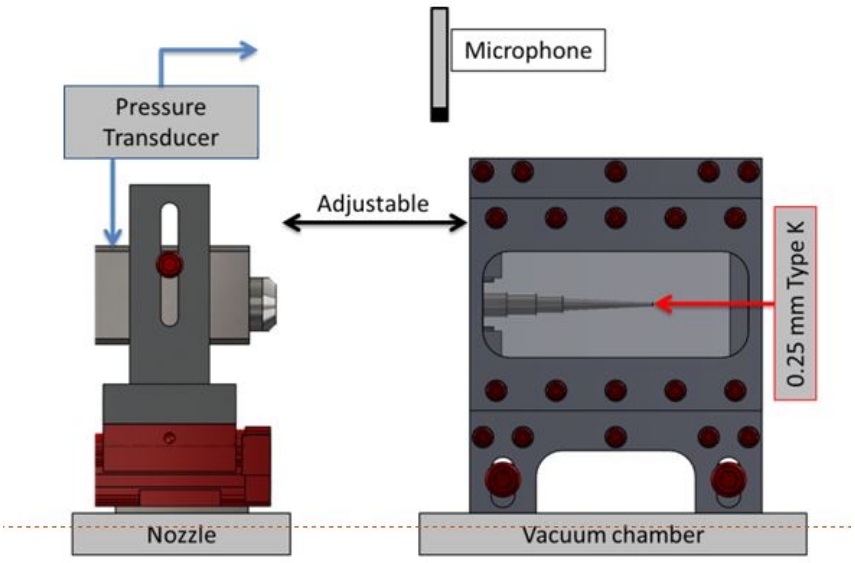

Figure 5.1: Experimental setup for sound and resonator bottom temperature measurement [11]

imental campaign was conducted to find the optimum nozzle-cavity distance to obtain the maximum temperature, by keeping the NPR=4 fixed. As shown in figure the nozzle distance that demonstrated the highest obtainable temperature is s/d= 2.4, and will be selected for the following investigations.

From the graphic can be seen that the conical shape gives higher heating, so this geometry

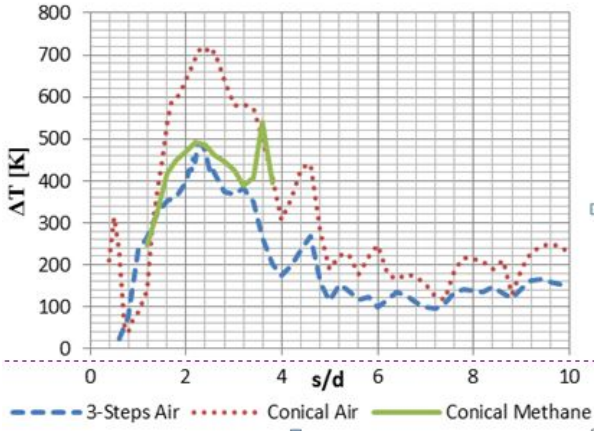

Figure 5.2: Equilibrium temperature for various nozzle distances at a NPR of 4 [11]

will be selected. The two different geometries are shown in figure 5.2. All the dimensional

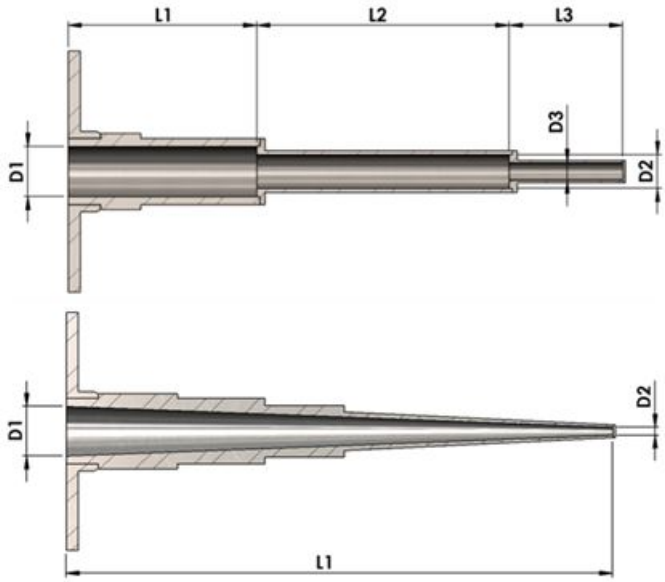

Figure 5.3: Resonator geometries used during the test campaign. [11]

ratios are related to a nozzle exit diameter d of 5 mm. The two types of resonator geometries were built from Inconel, in order to allow high temperatures. Wall thickness are kept as small as possible, in order to reduce axial heat transfer and thermocouple response time.[11]
The following experiments were conducted with air as working fluid, due to low availability of methane and since oxygen gave results quite similar to air.

	D1/d	D2/D1	D3/D1	L1/D1	L2/D1	L3/D1
3 Steps	1.25	0.5	0.25	3.75	5	2.25
Conical	1.25	-	-	11	-	-

Figure 5.4: Resonator geometries dimensions [11]

The final experimental frequency spectrum result refers to the conical cavity filled with air and is plotted for 2 different nozzle-cavity gap distances s/d= 2.4 (the optimum distance) and s/d= 0.8. The microphone response spectrum for both settings is different, as shown in figure 5.4.For s/d= 2.4 an intense heating occurs, accompanied with distinct high-amplitude screeching at 2 kHz, while for s/d= 0.8 no significant heating seems to happen,and only broadband noise beyond 5 kHz could be measured.[11].
The fluent numerical simulation will be run with this last configuration, in order to compare the frequncy spectrum of pressure amplitude and validate the results.

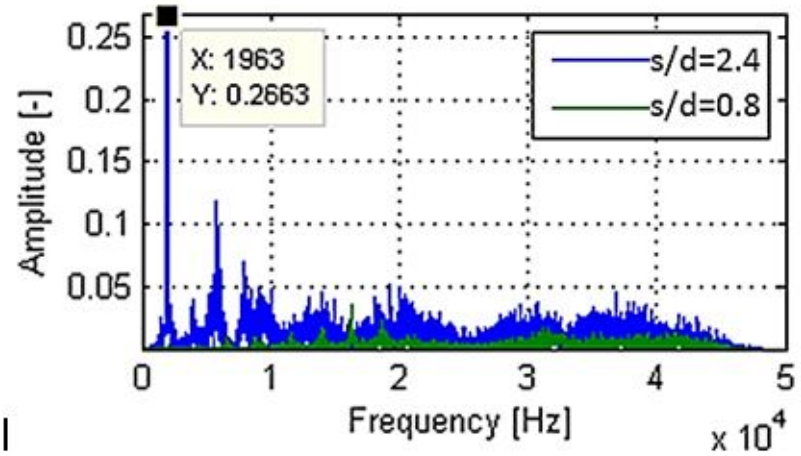

Figure 5.5: Non-calibrated microphone response spectrum for conical resonator at NPR 4 and s/d of 0.8 and 2.4 [11]

5.2 CFD simulation

5.2.1 Geometry

The geometry that is taken in account is a simply tapered axisymmetric 2D geometry. The analysis will start with a conical cavity design made by LTF [11] that was investigated by them both numerically and experimentally. The underexpanded jet is produced by a simply convergent nozzle, it has the same geometry of the one used by LTF [11]. An already tested geometry is chosen in order to validate the simulation results comparing it with the experimental results, for example comparing the pressure amplitude frequency spectrum.
The resonator has the following characteristics:

- Nozzle exit diameter: $d = 5mm$
- Cavity inlet diameter (D) -nozzle exit diameter (d) ratio : $D/d = 1.25$
- Cavity base diameter (D1) Cavity inlet diameter (D) ratio: D1/D=0.16
- Nozzle cavity gap (s)-Nozzle exit diameter (d) ratio: s/d=2.4

  This last value was chosen after an experimental campaign by LTF. The experimental setup allowed to change the nozzle-cavity gap, so a parametric study was possible. Using different conical and 3-steps geometry both with air and methane they found out that the temperature peak in the resonator was for s/d=2.4 for all the cases [11].

- Cavity depth (L)-Cavity inlet diameter (D) ratio : L/D=11

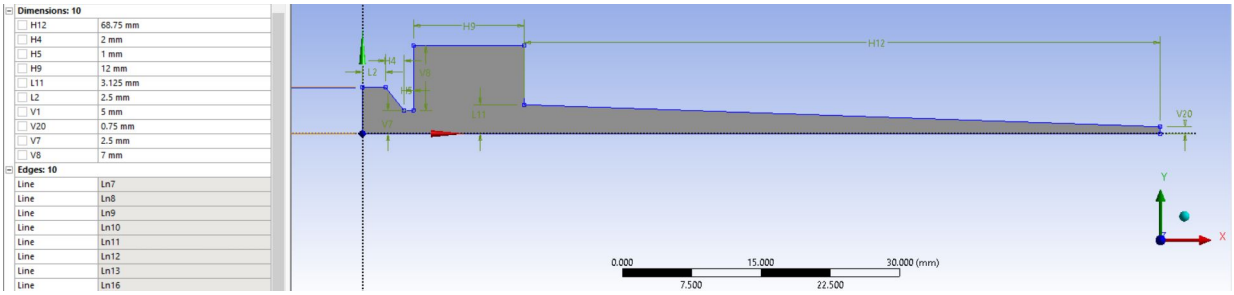

Figure 5.6: Case 1 geometry

5.2.2 Boundary conditions

In this section the boundary conditions are presented. A scheme of the boundaries is presented in figure 5.7.

- **Inlet:** A pressure inlet type was chosen. The inlet pressure imposed is of 405300 Pa, so four times the ambient pressure ($p_0 = 101325Pa$). The aim is to have a NPR=4 as done in the experimental setup tested by LTF [11].

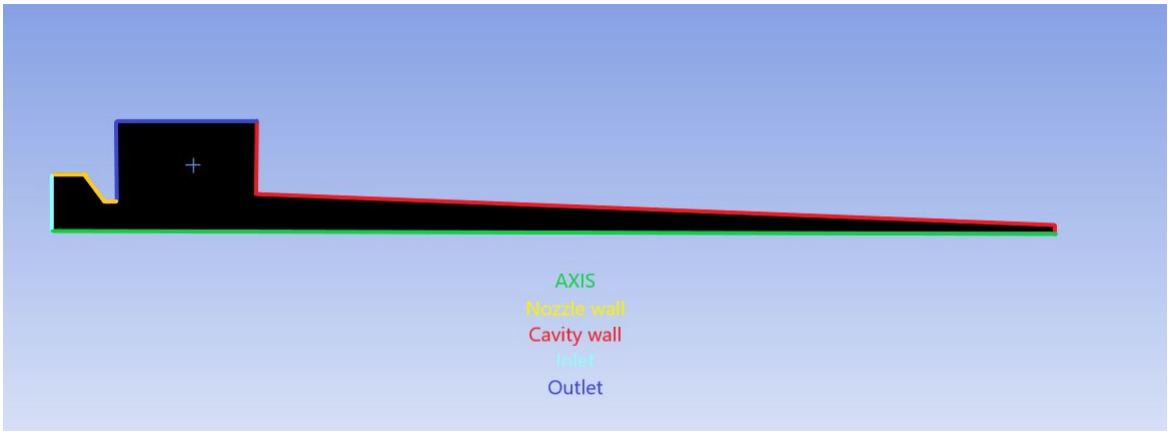

Figure 5.7: Case 1: boundary conditions

- **Walls:** For this first simulation all the walls, both cavity and nozzle walls, are considered adiabatic and no slip shear condition is chosen. The adiabatic walls are set to have a more simple simulation and because the aim of the simulations is to do a validation study against the pressure frequency at the cavity bottom, so it is not necessary to reproduce the exact experimental temperatures.
- **Outlet:** A pressure outlet was chosen, and the pressure was set to 101325 Pa.
- **Axis:** Since the cavity is conical the geometry is axisymmetric, so it was only necessary to model one half of the 2D geometry, setting the axis boundary condition.

5.2.3 Timescales

In order to choose an appropriate timestep for the simulation, is really important to estimate the typical timescale of the problem. Usually this problem can be challenging since resonance heating involves both convection in the fluid and conduction in the walls, and this two phenomena have different timescales. In this case the walls are considered adiabatic, so only the convective timescale is considered.
Convective processes can be characterized by the foundamental frequency of the employed resonator cavity. This foundamental frequency can be estimated by linear acoustic theory, that gives the eigenfrequency f_0 of a conical cavity as [21]:

$$\frac{2\pi f_0}{v} L = \pi - tan^{-1}\left(\frac{2\pi f_0}{v} x_1\right) \tag{5.1}$$

Where L is the cavity length, $v = \sqrt{kRT}$ is the temperature dependent speed of sound, and x_1 is a factor related to the truncation of the cone, considering that the cone mouth is located at x=0, the cone truncated end at x=L and the wide end should be at x=x1+L.
As Bauer pointed out in his paper [22] it is shown that a tapered resonator, as seen from the experiment, has lower frequencies than the one evaluated with the linear acoustic theory, instead it appears to behave like a cylindrical $\lambda/4$ resonator with an additional end correction.

$$f_{0,cyl} = \frac{v}{4(L + 0.4D)} \tag{5.2}$$

This result was evaluated by a matlab code that plotted the frequencies with respect to resonator average air temperature, comparing it with the foundamental frequency measured by Lungu's experiments [11]. The temperature considerated range from 200 to 1000 K.

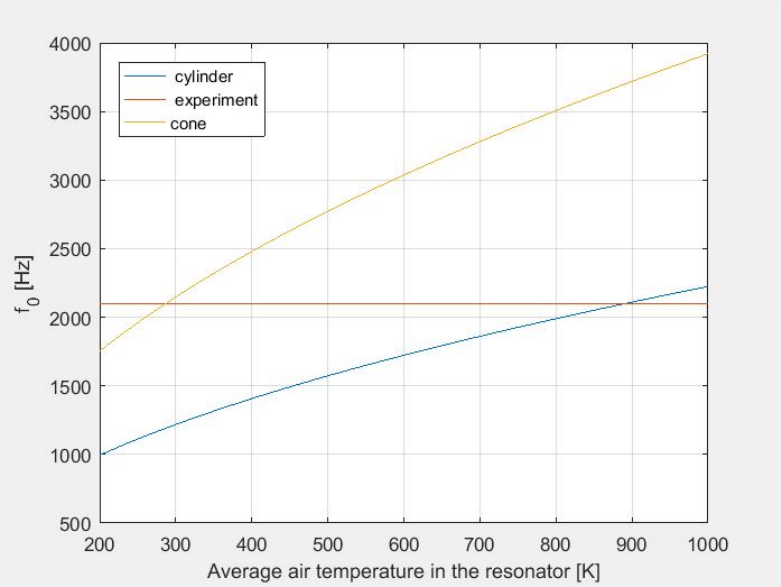

Figure 5.8: Foundamental frequencies for cylindrical and conical cavity compared to experimental frequency

Looking at this graphic it can be seen that the linear acoustic theory is not sufficient to describe the oscillation in the resonator cavity.In order to have a more reliable estimation of timescales the experimental foundamental frequency is considered. From the experiments $f_0 = 2100Hz$ and from this the convective timescale is obtained: $\tau_{conv} = 0.47ms$.

5.3 Mesh

5.3.1 Modeling the boundary layer

Having an high resolution on the near wall zone is an important task for a resonance igniter simulation, since one of the heating mechanisms,except the heat dissipated by the shock waves, is heat dissipation due to friction of the flow against the cavity walls.
In order to achieve better results in the boundary layer it is necessary to adapt the mesh to yeld a maximum $y^+ = 1$, since it is the most suitable value for a $k-\omega$ SST turbolence model. Based on previous mesh sensitivity studies a recommended best practice mesh guideline is a $y+ \cong 1$ [10] . As seen in previous studies [7] one of the phenomena contributing the heating inside the tube is heat dissipation due to friction on the walls, so it is quite important to refine the mesh in the boundary layer.
As shown in the "Ansys Fluent Theory Guide" [10], the y+ should not be higher than 1, but even values smaller than 0.001 should be avoided, since the trnasition position seems to translate downstream,this is presumably caused by the large surface value of the specific turbulence frequency , which scales with the first mesh node height. The fluent guide show some example of the effect of different values of y+ on the stream over a flat plate, as shown in figure:

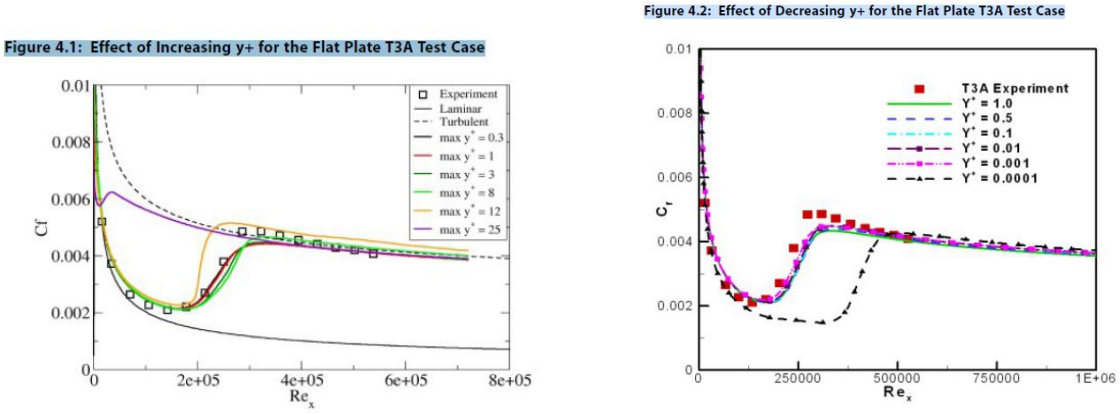

Figure 5.9: Effect od increasing or decreasing y+ for the stream over a flat plate [10]

That's why the boundary layer was modeled following the latter guidelines. The first cell height $\triangle y_1$ was computed in order to give as a result a wall y+ value around 1 both for the nozzle and the cavity walls. The equations used to compute this value are the following:

$$Re = \frac{\rho U D}{\mu} \tag{5.3}$$

$$\triangle y_1 = \frac{y^+ \mu}{U_\tau} \tag{5.4}$$

The last equation come from the definition of dimensionless wall distance y+. U_τ is called as friction velocity and it is defined as: $U_\tau = \sqrt{\frac{\tau_w}{\rho}}$, where $\tau_w = 0.5 C_f \rho U^2$ is the wall shear

stress and it is proportional to the skin friction coefficient C_f
A source of uncertainty for this calculation is the definition of the friction coefficient, since it is defined by experimental relationships. For an internal flow:

$$C_f = 0.079Re^{-0.25} \tag{5.5}$$

This is only a preliminary calculation, the free stream velocity changes with the time and the Reynolds number is not accurate since the tube is convergent.
Looking at the y+ distribution along the cavity walls at $t = 0.705ms = 1.5\tau_{conv}$ it is possible to see that the first cell height found in this way is sufficient to achieve the y+ values reccomended by the manual.

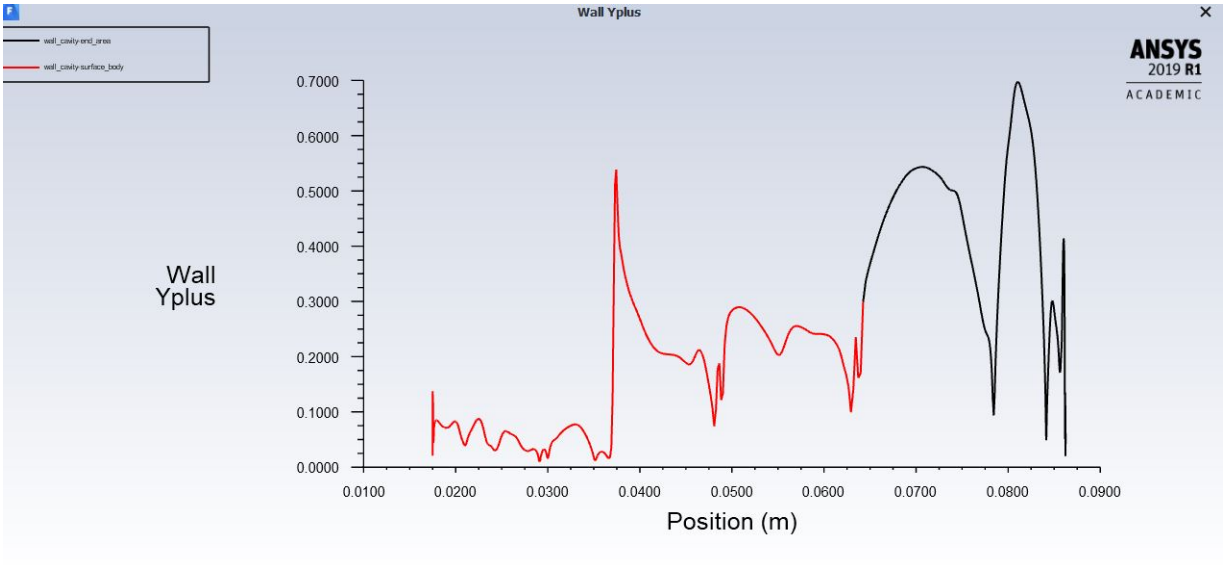

Figure 5.10: Y+ of the cavity walls at t=0.7 ms

After calculating the desidered first cell height the mesh was generated by using the Fluent mesher. Since the geometry is simple and two dimensional was possible to have a fully structured mesh, so all the elements are quadrilateral. Having a structured mesh gives the great advantage to have a better convergence.
Two important zones were refined more than others. The first one is the cavity entrance edge, because in this zone in the first phase of the outflow there is a Prandtl-Meyer expansion, due to the exit of the fluid [6]. Moreover there are many vortex originating from there because of the outflow.
The second one is the nozzle exit edge. In this zone originates the underexpanded jet, so it is important to refine this edge since there is a supersonic expansion that starts from here. The nozzle is simply convergent and is designed in order to have sonic throat and to create an underexpanded jet, so nozzle throat pressure is higher than ambient pressure.The sructure of an underexpanded jet is shown in figure 5.10.
The mesh must even be refined enough to catch the shocks of the jet and the traveling shocks inside the tube. While creating the mesh more attention was put in the mesh quality.

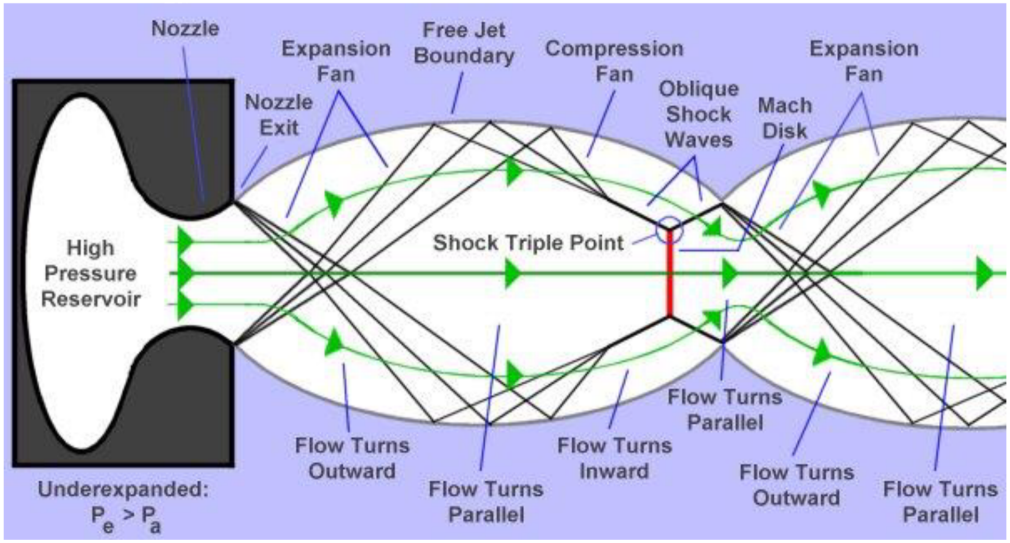

2

Figure 5.11: Underexpanded jet structure

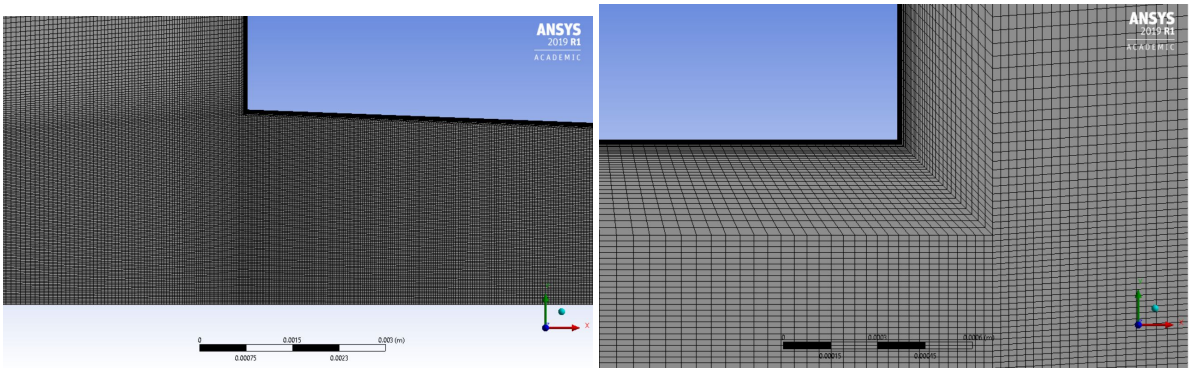

Figure 5.12: Mesh details of the cavity entrance and the nozzle exit

5.4 Setup summary

In this section the setup used for the simulation is summarized.
The geometry is axialsymmetric, so it is considered as 2 dimensional and only half of the tube is modeled.
The viscosity is taken in account in this model. The turbolence effect is considered by using the $k - \omega$**SST** turbolence model. This model was chosen because of its robustness and accuracy in the near wall zone, even for separating boundary layers, so seems to be the most suitable for this case, where the flow is often changing direction and adverse pressure gra-

dients are possible.The turbolence must be taken in account because of the high Reynolds numbers inside the tube, that had been deteced in many experiments for this kind of phenomenon [7].
Since the thermal effect are of primary importance and the flow is compressible the energy model is switched on.
The fluid is modeled as an ideal gas, since the flow is compressible and the density variations are noticeable. The ideal gas model is selected because this model is still valid for the temperature and pressure ranges typical of this application and the intermolecular interactions can be ignored (the model fails for high pressures and low temperatures). The other fluid properties such as Cp and viscosity are considered in a first case constant and in another one variable with temperature.
The chosen solver is the pressure based one, specifically the coupled version of it. This solver was preferred over the density based solver and the segregated algorithm pressure based for stability reasons. For transient simulation the coupled pressure based is less sensible to poor meshes and timesteps, moreover the rate of solution convergence increases beacuse the momentum and pressure equations are solved in a coupled manner.
All the spatial discretization schemes for pressure,density,temperature, momentum and turbolence equations hae second order accuracy.
For the initial conditions an **hybrid initialization** mehtod is used.It solves the Laplace equation to produce a velocity field that conforms to complex domain geometries, and a pressure field which smoothly connects high and low pressure values in the computational domain. All other variables will be patched based on domain averaged values or a predetermined recipe [10].
For the temporal discretization a timestep of $2 * 10^{-8}s$ is chosen, as will be justified in the timestep study this timestep is sufficient and gives low temporal discretization errors. The temporal discretization has a first order accuracy, it was chosen to give the problem an higher stability, despite having higher dissipation errors.

Chapter 6

Verification of the CFD code

The term verification in CFD field is defined as:

"The process of determining that a model implementation accurately represents the developer's conceptual description of the model and the solution to the model." [23]

In the verification process is necessary to find the errors in the model and its solution. The main error sources that must be checked are: insufficient spatial or temporal discretization convergence, lack of iterative convergence, and computer programming. The methods to do this will be presented in the next chapters. Part of the iterative convergence check is the consistency analysis on the solution.
Another part of the verification assessment is the comparison with higly accurate solutions, such as analytical, benchmark PDE or ODE solutions and in this phase computer programming errors are estimated.[23] However this part will be not assessed in this thesis, due to the absence of highly accurate analytical solutions or benchmark solutions.As shown in chapter 3, all the theoretical analysis done up to now can give only order of magnitude informations and are valid for simple geometries, so are not useful for this case. The only accurate solution could be the one of the shock tube, but the results are not comparable.
Verification activities are primarily performed early in the development cycle of a CFD code. The process must be dome again for every code enhancement or modification. The level of accuracy required for this phase is much higher than in the case of validation. Usually the verification process is easier for the steady flows, the unsteady case is still not totally understood [23].

6.0.1 Mesh sensitivity study

In this section a mesh sensitivity analysis is carried out. The geometry is simple, so it is possible to have a fully structured quadrilateral mesh , as seen in previous studies [4]. The aim of the analisys is to choose the mesh size, finding a compromise between computational speed and results accuracy. Usually finer is the mesh more accurate the results will be, but the computational time will considerably increase.
To estimate the mesh discretization error, the procedure reccomended by Fluids Engineering Division of ASME [24] will be used. The recommended method for discretization error esti-

mation is the Richardson extrapolation (RE) method, up to now is the most reliable method to calculate numerical uncernainty, but it is necessary to be aware of its limitations: the local RE values of the predicted variables may not show a smooth, monotonic dependence on grid resolution, and in a time-dependent calculation, this non-smooth response will also be a function of time and space. [24]
The Richardson Extrapolation method will be implemented by using the following procedure:

- **1)** The first step is to define a representative grid size. Since the case geometry is 2D the following expression will be used [24]:

$$h = \sqrt{\frac{1}{N}\sum(\triangle A_i)} \tag{6.1}$$

  Where N is the number of cells and $\triangle A_i$ is the area of the i-th cell.

- **2)** The next step is to select at least 3 different grids and to run simulations in order to determine the values of the main variables of interest. The three meshes are supposed to be significantly different, it is desiderable to achieve a refinement factor $r = h_{coarse}/h_{fine}$ greater than 1.3. This value s based on experience, and not on formal derivation. While doing the refinement a use of geometrically similar cells is preferable [24]
  In that case the refinement will be done by maintaining the boundary layer first cell heigth, in order to keep the y+ values compatible with the turbolence model mesh requirements.

- **3)** Considering that $h_3 > h_2 > h_1$ and $r_{21} = h_2/h_1$, $r_{32} = h_3/h_2$, it is necessary to calculate the apparent order 'p' of the method.

$$p = \frac{1}{ln(r_{21})} \mid ln \mid \epsilon_{32}/\epsilon_{21} \mid + q(p) \mid\mid \tag{6.2}$$

$$q(p) = ln\left(\frac{r_{21}^p - s}{r_{32}^p - s}\right) \tag{6.3}$$

$$s = sign(\epsilon_{32}/\epsilon_{21}) \tag{6.4}$$

  where $\epsilon_{32} = \phi_3 - \phi_2$,$\epsilon_{21} = \phi_2 - \phi_1$ and ϕ_k is the solution of the k-th grid. This equation can be solved with fixed term iteration method with initial guess equal to first term.

- **4)** Calculate the extrapolated values from:

$$\phi_{ext}^{12} = (r_{21}^p \phi_1 - \phi_2)/()$$

- **5)** Calculate the following error estimates, along with the apparent order p:
  Approximate relative error:

$$e_a^{21} = |\frac{\phi_1 - \phi_2}{\phi_1}| \tag{6.5}$$

The fine grid convergence index:

$$GCI_{fine}^{21} = \frac{1.25 e_a^{21}}{r_{21}^p - 1} \tag{6.6}$$

The GCI is a measure of the percentage the computed value is away from the value of the asymptotic numerical value. It indicates an error band on how far the solution is from the asymptotic value. It indicates how much the solution would change with a further refinement of the grid. A small value of GCI indicates that the computation is within the asymptotic range.The value 1.25 is a safety factor F_s, its value is 1.25 if the used grids are three, but when having 2 grids it raise to 3.
It is useful to define the convergence ratio, in order to classify the convergence condition of the variables:

$$R = \frac{\Phi_2 - \Phi_1}{\Phi_3 - \Phi_2} \tag{6.7}$$

So as mentioned by Roache we have :

- Monotonic convergence : $0 < R < 1$
- Oscillatory convergence: -1 $< R < 0$
- Monotonic divergence: $R > 1$
- Oscillatory divergence: $R < -1$

This classification is only possible if the available grids are no more than 3. It is useful to know the variables behavior, since the Richardson extrapolation method works best with monotonic convergence.

Results

For the mesh convergence study is necessary to compare even the distribution of temperature and pressure along the axis and show the discretization error bars. One possible approach is to compare the variables distribution for the same timestep and calculate the corresponding error bars. This method is limited by the different shock wave traslation velocity inside the tube for the 3 different meshes. As shown in figure 6.1 the position of the shock wave is closer to the cavity entrance by increasing the mesh density. Since for $t = 1.5\tau_{conv}$ we are in the outflow phase it is right to state that the shock wave moves faster by increasing the mesh density. This difference in traveling velocity is not related to the phisycs of the problem, but only to numerical reasons.

To have a more reliable comparison it is necessary to compare the results for the same shock position. After choosing a desired position of the shock it is necessary to choose the right timestep in order to achieve the same position for each mesh. The position chosen is the shock position of the fine grid x=0.038 m.

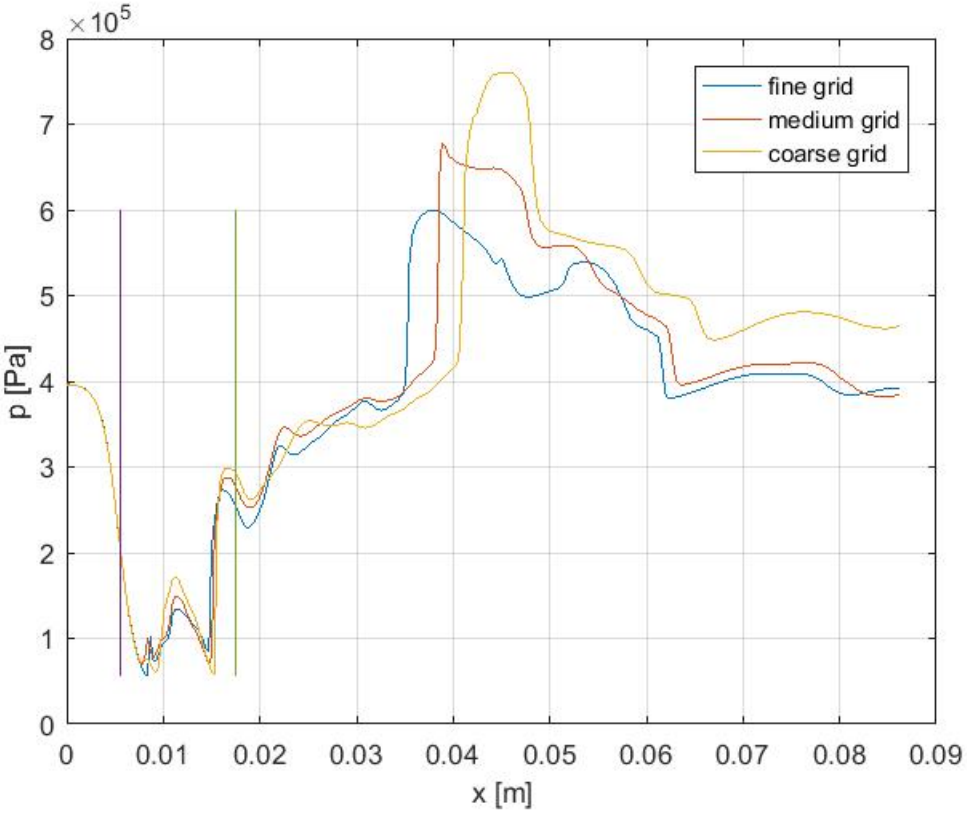

Figure 6.1: Pressure axial distribution at $t = 1.5\tau_{conv}$ for the 3 different meshes

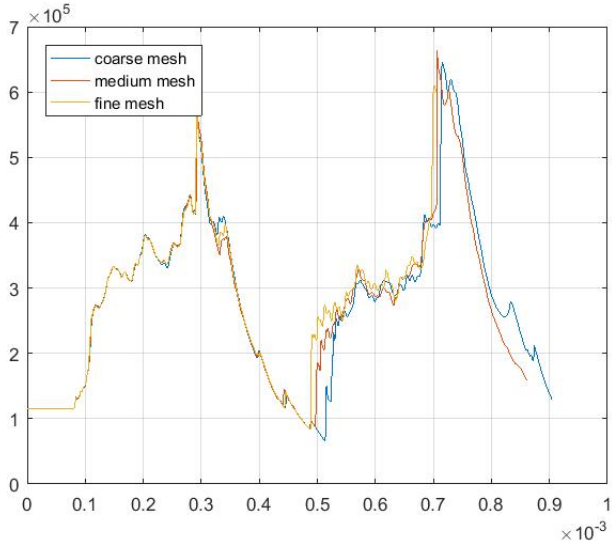

Figure 6.2: Pressure history

Looking at the pressure history of this point the timesteps were chosen in order to have a peak in the pressure, that indicate that the reflected shock is positioned at that point. The three selected timesteps are: $t_{fine} = 0.7ms$, $t_{medium} = 0.7081ms$, $t_{coarse} = 0.7152ms$. The

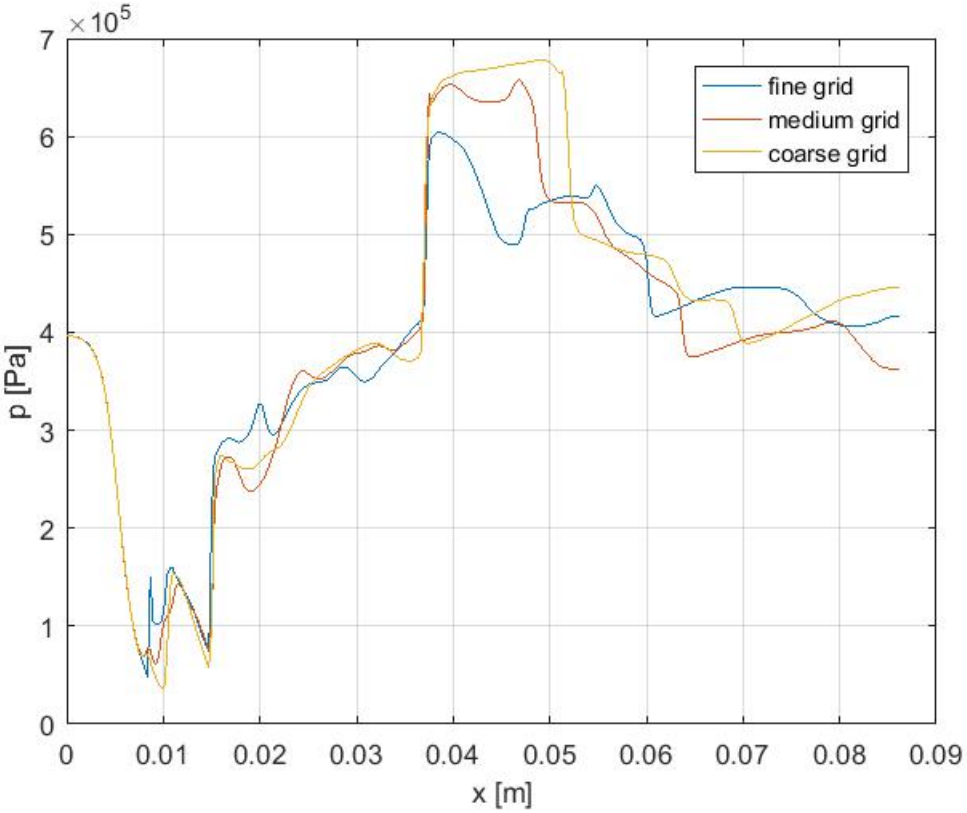

Figure 6.3: Pressure axial distribution at for the 3 different meshes for the same shock position

pressure distribution for the 3 meshes with the new selected timesteps are shown in figure 6.3 and, as it is possible to notice, the shocks have almost the same position, so now it is possible to have a more reliable mesh convergence study.

	Average cavity base temperature (K)	Average cavity base Pressure (Pa)
N1 N2 N3	236120 119080 59385	236120 119080 59385
r_{21}	1.408	1.408
r_{32}	1.41	1.41
Φ_1	637.46	392318.4
Φ_2	643.94	383329.13
Φ_3	814.44	464194.3
p	9.23	6.343
e_a	1.02 %	2.28%
GCI_{fine}	0.054 %	0.37 %
R	0.0380	-0.1105

Table 6.1: Mesh influence at $1.5\tau_{conv}$

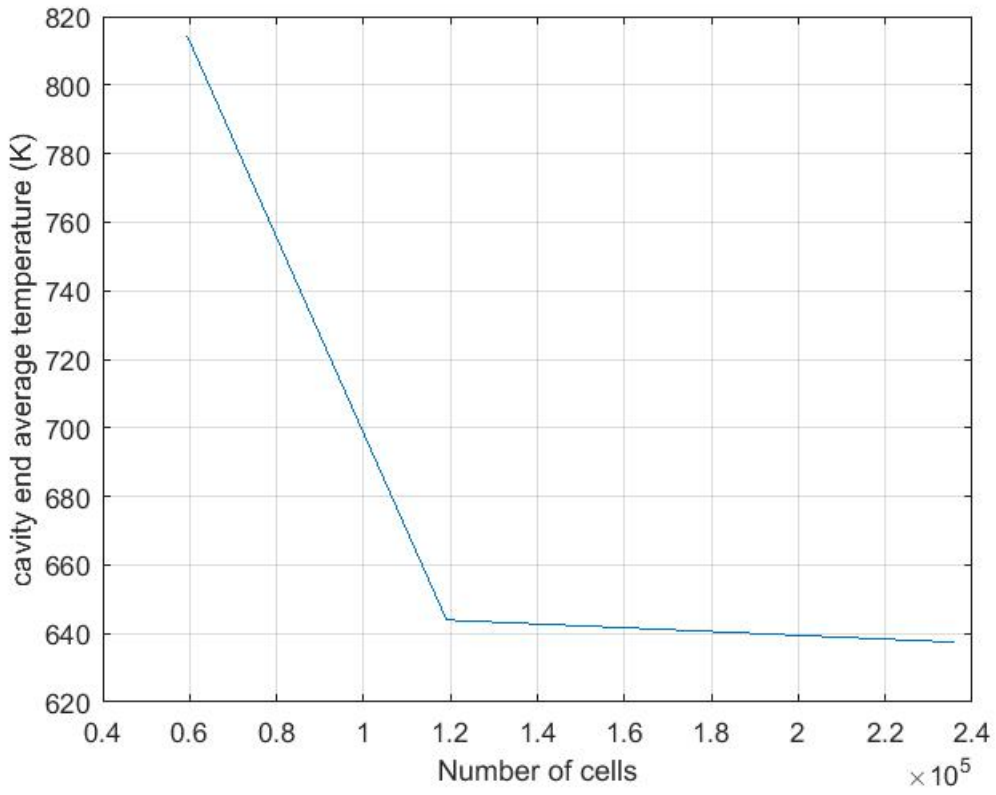

Figure 6.4: Cavity base temperature with respect to mesh refinement at $t = 1.5\tau_{conv}$

The first step is to monitor how the most important variables related to ignition behave by changing the grid resolution. The ignition usually starts at the cavity tip, since the highest temperatures are usually in this position, that's why the cavity base pressure and temperature need to be monitored as most important parameters.
As the plot and the table shows, the cavity base temperature shows a monotonic convergence, as the convergence ratio R tells us. The GCI error is even quite low, so it is possible to state that we are in the asympotic range for this parameter. For the pressure at the resonator tip the behavior is different, since $-1 < R < 0$ we detect an oscillatory convergence, but the GCI is quite low (3.7%) so even for this value the error bar size is acceptable and the value is close to the asymptotic range.

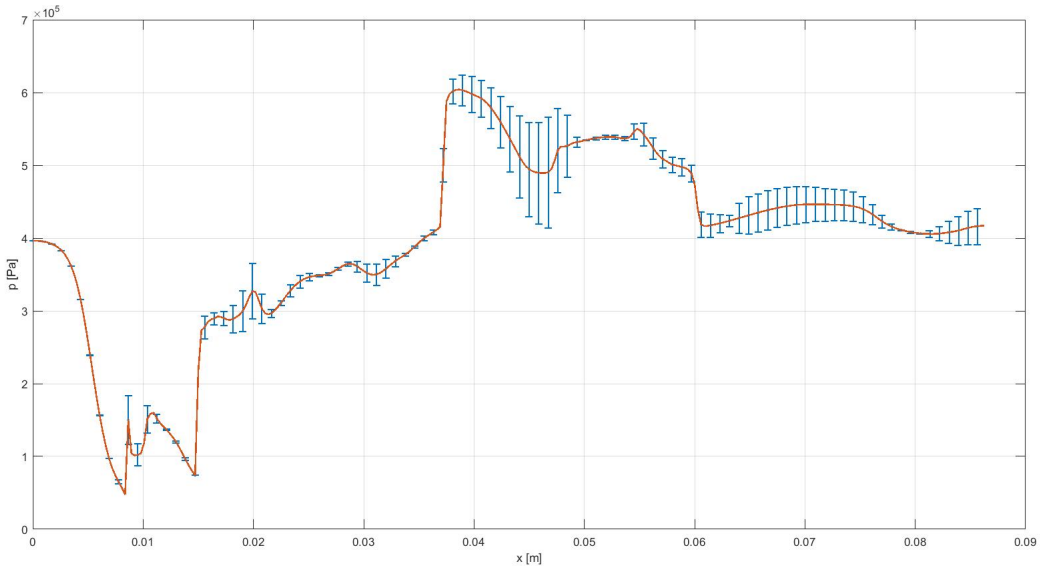

Figure 6.5: Axial distribution of pressure for the 2e-8 s timestep and with the finest mesh

Looking at the axial distribution of temperature and pressure is possible to see the error bars. The bigger error bars are detected in high gradient areas, for example after the shock waves, especially for the pressure the error bars magnitude raise after the traveling shock wave, that travels towards the left, and even after the mach disk of the underexpanded jet. For the pressure the maximum GCI error is located after the reflected shock inside the cavity,and it is around 20%. For the temperature the behavior is similar, but the maximum is located in the underexpanded jet first shock and its around 12.7%.
It is possible to say that for this variables the asymptotic range is not achieved in all the domain, especially in the area after the shocks. Furthermore, for both temperature and pressure, oscillatory convergence is detected in various positions, as expected for a transient simulation with high gradient zones. But, even if the discretization errors are high it is possible to say that they do not affect in a consistent way the ignition prediction capability of the simulation. To state that the error is low enough is necessary to look at the minumum auto ignition temperature for methane-air mixtures. The MAIT is the lowest temperature at wich spontaneous

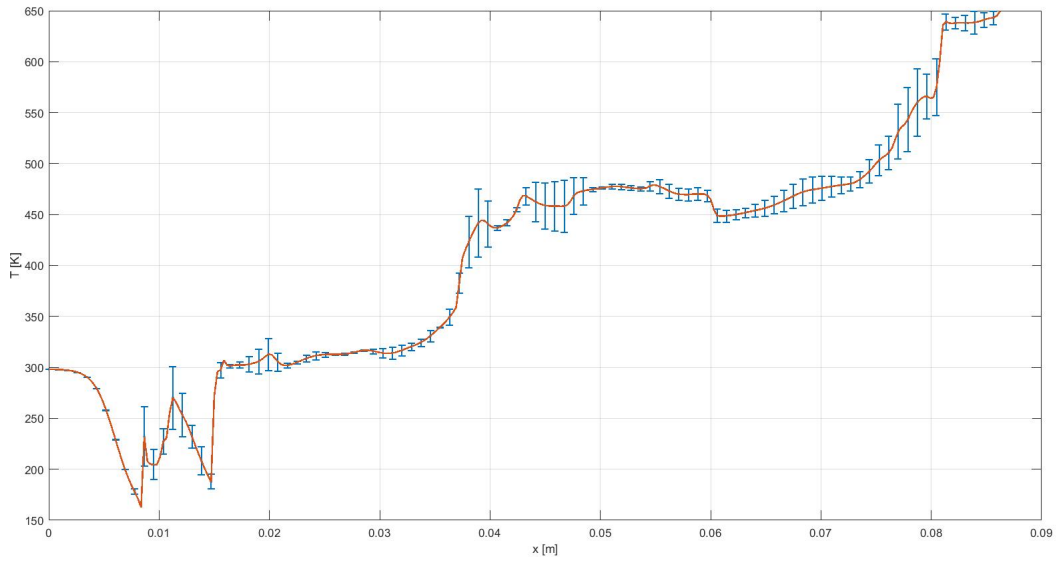

Figure 6.6: Axial distribution of pressure for the 2e-8 s timestep and with the finest mesh

ignition (without external ignition sources) occurs.
For the minimum autoignition temperature the experimental work of C. Robinson and D.B. Smith [12] is taken in account as reference. In this experimental campaign a roughly spherical test vessel was used, made of stainless steel. Fuel and air were premixed to allow good control of the mixture composition. Although the vessel was closed, a relief valve ensured that ignitions were carried out at constant pressure, very close to atmospheric.[12]
Looking at the figure is clear that the temperatures of ignition at atmospheric conditions are quite lower than the maximum temperature that the resonator tip can rise,even far from stechiometric conditions, and the discretization error is too low to affect the ignition capability of the igniter.
The discretization error on the temperature profile is compatible with the auto ignition temperature of the methane-air mixture. From the experiments [11] (figure 5.1), an increase of temperature of around 700 K was detected for the chosen nozzle-cavity gap, NPR, and using air as working fluid, so the maximum temperature of the resonator tip can reach around 1000 K. Condidering that the temperature discretization error is around 12.7 % the error over the maximum achiaveble temperature estimated before is about $\pm 127K$, and that value doesn't affect the ignition capability for a methane-air mixture, that, as it is possible to see from the experiment results, is not higher than 650 K even far from stechiometric conditions.

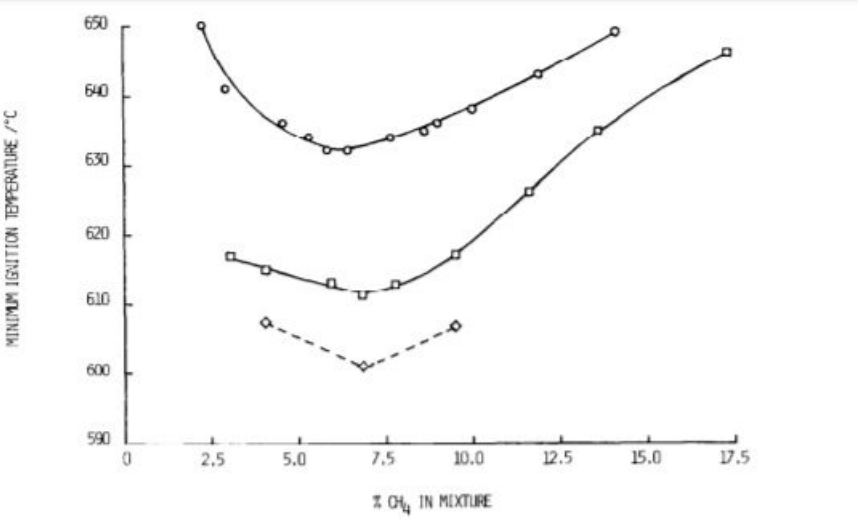

Fig. 1. Auto-ignition temperatures of methane—air mixtures: variation with stoichiometry. □ — this work, untreated vessel; ◇ — this work, boric acid coating; ○ — Naylor and Wheeler [5].

Figure 6.7: Autoignition temperature of air-methane mixture with respect to methane concentration [12]

6.0.2 Temporal discretization sensitivity

As well for the spatial discretization, a convergence study is necessary even for the time discretization. As well as done in the mesh indipendence study, 3 different timestep sizes will be investigated, and the relative discretization error will be evaluated with a GCI method adapted for a timestep influence study, even though CGI was first developed for an uncertainty quantification regarding mesh resolution.
Three different simulations were carried out with different timestep sizes: 40 ns, 20 ns, 12 ns for $1.5\tau_{conv}$. The distance between the timesteps was chosen in order to have a refinement factor at least equal to 1.3, as reccomended in ASME journal procedure for estimation and reporting of uncertainty [24].

It is possible to notice that, as espected, the discretization error rises in points with high gradients, for example in the zone of the shock wave front, as it is possible to see expecially in the pressure and density plots.
Looking at the temperature plot, it is possible to see that te maximum relative discretization error (GCI) is around 3.95 %. The simulation seems to have not considerable changes by decreasing the timestep size, so it is possible to say that it is not necessary to use the lowest timestep, since the increase of computational cost is not justified.
The discretization error on the temperature profile is compatible with the auto ignition temperature of the methane-air mixture. From the experiments [11] (figure 5.1), an increase of temperature of around 700 K was detected for the chosen nozzle-cavity gap, NPR, and using air as working fluid, so the maximum temperature of the resonator tip can reach around 1000 K. Condidering that the temperature discretization error is around 3.95 % the error over the maximum achiaveble temperature estimated before is about $\pm 39K$, and that value doesn't af-

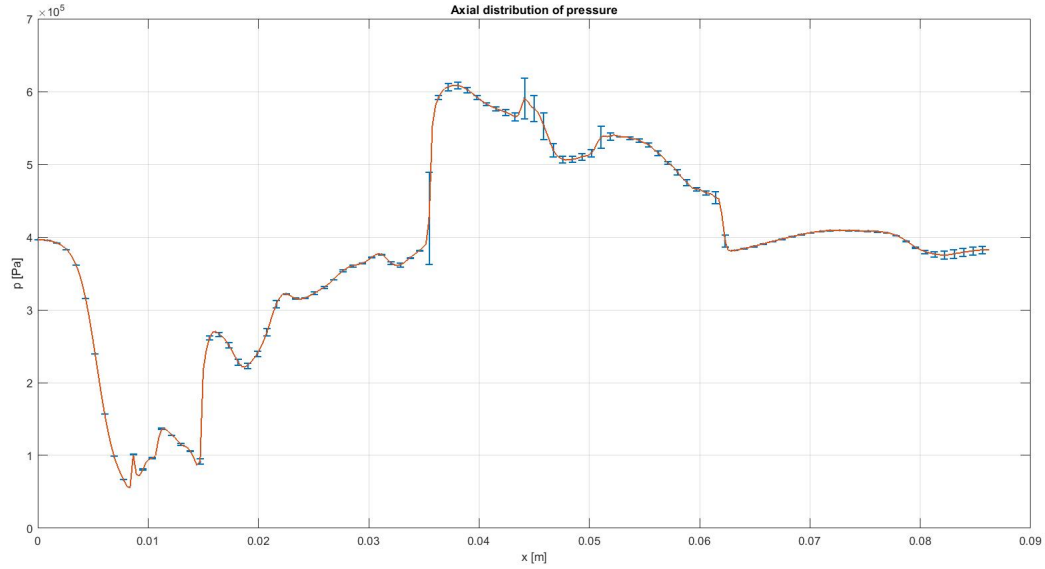

Figure 6.8: Axial distribution of pressure for the finest timestep and with the finest mesh

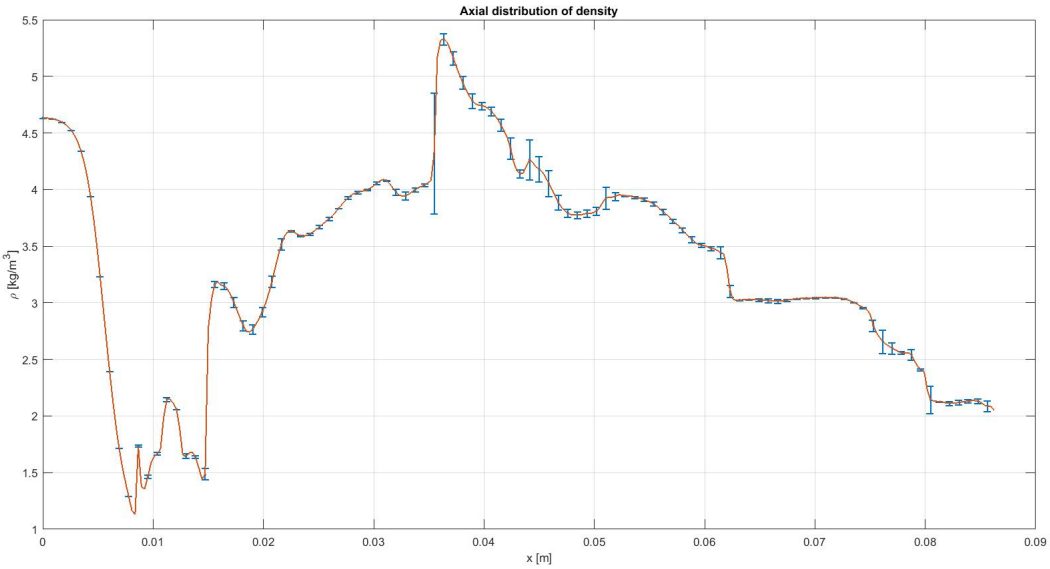

Figure 6.9: Axial distribution of density for the finest timestep and with the finest mesh

fect the ignition capability for a methane-air mixture. The considerations are the same done for the case of spatial discretization error.

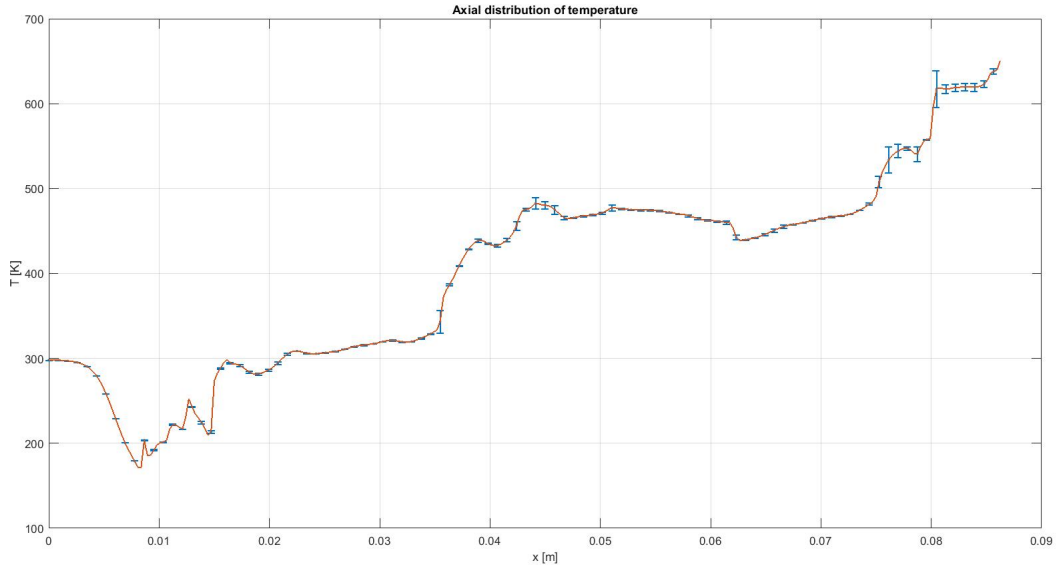

Figure 6.10: Axial distribution of pressure for the finest timestep and with the finest mesh

6.0.3 Examination of consistency

Examining consistency is one of the most important steps in the verification process of a code. Consistency verifications consists in cheking if the most relevant conservation principles are satisfied.In this case, since the walls are adiabatic, the heat balance will be not considered and the checks will be focusing on the mass flow balance between inlet and outlet.
Looking at the mass flow rate history until $t = 1.5\tau_{conv}$ a mass flow imbalance was noticed, and is related to a reversed flow condition taking place in the outlet for several timesteps.

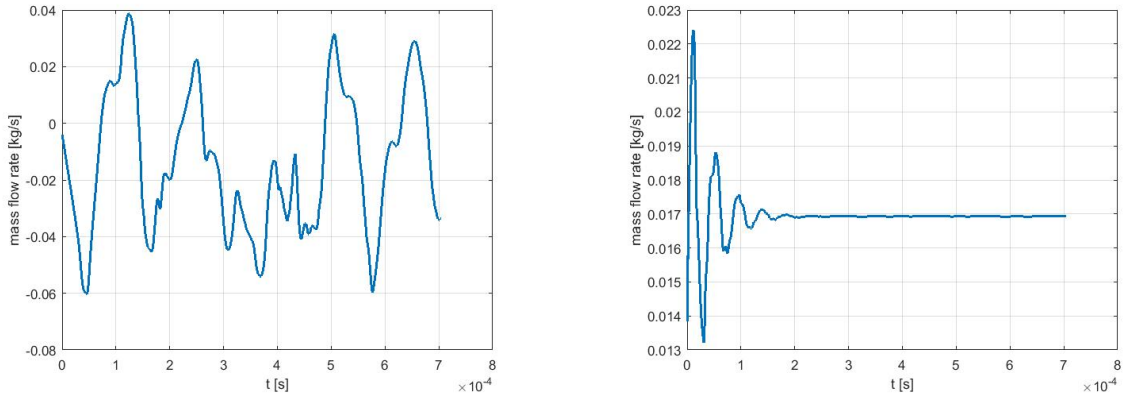

Figure 6.11: Outlet and inlet mass flow rates

For the outlet positive mass flow rates indicate a reversed flow, on the contrary, for the inlet positive mass flow rates indicate outflow.
Usually this kind of imbalance is a sign of a poor simulation setup, but in this case can be demonstrated that it depends on physical reasons instead of numerical and thus can be ac-

cepted.
To fulfil this purpose the outlet mass flow history will be compared for 3 different otlet distances from the nozzle exit outer border, and look if this affects the results in a physical way. The initial distance of 15 mm will be first quadruplicated and then this latter distance will be doubled and the three results will be compared.The next figure shows the results of this comparison.
Looking at this result it is possible to see that the simulations behave as expected. First of all

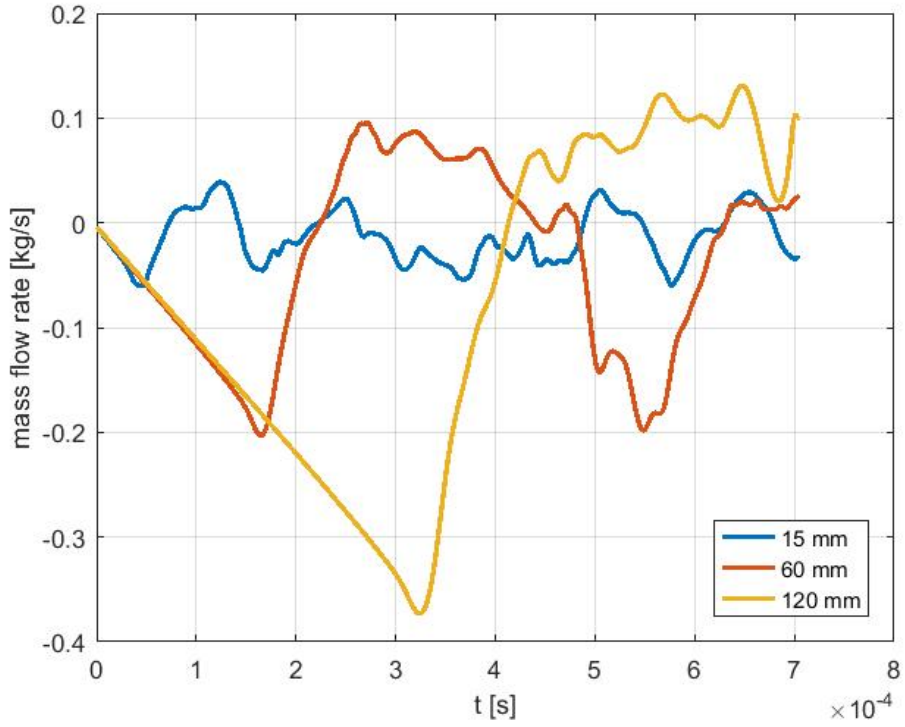

Figure 6.12: Outlet mass flow rate for different outlet distances

the three plots are shifted one to another due to the delay of the information signal traveling from the main flow to the outlet. The delay is almost proportional to the distance from the main flow, for example considering the first inflow peak position, in the first case it is positioned at $t_1 = 0.0456ms$, but in the second case at $t_2 = 0.165ms = 4t_1$, so the signal delay is proportional to the outlet distance. The same thing can be seen for the last outlet position: $t_3 = 0.361ms = 2t_2$. The traveling velocity of the information is almost the same for all the three cases, as seen from the velocity contours. Ater pointing out all of this is possible to state that the alternating inflow-outflow of the outlet is related to a physical motivation.
Another characteristic that is possible to notice is the increasing mass flow rate level for more far outlet position, that's due to the outlet increasing surface for higher radii.

The main physical reasons that contribute to the inflow or reversed flow condition of the outlet are: the cavity inflow or outflow phase and the oscillation of the normal shock in front of the cavity entrance.
By comparing the plots of the cavity entrance mass flow rate and the outlet mass flow rate for

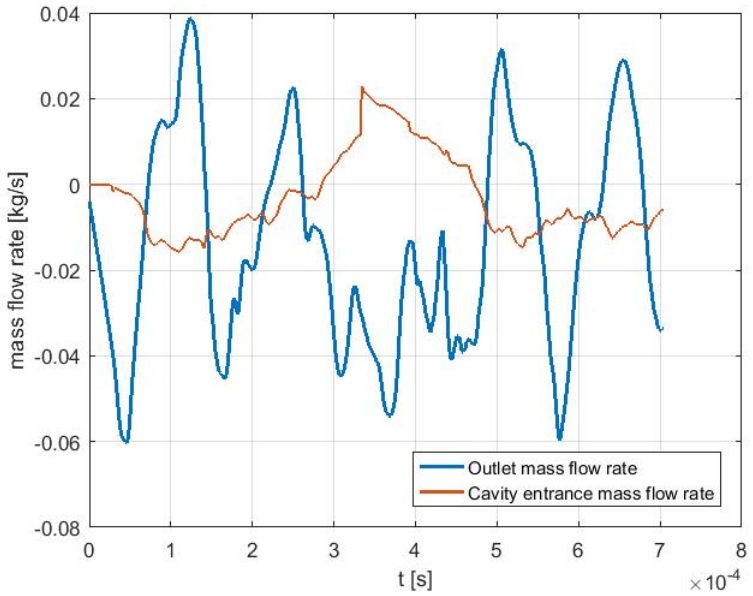

Figure 6.13: Outlet mass flow rate and cavity entrance mass flow rate for the standard case

the standard case is possible to notice that, as foreseen, the main inflow phase is beetween 0.3 ms and 0.5 ms and corresponds to the outflow phase of the cavity ,when the traveling shock pushs out the fluid from the cavity (for the cavity the outflow condition is achieved for positive mass flow rates).
Another reason can be the oscillatory motion of the normal shock wave in front of the cavity. Since the cavity-nozzle gap is designed in order to have the normal shock due to the jet cavity interaction in the unstable zone of the jet, there is an oscillation of this shock and of the jet structure.

6.0.4 Examination of iterative convergence

Generally CFD codes involve some iterative method to calculate the simulation solution. It is necessary to control how some important variables change with iterations, to assess if they converge or not.
First of all checking the residuals value is a must for every simulation. The residuals of the equations are the change in the equations results over an iteration,for fluent the default condition for convergence is that all the reiduals of the equations must be lower than 10^{-3}. Looking

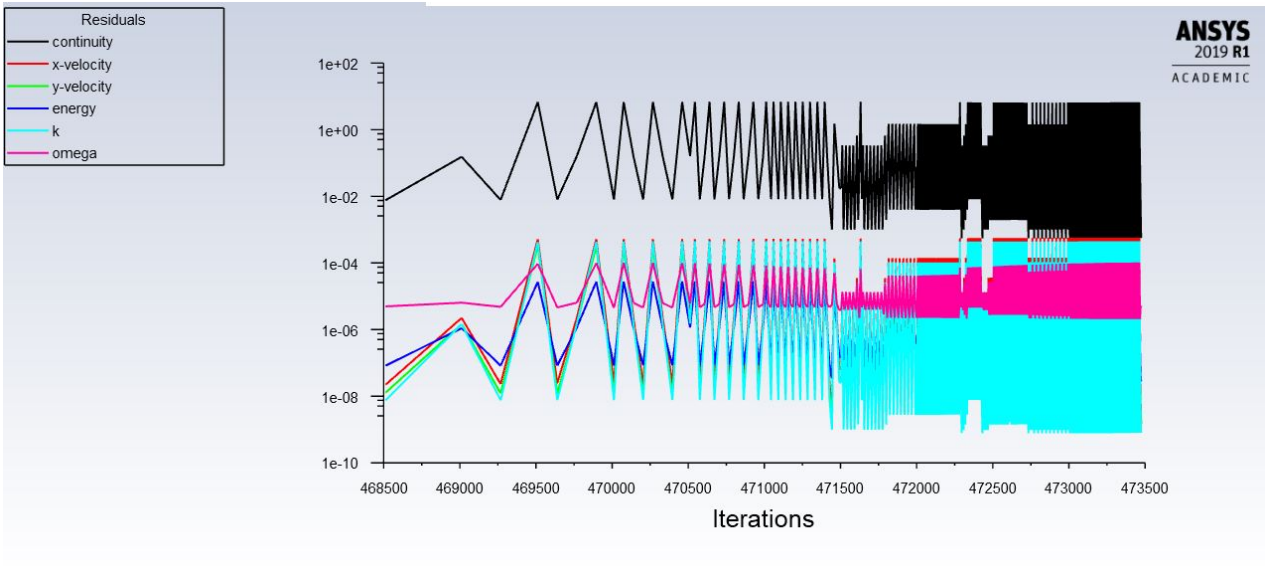

Figure 6.14: Residuals of the equation with respect to the iterations for the finest mesh

at the residuals plot and files it was found out that all the equations residuals are quite below the limit of 10^{-3} at least of 3 oreder of magnitude. The only noticeable exception is the continuity equation,but it still converge with an acceptable level of residuals value (10^{-3}) for all the timesteps.
At first the pressure based SIMPLE scheme was used for the simulation, but the continuity equation had some convergence issue for some of the timesteps. That's why a first order scheme for the time discretization was introduced and the Coupled scheme was used instead of the SIMPLE scheme. The coupled algorithm solves the momentum and pressure-based continuity equations together,the full implicit coupling has the advantage of a faster convergence than the semi-implicit pressure based segregated algorithm. Moreover for transient flows the coupled algorithm is useful to reduce the sensitivity on a poor mesh or large timesteps [10]. The improvement of performances and robustness of the simulation is payed with a more memory requirement to store the coupled coefficients.
The next step is to track the values of some engineering quantities or values of interest with respect to iteration and define iterative convergence when these quantities converge. In this case will be checked if these quantities change with respect to the number of iterations.
One of the most important integral quantities to monitor is the cavity entrance mass flow rate, that, as shown in some prior publications [25], has a great incidence on the performances, since bigger is the mass flow inside bettter will be the heating performances.

This quantity was found out to converge for every timestep. In the figure 6.15 is represented for simplicity only a monitor for a part of simulation, but the behavior was the same for the entire simulation. The quantity became indipendent with the iteration after a few iterations for every timestep, having a convergent behavior.

It is possible to state the same for the outlet mass flow rate, a plot similar to the one before is

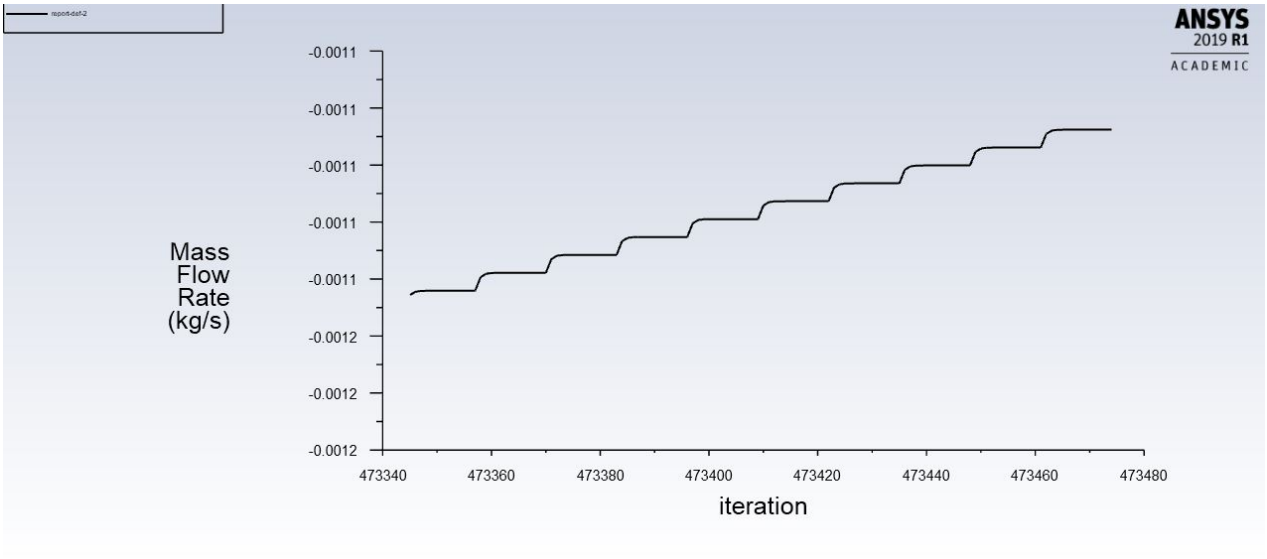

Figure 6.15: Cavity entrance mass flow with respect to the iterations for the finest mesh

shown in the next figure. This parameter has been monitored since there are some backflow conditions, so it is necessary to see if it is caused by a convergence issue.

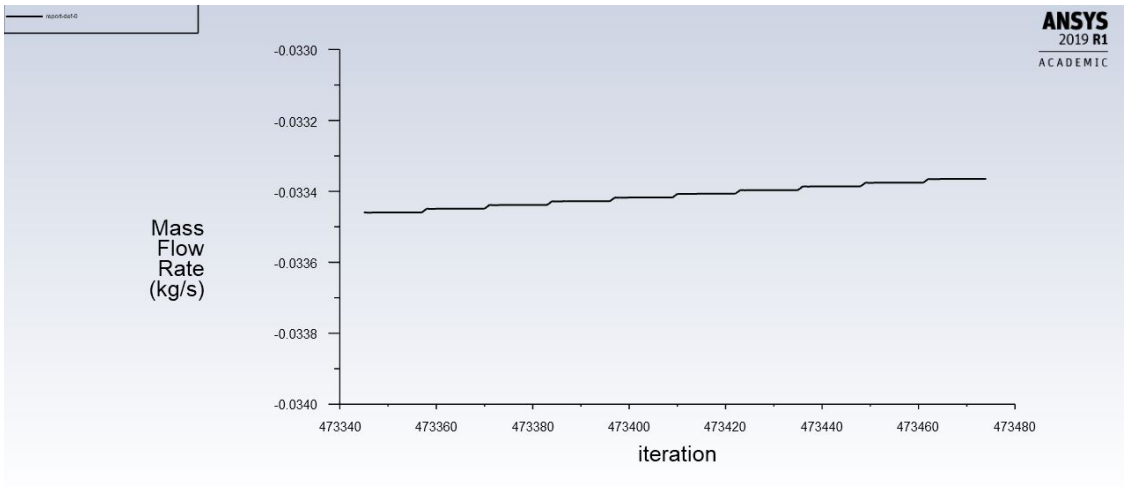

Figure 6.16: Cavity entrance mass flow with respect to the iterations for the finest mesh

Chapter 7

Validation of the results

The validation of a CFD code is defined as:

"The process of determining the degree to which a model is an accurate representation of the real world from the perspective of the intended uses of the model." [23]

The main strategy is to identify and quantify errors and uncertainties in the computational model. Since the validation must measure the accuracy in reproducing the real world the errors will be estimated comparing the results with experimental data. Since experimental data are always affected by accuracy issues is useful to take in account of experimental bias errors and random errors during the comparison, if available.
The number of validation test cases and the approaches. accuracy level required for each test case are highly application-dependent. It is not possible to define a single set of criteria for all applications.[23].
High accuracy in engineering calculation is not essential. As long as the trends predicted by the tools are consistent within the design envelope and an estimate of the error and uncertainty can be made, less-than perfect accuracy of the simulation is commonly acceptable.[23]
The validation process must be flexible, must allow various levels of accuracy and must be tolerant with incremental improvements.

7.1 Pressure frequency spectrum comparison

Due to the absence of pressure and temperature measurements within the resonator itself the microphone response has been selected as primary data for the validation. It is possible to assume that the microphone response is qualitatively linked to the phenomena taking place inside the resonator and in the area between resonator and nozzle. Other comparisons, for example about the cavity base pressure and temperature could not be possible even having experimental misurations inside the cavity, since for this simulation the walls were considered adiabatic, so the temperatures inside the cavity are overestimated.
For computational resources constraints was possible a simulation runtime of around 5 ms only,corresponding to $\sim 10\tau_{conv}$, so the results of the FFT analyis leads to a very coarse resolution in the frequency domain. That's why this results can only be considered as a pre-

liminary comparison, for a more accurate validation is necessary to have longer runtimes.

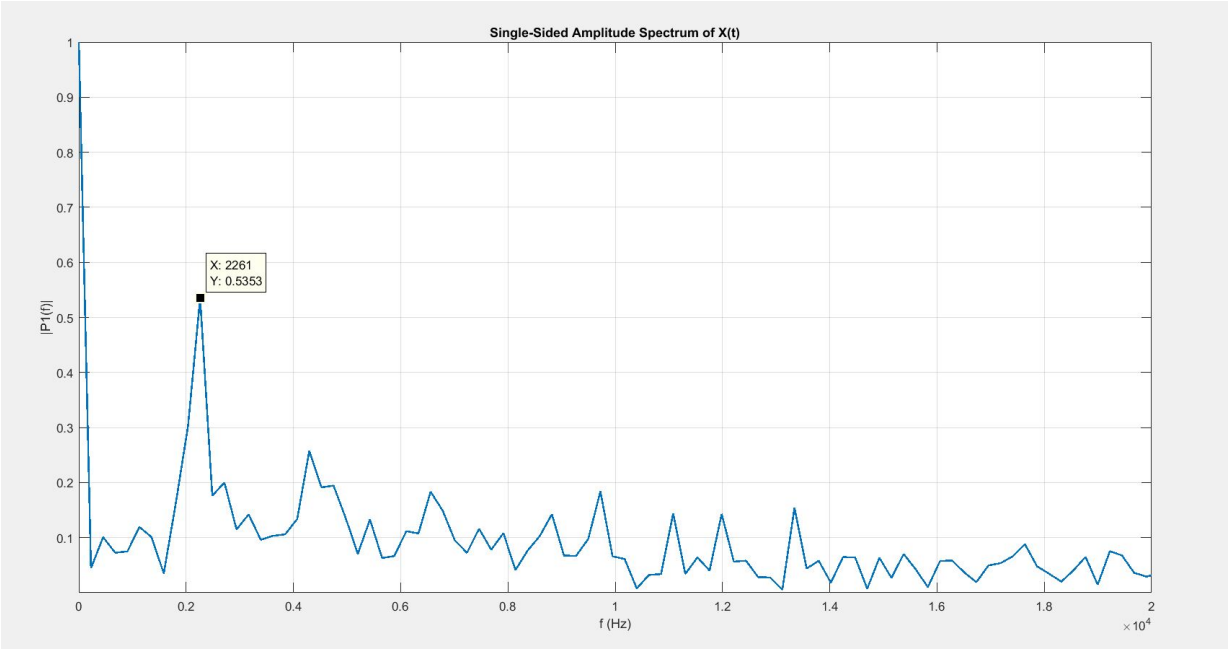

Figure 7.1: Frequency spectrum of cavity base pressure of the simulation (5 ms runtime)

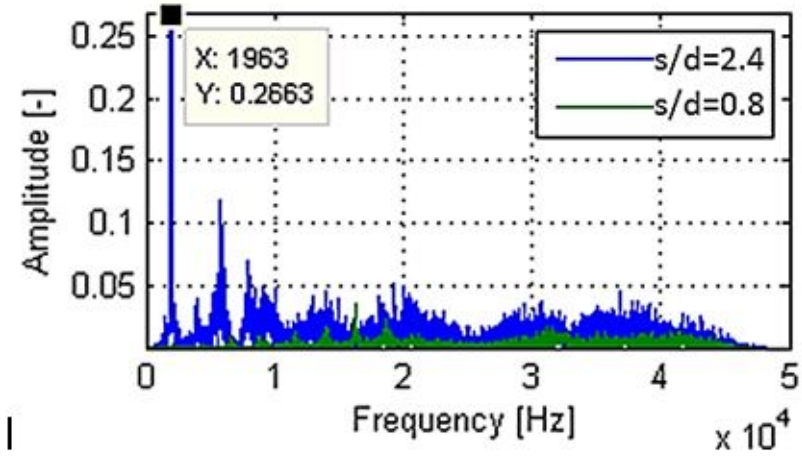

Figure 7.2: Non-calibrated microphone response spectrum for conical resonator at NPR 4 and s/d of 0.8 and 2.4 [11]

What is possible to state from this comparison is that, even for short runtimes, the peak frequency of the oscillations inside the tube is reproduced in an acceptable way, with an error of 15% compared to the experimental frequency. The higher frequency may be related to the fact that in this simulation the tube is considered adiabatic, so the mean temeperature is much higher than in the real tube and the speed of sound is proportional to that. As it is possible

to see by the cavity base temperature history the maximum temperatures are not comparable to the experimental ones, since are not balanced by heat transfer. A secondary peak in the frequency spectrum was detected, it is at a frequency of 4435 Hz, 1.96 times bigger than the main peak frequency, with an amplitude around 2 times lower. This relationship between the frequencies is qualitatively similar with the one found out in the experiments, as it is possible to see in figure 7.2, looking at the first and second peak.
Another factor that influence the frequency resopnse of the simulation can be seen in the following pressure history plot at the cavity base,where θ is the adimensionalized time, defined as :

$$\theta = \frac{t}{\tau_{conv}}$$

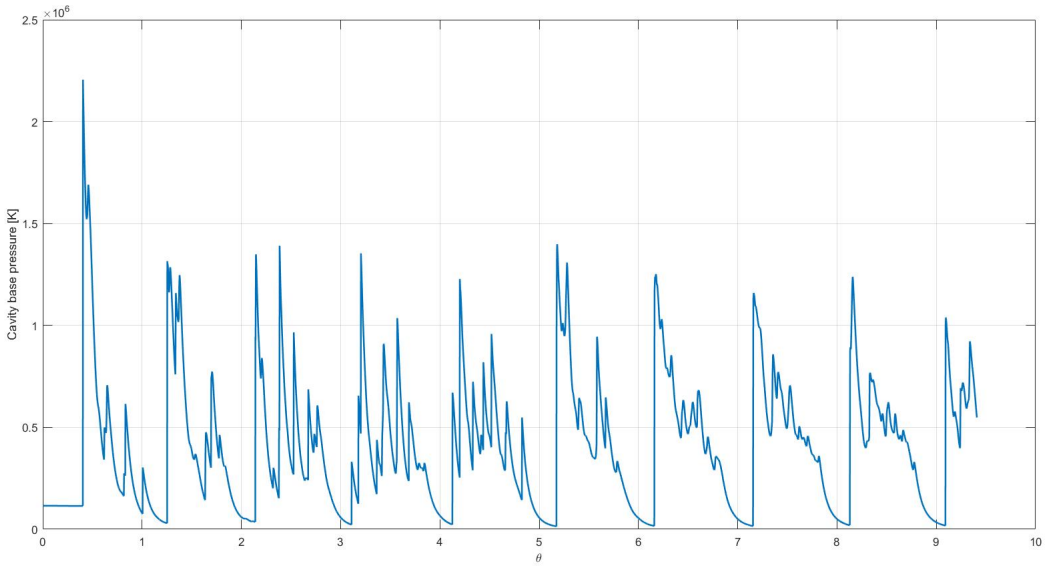

Figure 7.3: Pressure history of the cavity closed end

Looking at the plot it is possible to notice that the first 5 cycles are less regular than the others and show some internal oscillations. Moreover for the first cycle there is an high peak in the pressure value. It is possible to state that the periodic flow is still in a transition phase and thus the frequency computed is affected by this transition phase.
The frequency response was calculated for the last 4, 5, 7 cycles and then for all the cycles excluding the first, in order to establish the influence of the first transition cycles on the final results. The comparison is shown in the next figure.

Number of cycles considered	Last 4	Last 5	Last 7	Last 9	All
Peak frequency (Hz)	1920	1968	2027	2087	2261

Table 7.1

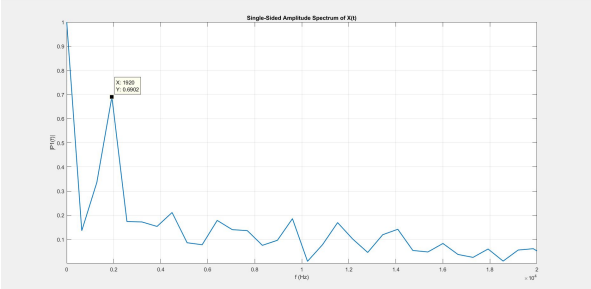

Figure 7.4: Last 4 cycles FFT

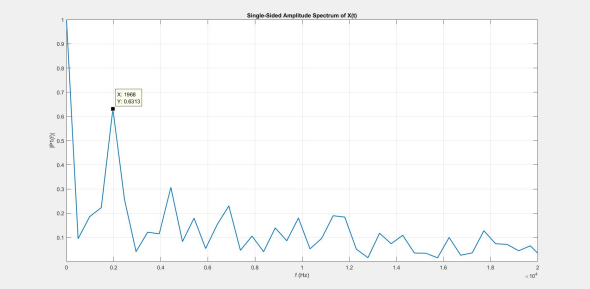

Figure 7.5: Last 5 cycles FFT

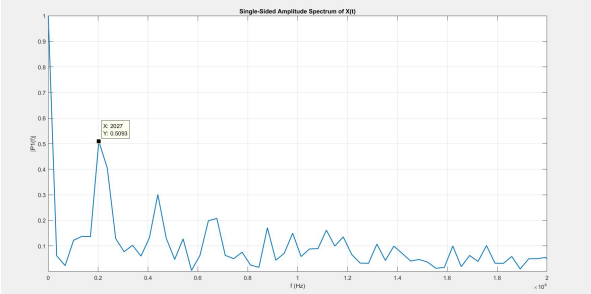

Figure 7.6: Last 7 cycles FFT

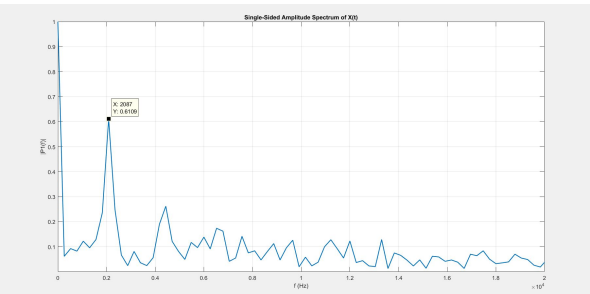

Figure 7.7: Last 9 cycles FFT

From the last results is possible to argue that there is an influence of the first cycles over the FFT analisys.The peak frequency including all the cycles is much higher then the one including only the last 4. The frequency rises if more of the first cycles are included in the evaluation window of the FFT analisys. That's an expected result, since in the first cycles there are many high amplitude oscillations, that may be related to a transition phase of the startup phase of the resonator. The highest frequency rise is seen when including the first cycle, that show a peak much higher then in the other cycles. For example by excluding just the first cycle the error related to the experimental result lowers to 6.3 %. After this analyis it is opinion of the author to conclude that the evaluation window should not include the first 5 cycles or at least the first, in this way only the stable operation regime is taken in account, and, in order to have an higher frequency domain resolution, should be a good choice to have a more wide evaluation window increasing the running time.

7.2 Influence of variable Cp

Constant pressure specific heat Cp is not constant in the actual world, but it is variable with temperature. By the opinion of the author was considered important to look deeper into the consequences of a variable Cp, since the shocks inside the tube cause high temperature gradients.
The Cp temperature dependency law chosen is a fourth order polynomial law empirically developed by NASA [26]. The espression looks like this:

$$\frac{C_p}{R} = a_1 + a_2 T + a_3 T^2 + a_4 T^3 + a_5 T^4 \tag{7.1}$$

The coefficients "a" depends on the gas species and temperature ranges, defined in the fluent input for piecewise-polynomial law. There are two possible temperature ranges, from 100 K to 1000 K and from 1000 K to 5000 K, the program switch to one or another depending on the temperature detected.

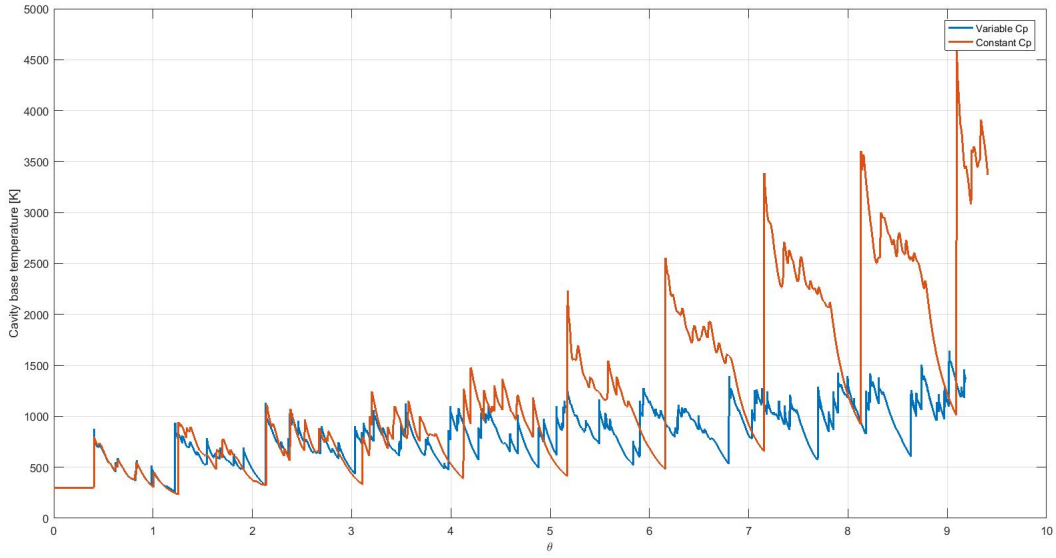

Figure 7.8: Cavity closed end temperature: variable Cp effect

One of the most noticeable effects of the variable Cp is the temperature decrease. Looking at the image is possible to see that the temperatures do not surpass 1650 K, and the peak temperatures for the constant Cp case are more than twice bigger. That behaviour is what would be espected from the fluid dynamic and thermodynamic theory and the resulting temperatures fits better the experimental rsults, even if are still higher because of the wall heat transfer neglection.
This reusult can be explained qualitatively by looking at the second law of thermodynamics:

$$\Delta s = C_p ln\left(\frac{T_2}{T_1}\right) - R ln\left(\frac{p_2}{p_1}\right) \tag{7.2}$$

Where Δs is the entropy jump, C_p the constant pressure specific heat, T the static temperature, R the gas constant,and p the static pressure. Or in a more specific way, looking into the irreversibe heat due to the shocks that Brocher derived [7], that is proportional to Cp :

$$Q_{irr} = mC_p\Delta T_5 \tag{7.3}$$

From these equations can be seen that for the same shock strength or for the same heat dissipation due to friction, so for the same entropy jump, the temperature obtained will be lower if the specific heat is higher. The specific heat represents how much energy is needed to rise the temperature of one mass unit by 1 K. That's why for the first cycle, where the temperature is lower and the Cp is closer to the constant standard value, the temperature of the two cases are almost coincident. For the last cycles, where the temperature is higher and the Cp difference is more important, the curves differs in a noticeable way.
Another factor that may be tha cause of this temperature lowering is the effect of mass exchange between cold and hot fluid. Th heat lost by the hot flow is [7]:

$$Q_m = m^*C_p(T_{tot2} - T_{tot}) \tag{7.4}$$

For the same mass exchanged the enthalpy carried by the hot $h = m^*C_pT_{tot2}$ is higher if the Cp rise, then the heat losses are higher.
Is then possible to say that the consequences over the temperatures are severe, than a variable Cp should be a good choice for this case of study, if a realistic temperature prediction is needed.
Looking at the frequency response is possible to see an higher frequency peak. The cycle duration is quite lower than the case of constant Cp, as is possible to notice even looking at the pressure and temperature plots.

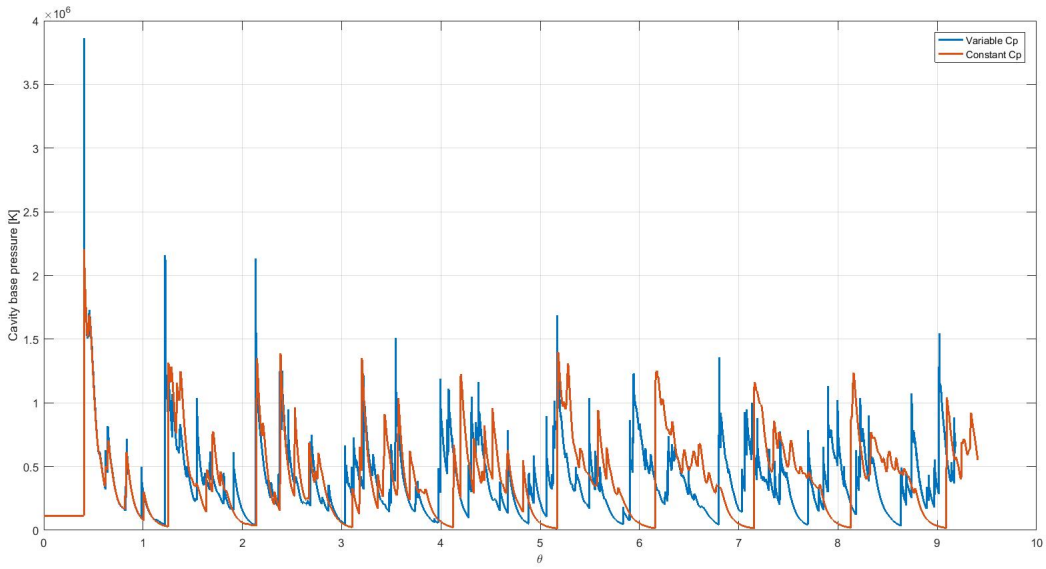

Figure 7.9: Cavity closed end pressure: variable Cp effect

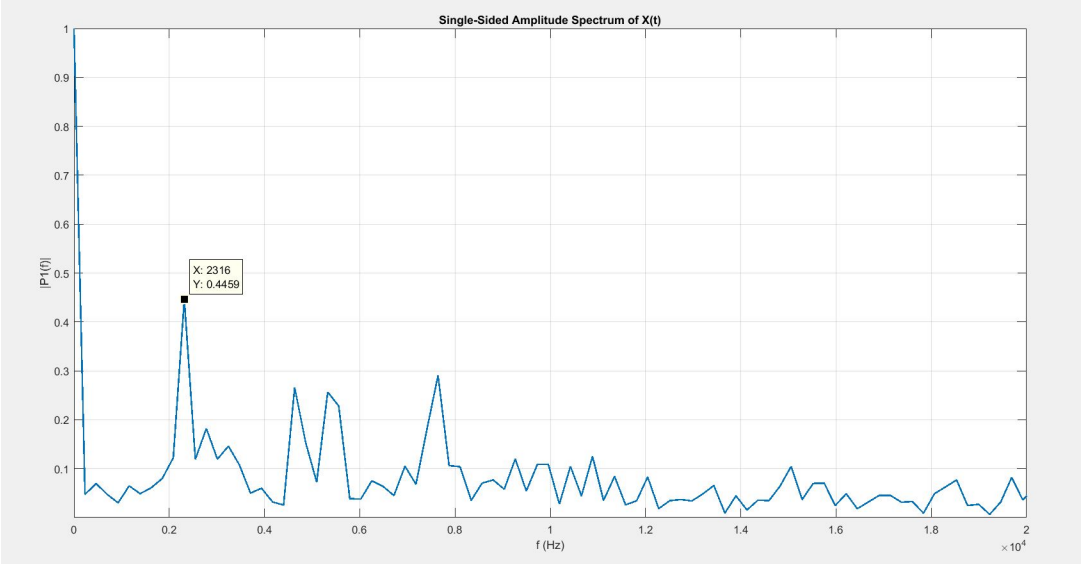

Figure 7.10: Frequency spectrum of cavity base pressure of the simulation for temperature dependent Cp

From the FFT analysis it is possible to notice that the error of the peak frequency increases. Moreover there are 3 more peaks that were not detected in the constant Cp analysis. The cycles appear less regular than the constant Cp case, the first 3 cycles has higher peaks, and genrally more in cycle secondary oscillations are detected and it is necessary to point out if are numerical spurious oscillations or are part of the transition phase. The main peak is detected at a frequency of 2316 Hz, the other three at 4633 Hz, 5327 Hz and 7644 Hz respectively. Taking in account the second peak it is at a fequency two times bigger than the first, with an amplitude 1.67 times lower.The relationship between this two frequencies is similar to the one found out in the first case with constant properties.

7.3 Influence of variable μ

Viscosity μ has a strong dependency on temperature and a low dependency on pressure. In this case there are big variations of temperaure because of the traveling shock waves irreversible heating effect.
Looking at this variable is quite important for the evaluation of heating effects related to irreversible heat dissipation caused by friction, that, as stated in the first chapter, is one of the main mechanisms that allows temperature rise inside the tube. Looking at the energy equation (equation 4.4) it is possible to see that temperature is connected with the dissipation function, that represents the work of friction forces due to velocity gradients that is irreveribly converted in internal energy. This function, is proportional to the viscosity μ,as shown in equation 4.5.
The viscosity model used in this section is the Sutherland viscosity law with three coefficients:

$$\mu = \mu_0 \frac{T^{3/2}}{T_0^{3/2}} \frac{T_0 + S}{T + S} \tag{7.5}$$

Where μ is the viscosity (Kg/ms), T is the static temperature (K), T_0 is the refrence temperature in K, S is an effective temperature in K.
This theory is based on ideal gas ipothesis and resulted from a kinetic theory by Sutherland (1893) using an idealized intermolecular-force potential [10]. For air and in general for gases the viscosity increases with temperature,as shown in the next figure.
For air the equation coefficients are as follows:

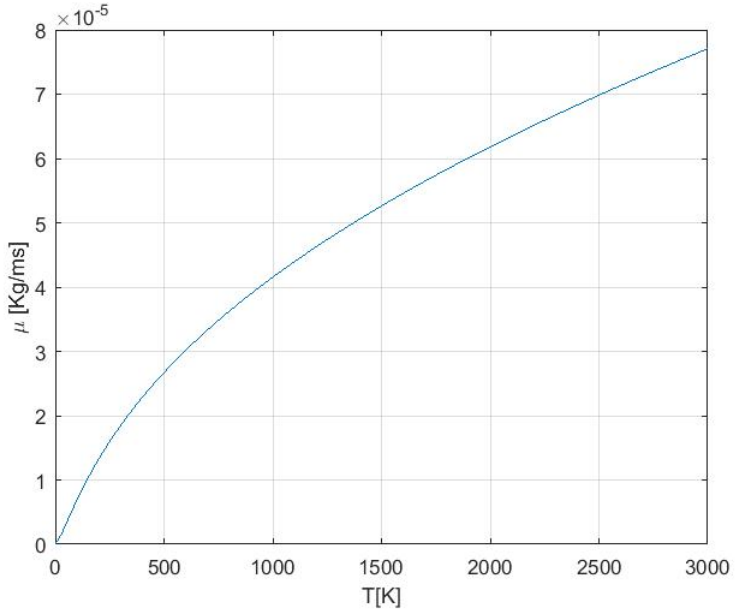

Figure 7.11: Sutherland law

- $T_0 = 273.11K$
- $S = 110.76K$

- $\mu_0 = 1.716 * 10^{-5}$

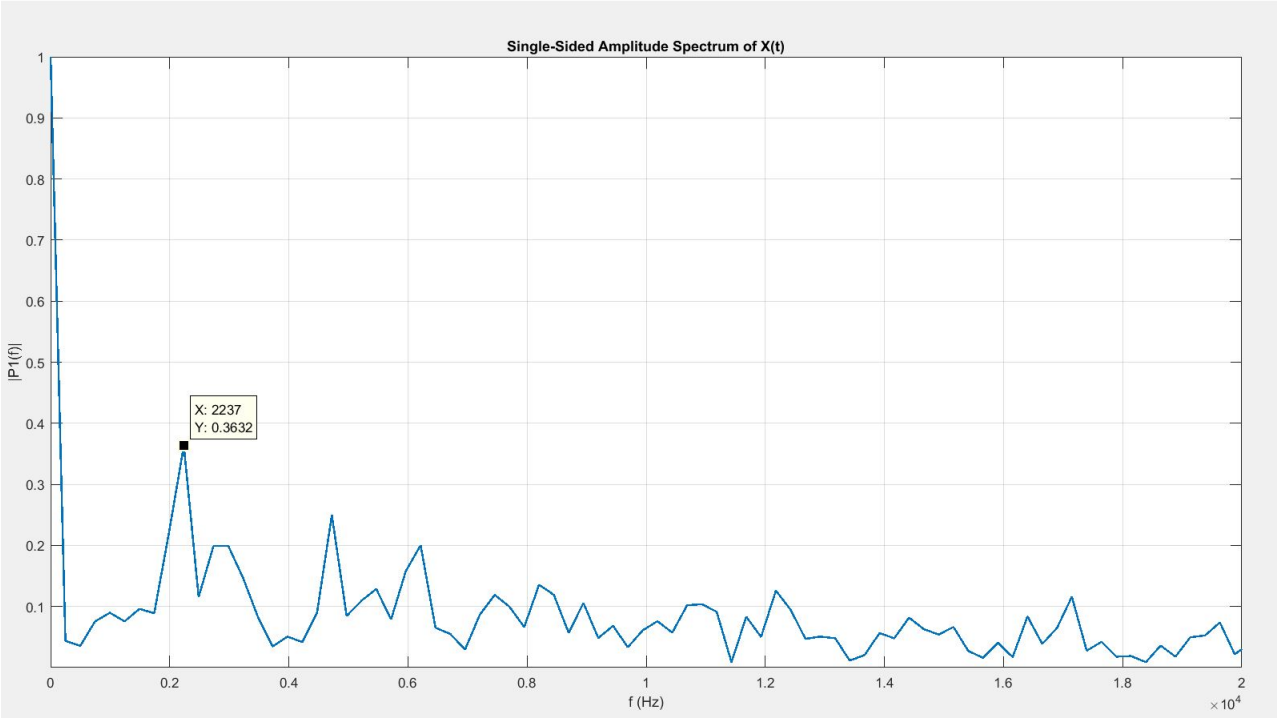

Figure 7.12: Frequency spectrum of cavity base pressure of the simulation for temperature dependent viscosity

The influence of the variable viscosity over the peak frequency is not quite noticeable, the error over the experimental results lowers to 13.7 %, with a difference of -1.3 % compared to the constant viscosity case. Looking at the secondary peaks we find out two main peaks, with a frequency of 4722 Hz and 6213 Hz respectively.The secondary peak frequency is 2.11 times bigger then the first peak frequency, showing a small difference with the constant viscosity case. The secondary peak and primary peak amplitude are one 1.5 times bigger then the other,showing a difference with the fist case.
Quite bigger differences were detected comparing the temperature histories, as shown in the plots the temperatures of th cavity closed end are more than twice higher for the case of constant viscosity. An increase of temperature was expected because of viscosity increase and its influence on the dissipation funcion in the energy equation, but the results show a different behaviour. Looking at the comparison of the cavity mass flow rate at the tube mouth is possible to notice that in the outflow phase there is a lower mass flow rate in the variable viscosity case, especially in the last cycles where the temperature difference is higher. The explaination can be found in the damping effect tha viscosity have on the velocity inside the tube.
The explaination of this temperature lowering can be found in the effect of viscosity on the mass exchange between hot indigenous flow and cold flow coming from the underexpanded jet seen in section 3.3, that was developed by Brocher and Maresca [7]. Looking at eqaution

3.12 is noted that the power lost because of mass exchange is proportional to:

$$\frac{P_m}{P_2} \propto \frac{m^*}{m}\frac{\rho_1}{\rho_2}$$

Using the equation for the mass exchanged 3.10 :

$$\frac{P_m}{P_2} \propto 0.103\left(\frac{L_p}{L}\right)^{4/5}\left(\frac{L}{D}\right)^{4/5}(Re)^{-1/5}\left(1-0.137\left(\frac{L_p}{L}\right)^{4/5}\left(\frac{L}{D}\right)^{4/5}(Re)^{-1/5}\right)$$

Considering that the Reynolds number is dependent with the viscosity $Re = \frac{uD\rho}{\mu}$ it is possible to plot the mass exchange with respect to the viscosity, in order to evaluate qualitatively the effect on heat losses. L is length of the tube and L_p the penetration depth, that is calculated using the simplified method of Liang [9]:$L_p = L - L_{cs} = L(1 - 0.5(k+1)^2)$. The diameter D used is the one of the tube entrance.

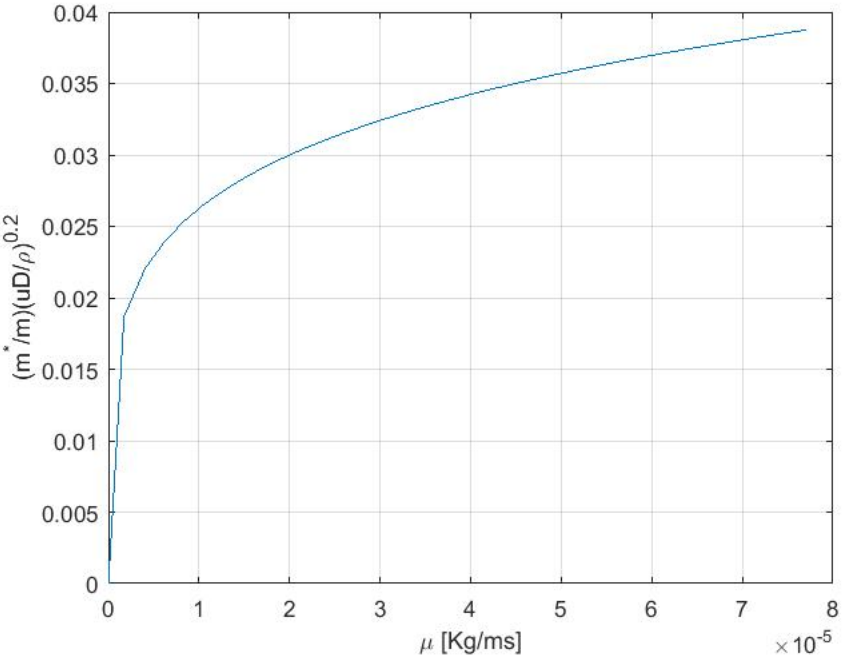

Figure 7.13: viscosity effect on mass exchanged between extranous and indigenous flow

Looking at this picture it is possible to noctice that the mass exchanged rise with lowering the Reynolds number, thus by increasing the viscosity. In this way it is possible to say that the viscosity effect make increase the heat lost by mass exchange, that balance the increase of the friction effect, thus having lower temperatures in the resonator.
The effect of the viscosity on the heat caused by friction dissipation is lower than the effect on mass exchange losses. The effect on friction as seen in section 3.2.2 is proportional to friction coeffcient, that is:

$$C_f = 0.316Re^{-0.25}$$

So it is proportional to $\mu^{0.25}$. So as seen from the results and from this qualitative analysis, the influence of the viscosity is important especially for the temperature response, becuase of the combined effect of friction heat dissipation and of the effect of mass exchange through the boundary layer height between cold and hot gas in the tube.

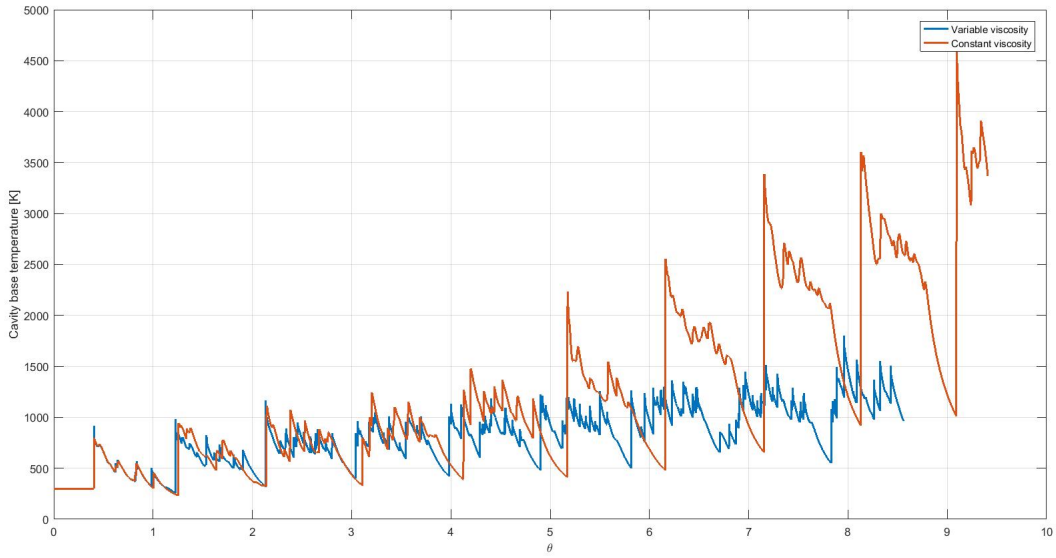

Figure 7.14: Cavity closed end temperature: variable viscosity effect

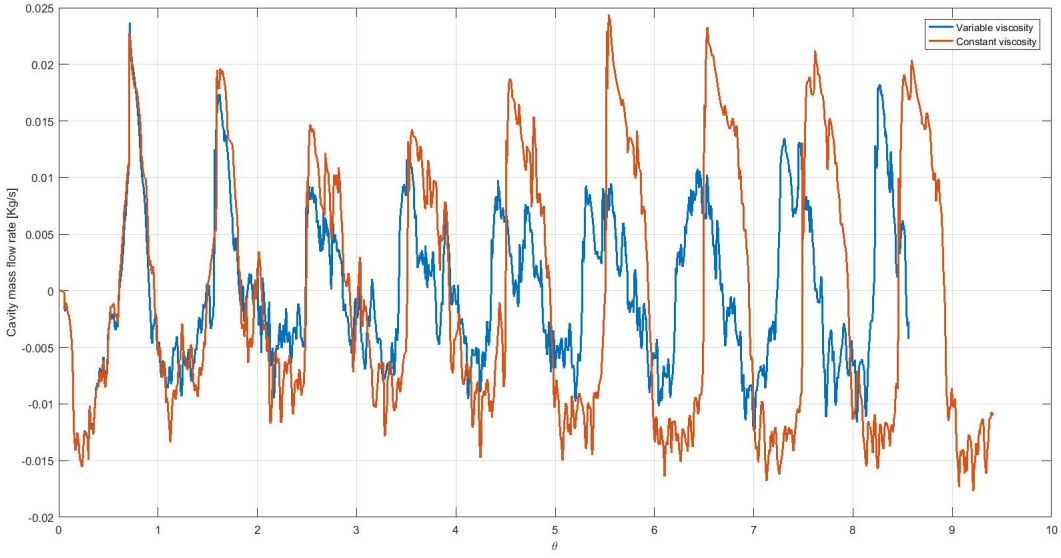

Figure 7.15: Cavity mass flow rate: variable viscosity effect

7.4 Schlieren image comparison

During the experiment some images of the underexpanded jet were taken by using the Schlieren technique. Schlieren imaging systems have been used since the early 1800's to visualize fluctuations in optical density.The physical basis for schlieren imaging emerges from Snell's Law, which states that light slows upon interaction with matter. If media is homogeneous, such as in a vacuum, or space, light travels uniformly, at a constant velocity. When encountering inhomogenous media, such as fluids in motion, light rays refract and deflect from their continuous path, resulting in schliere.[27]
The refractive index n = c0/c of a medium describes the change in phase speed where c is the speed of light in the medium and c0 is the speed of light in a vacuum. For gases the refractive index is linearly dependent on the gas density according to the Gladstone-Dale relation:

$$n = K\rho + 1$$

where K is the Gladstone-Dale constant and ρ is the gas density.
If a light ray passes in an orthogonal way trough a change in refractive index, so a change in density, it will continue traveling in the same direction but with different phase velocity. If the ray intersect the density change obliquely it will bend towards the region of bigger refractive index. For a ray traveling in the z direction its curvature intersecting the density change is:

$$\frac{\partial^2 x}{\partial z^2} = \frac{1}{n}\frac{\partial n}{\partial x}$$

Integrating the angular ray deflection is:

$$\epsilon = \frac{1}{n}\int \frac{\partial n}{\partial x}\partial z$$

What is possible to see with a Schlieren image is the ray curvature, so it is proportional to the first derivative of the refractive index, thus to the density gradient.
For this latter analisys was decided to do the comparison of the shlieren image with a greyscale contour plot of the density gradient, obtained by using the "Paraview" post processing software. The results of this schlieren like plots are represented in the next figures, where is possible to see the typical structures of the underexpanded jet and the shocks in front of the cavity. The plot shown here are in a logaritmic scale such that the flow structures are more clearly visible.

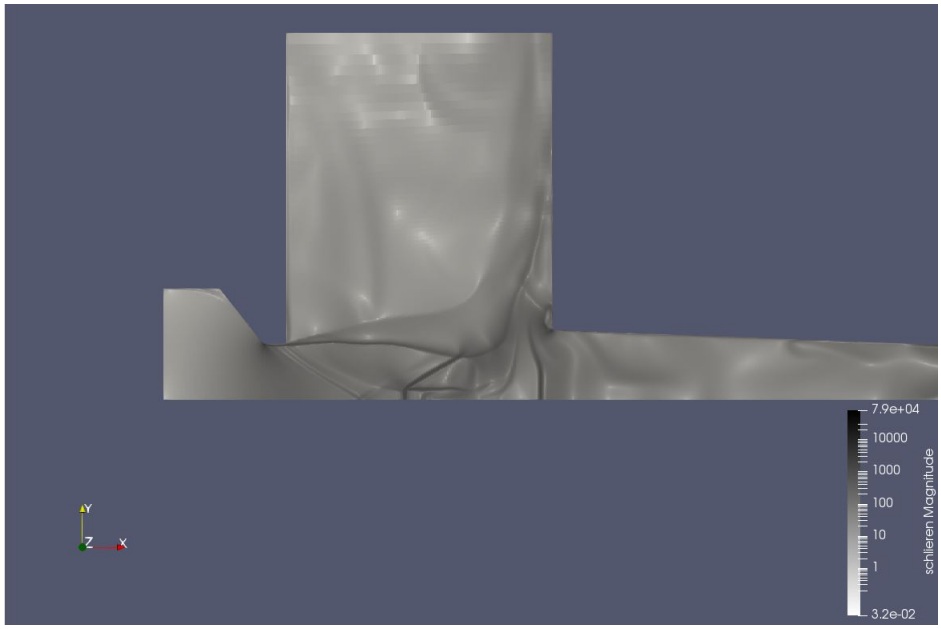

Figure 7.16: Numerical schlieren-like image during outflow: t=0.33 ms

Figure 7.17: Numerical schlieren-like image during inflow: t=0.11 ms

Looking at figure 7.18 ,that compares the schlieren image (below) with the numerical reproduction of it (on the top), is possible to see that the jet main structure is reproduced acceptably. The jet boundaries are well reproduced, moreover is possible to see that the position of the mach disk is almost the same. At the beginning of the jet is possible to see the expansion fans very clearly in the numerical image, and a similarstructure is visible also in the experimental image.
This comparison can be only considered as qualitative, since the schlieren image has not

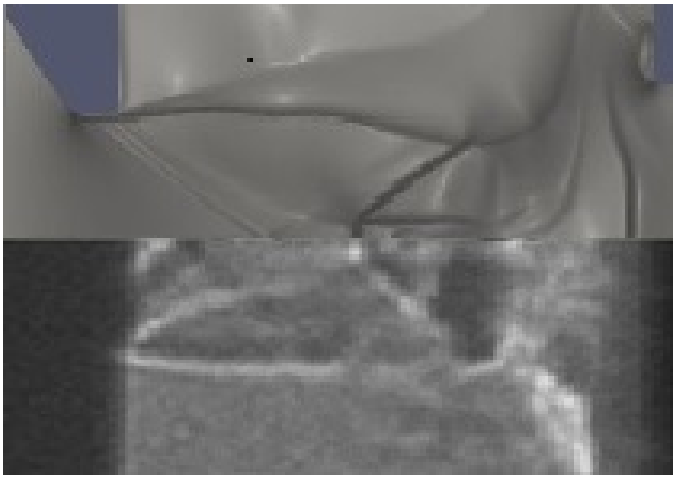

Figure 7.18: Comparison of numerical and experimental schlieren image during outflow

enough temporal and spatial resolution, so it cannot be used to establish definitive conclusions on the validity of the CFD calculations, especially in a highly unsteady phenomenon like this. Furthermore the image is not at high resolution, so it is difficult to see the details of the shock structures.
This last analisys can only be considered as a qualitative demonstration of the code capability to reproduce the real phenomenon characteristics, especially for what concerns the underexpanded jet.

Chapter 8

Conclusions

That study tried to verify and validate a Fluent CFD code for the simulation of the transient heat up phase of a resonance igniter for rocket engines applications. The study was motivated by the high reliability of this ignition technology, that is quite suitable for satellite propulsion systems with long mission duration and high number of ignitions. This technology is suitable even for green non hypergolic propellants, that are an important object of research after hydrazine had been declared a material of very high concern.
The importance of CFD for the analysis of this kind of technology has been pointed out in this thesis. The complexity of the phenomenon requires computational fluid dynamics to have results that can be comparable to the real world. All the theoretical approaches have too many restrictive hypotesis, for example on the fluid properties and on the resonator geometry, and can be used only for qualitative predictions, but not for real applications.
From the CFD analysis was found out that the density based solver, even if is the most precise for compressible flows, is not stable enough. Better results were obtained with the pressure based solver using a coupled algorithm, this one is less sensible on poor mesh and timestep for transient simulations compared to the segregated algorithm and to the density based solver, that showed stability issues. The verification phase showed an acceptable behaviour of the code, that do not show iterative convergence issues. The code shows reversed flow on the outlet, but it was demonstrated to be physical and not a numerical artifact.
The validation of the code was carried out comparing the simulation with the results of an experimental campaign conducted at Techincal University of Munich by LTF. In this phase was investigated how the code reproduced the real behaviour of the resonator. First of all was verified that the main flow features were reproduced, for example was verified that the periodic inflow and outflow phases were established by looking at the cavty mass flow rate. Moreover by comparing the schlieren images of the undrexpanded jet with the numerical schlieren was qualitatively verified that the main jet structure characteristics were reproduced.
Looking more in detail in the validation, a comparison of the closed end pressure frequency spectrum with the frequency response of the microphone of the experiments was done. By this analysis was detected a good agreement with the experimental results, especially excluding the first trasitory cycle, that shows an anomalous peak, the error lowers from 15% to 6%. This results however are still preliminary, since a wider temporal evaluation window should be considered to have a better resolution on frequency domain. Another limit of this comparison is that the microphone position is outside the resonator, so the correlation with the

pressure frequency spectrum of the cavity base is only qualitative.
Finally a calibration analysis was carried out by looking deeper into the effect of the fluid properties, by using a temperature dependent viscosity and specific heat Cp. The variation of Cp and viscosity do not have important effects on the frequency response, that is similar to the constant fluid properties case, even looking at the main and secondary peak positions and amplitudes .Bigger effects were detected on the cavity base temperatures. The temperatures detected in this case are much more realistic, shows a maximum of around 1600 K, much lower than the initial case that has a maximum temperature of around 4000 K. In the experiments the maximum temperature detected was around 1000 K, still lower than the temperatures obtained in this case, because of the neglection of heat transfer in the simulation. The main reason that was considered for this temperature lowering is the effect of the Cp on the temperature rise because of the heat disspiation of the shock wave and on the enthalpy transported with the mass exchange between cold gas and hot gas in the tube. For the viscosity the main hypotesis, based on theoeretical results, is the effect on the mass exchanged through the boundary layer beetween cold and hot flow. However if the simulation aim is to have a realistic temperature prediction should be necessary to include the variation of μ and C_p.

8.1 Possible future developements

This study was only a preliminary approach to the problem. Due to the computational limits a small temporal evaluation window was used, that affected the results. Moreover there are still big discretization errors, that do not affect the prediction of ignition, but could affect the comparison with experiments. For future simulations is suggested to use a finer mesh and have longer simulation runtimes.Having longer runtimes would allow even to look deeper into the cyclic behaviour, establishing how long is the duration of the transient heating phase, an important parameter for real applications.
Another limit that was found in this validation was the link between the cavity base pressure history and the microphone response, since the microphone is located outside the cavity. For future similar validation is suggested to find a transfer function between this two pressure histories.
The analysis used adiabatic walls, not including wall heat transfer. For future works on that field should be introduced wall heat transfer, that is a limiting parameter for the resonance heating as shown by several studies [2]. The reults in this case would be more realistic and suitable for a temperature comparison with experiments. In this work should be interesting a comparison with the results obtained in this thesis, to quantify the influence of material insulation of the tube.
In this validation work was not investigated the role of turbolence, a possible continuation of this work should be the influence of the turbolence model settings on final results, choosing the most suitable for reproducing experimental results.

Bibliography

[1] P. Lungu, C. Bauer, and O. J. Haidn, "Operational behaviour investigation of hartmann-sprenger tube based resonance ignition systems for oxygen/methane in-orbit propulsion applications."

[2] B. R. Phillips and A. J. Pavli, "Resonance tube ignition of hydrogen–oxygen mixtures," National Aeronautics and Space Administration, Cleveland, Ohio (USA). Lewis ..., Tech. Rep., 1971.

[3] V. Bogdanov, "Contemporary achievements in the field of acoustic ignition systems," *Procedia engineering*, vol. 129, pp. 702–707, 2015.

[4] C. Bauer and O. J. Haidn, "Design and test of a resonance ignition system for green in-orbit propulsion systems," in *52nd AIAA/SAE/ASEE Joint Propulsion Conference*, 2016, p. 4688.

[5] C. G. Przirembel, "Aerothermodynamic aspects of an i. 5 axisymmetric resonance tube," *AIAA Journal*, vol. 18, no. 9, pp. 1141–1143, 1980.

[6] P. A. Thompson, "Jet-driven resonance tube," *Aiaa Journal*, vol. 2, no. 7, pp. 1230–1233, 1964.

[7] E. Brocher and C. Maresca, "Etude des phenomenes thermiques dans un tube de hartmann-sprenger," *International Journal of Heat and Mass Transfer*, vol. 16, no. 3, pp. 529–538, 1973.

[8] A. H. Shapiro, "On the maximum attainable temperature in resonance tubes," *Journal of the Aerospace Sciences*, vol. 27, no. 1, pp. 66–67, 1960.

[9] G. Liang, G. Zhang, and X. Cheng, "Preliminary investigation on gas dynamic resonance ignition for liquid propellant rocket engine," *JOURNAL OF PROPULSION TECHNOLOGY-BEIJING-*, vol. 20, pp. 13–16, 1999.

[10] A. Fluent, "Ansys fluent theory guide 15.0," *ANSYS, Canonsburg, PA*, 2013.

[11] C. Bauer and O. Haidn, "Numerical and experimental investigations on resonance ignition," in *Space Propulsion Conference*, 2014.

[12] C. Robinson and D. Smith, "The auto-ignition temperature of methane," *Journal of hazardous materials*, vol. 8, no. 3, pp. 199–203, 1984.

[13] X. Annex, "Proposal for identification of a substance as a category 1a or 1b cmr, pbt, vpvb or a substance of an equivalent level of concern."

[14] J. Hartmann, "On a new method for the generation of sound-waves," *Physical Review*, vol. 20, no. 6, p. 719, 1922.

[15] H. Sprenger, "Über thermische effekte in resonanzrohren," *Mitteilungen aus dem Institut für Aerodynamik an der ETH Zürich*, vol. 21, p. 18, 1954.

[16] V. Sarohia and L. H. Back, "Experimental investigation of flow and heating in a resonance tube," *Journal of Fluid Mechanics*, vol. 94, no. 4, pp. 649–672, 1979.

[17] A. Hamed, K. Das, and D. Basu, "Numerical simulation and parametric study of hartmann-sprenger tube based powered device," in *41st aerospace sciences meeting and exhibit*, 2003, p. 550.

[18] C. BAUER, M. HAUSER, and O. J. HAIDN, "Investigation of stabilization effects in hartmann-sprenger tubes," *TRANSACTIONS OF THE JAPAN SOCIETY FOR AERONAUTICAL AND SPACE SCIENCES, AEROSPACE TECHNOLOGY JAPAN*, vol. 14, no. ists30, pp. Pa_95–Pa_100, 2016.

[19] R. MCALEVY III and A. Pavlak, "Tapered resonance tubes-some experiments," *Aiaa Journal*, vol. 8, no. 3, pp. 571–572, 1970.

[20] E. Michael, S. Narayanan *et al.*, "Numerical simulation of jet flow impinging on a shielded hartmann whistle," *International Journal of Aeronautical and Space Sciences*, vol. 16, no. 2, pp. 123–136, 2015.

[21] H. Kuttruff, *Acoustics: an introduction*. CRC Press, 2006.

[22] C. Bauer, P. Lungu, and O. J. Haidn, "Numerical investigation of a resonance ignition system," in *8th European Conference for Aeronautics and Space Sciences*, 2019.

[23] W. L. Oberkampf and T. G. Trucano, "Verification and validation in computational fluid dynamics," *Progress in aerospace sciences*, vol. 38, no. 3, pp. 209–272, 2002.

[24] I. B. Celik, U. Ghia, P. J. Roache, and C. J. Freitas, "Procedure for estimation and reporting of uncertainty due to discretization in cfd applications," *Journal of fluids Engineering-Transactions of the ASME*, vol. 130, no. 7, 2008.

[25] J. Lee, D. Lim, S. Seo, and S. H. Kang, "Numerical analysis of the thermal characteristics of a gas-dynamic ignition system," *Journal of Mechanical Science and Technology*, vol. 32, no. 5, pp. 2385–2390, 2018.

[26] B. J. McBride, S. Gordon, and M. A. Reno, "Coefficients for calculating thermodynamic and transport properties of individual species," 1993.

[27] A. Mazumdar, "Principles and techniques of schlieren imaging systems," 2013.